Photon echo studies of rare-earth-activated materials for optical memory and signal processing devices
by Randy Wayne Equall

A thesis submitted in partial fulfillment of the requirements for the degree of Doctor of Philosophy in Physics
Montana State University

Abstract:
The optical spectroscopy and dynamics of three materials; Eu^3+:Y2SiO5, Pr^3+:Y2SiO5, and Tm^3+:Y2SiO5 that are of interest for application in persistent spectral holeburning optical memory and signal processing devices were investigated using linear and nonlinear spectroscopic techniques. Two-pulse photon echoes have been used to measure the homogeneous linewidths. The effects of instantaneous spectral diffusion were systematically studied to allow accurate determination of the optical resonance widths, and external magnetic fields were applied to characterize the effects of fluctuating nuclear spins of the host lattice on dephasing of the dopant ion.

The 7F0 → 5D0 transition of 0.1% Eu^3+ in the two crystallographic sites of Y2SiO5 was studied using photon echoes. Using this material, we succeeded in measuring the narrowest optical resonance in a solid by shielding the crystal from stray electromagnetic fields and using sufficiently low laser power to minimize contributions from instantaneous diffusion. The homogeneous linewidths measured in a magnetic field of 100 G are 122 Hz (site 1) and 167 Hz (site 2). These widths are dominated by population decay, but up to 20 Hz is attributed to 89Y spin fluctuations which have been reduced by the applied magnetic field.

Similar studies were performed to determine the contributions to the homogeneous linewidth of the 3H4(1) → 1D2(1) transition for both sites of 0.02% Pr^3+ in Y2SiO5. Linewidths of 2.1 kHz (site 1) and 0.85 kHz (site 2) were obtained with an applied magnetic field of 77 G. A significant contribution of 89Y nuclear spin fluctuations to the zero-field homogeneous linewidth was found. Optically detected nuclear magnetic resonance measurements determined the hyperfine structure of the 3H4 ground state for each site, and photon echo nuclear double resonance was used to determine the hyperfine levels of the lowest component of the 1D2 manifold.

Absorption, fluorescence, fluorescence excitation and Zeeman experiments were performed to characterize the crystal field levels of 0.1% Tm^3+ in Y2SiO5. Small splittings of only 13 cm^-1 (site 1) and 1.6 cm^-1 (site 2) were found for the lowest components of the 3H6 ground state multiplet. The homogeneous linewidth of the 3H6 → 3H4 transition was also measured yielding widths of 57 kHz (site 1) and 241 kHz (site 2) in zero magnetic field. These unexpectedly large widths were attributed to the accidental magnetic sensitivity of Tm^3+ in this host due to the presence of enhanced nuclear magnetic moments resulting from the energy level structure.

PHOTON ECHO STUDIES OF RARE-EARTH-ACTIVATED MATERIALS FOR OPTICAL MEMORY AND SIGNAL PROCESSING DEVICES

by

Randy Wayne Equall

A thesis submitted in partial fulfillment
of the requirements for the degree

of

Doctor of Philosophy

in

Physics

MONTANA STATE UNIVERSITY
Bozeman, Montana

May 1995

APPROVAL

of a thesis submitted by

Randy Wayne Equall

This thesis has been read by each member of the thesis committee and has been found to be satisfactory regarding content, English usage, format, citations, bibliographic style, and consistency, and is ready for submission to the College of Graduate Studies.

5/18/95 — Rufus L Cone

Date — Chairman, Graduate Committee

Approved for the Major Department

5-18-95

Date — Head, Major Department

Approved for the College of Graduate Studies

6/31/95

Date — Graduate Dean

STATEMENT OF PERMISSION TO USE

In presenting this thesis in partial fulfillment of the requirements for a doctoral degree at Montana State University, I agree that the Library shall make it available to borrowers under rules of the Library. I further agree that copying of this thesis is allowable only for scholarly purposes, consistent with “fair use” as prescribed in the U. S. Copyright Law. Requests for extensive copying or reproduction of this thesis should be referred to University Microfilms International, 300 North Zeeb Road, Ann Arbor, Michigan 48106, to whom I have granted “the exclusive right to reproduce and distribute my dissertation for sale in and from microform or electronic format, along with the right to reproduce and distribute my abstract in any format in whole or in part.”

Signature Randy W. Egsell

Date 5/18/95

ACKNOWLEDGMENTS

It is my pleasure to acknowledge the people who have helped make the work presented in this thesis possible. First and foremost, I would like to thank my advisor Rufus Cone for the opportunity to work in his lab and for his expert scientific and experimental guidance. His endless patience and encouragement have made my tenure here a truly enjoyable experience. I would also like to thank Roger Macfarlane who has been involved in all aspects of this research. Our many conversations have provided both insight and inspiration. Thanks also to Ralph Hutcheson at Scientific Materials for providing some of the crystals used in these studies.

I would also like to acknowledge my fellow students in the lab: Yongchen Sun, Guangming Wang, Meg Hall, and Greg White for their help in performing experiments and for our many useful discussions.

I also want to thank Norman Williams and Erik Andersen for their expert technical advice and aid in the construction and maintenance of the equipment that made this research possible.

Finally, I owe my wife and parents more than words can really express. Throughout my academic career they have been a constant source of support and encouragement. I especially wish to thank my wife Nancy for her patience during the many late nights when the helium just never seemed to run out.

TABLE OF CONTENTS

TABLE OF CONTENTS—Continued

LIST OF TABLES

LIST OF FIGURES

LIST OF FIGURES—Continued

LIST OF FIGURES—Continued

LIST OF FIGURES—Continued

ABSTRACT

The optical spectroscopy and dynamics of three materials; Eu^{3+}:Y_2SiO_5, Pr^{3+}:Y_2SiO_5, and Tm^{3+}:Y_2SiO_5 that are of interest for application in persistent spectral holeburning optical memory and signal processing devices were investigated using linear and nonlinear spectroscopic techniques. Two-pulse photon echoes have been used to measure the homogeneous linewidths. The effects of instantaneous spectral diffusion were systematically studied to allow accurate determination of the optical resonance widths, and external magnetic fields were applied to characterize the effects of fluctuating nuclear spins of the host lattice on dephasing of the dopant ion.

The $^7F_0 \rightarrow {}^5D_0$ transition of 0.1% Eu^{3+} in the two crystallographic sites of Y_2SiO_5 was studied using photon echoes. Using this material, we succeeded in measuring the narrowest optical resonance in a solid by shielding the crystal from stray electromagnetic fields and using sufficiently low laser power to minimize contributions from instantaneous diffusion. The homogeneous linewidths measured in a magnetic field of 100 G are 122 Hz (site 1) and 167 Hz (site 2). These widths are dominated by population decay, but up to 20 Hz is attributed to ^{89}Y spin fluctuations which have been reduced by the applied magnetic field.

Similar studies were performed to determine the contributions to the homogeneous linewidth of the $^3H_4(1) \rightarrow {}^1D_2(1)$ transition for both sites of 0.02% Pr^{3+} in Y_2SiO_5. Linewidths of 2.1 kHz (site 1) and 0.85 kHz (site 2) were obtained with an applied magnetic field of 77 G. A significant contribution of ^{89}Y nuclear spin fluctuations to the zero-field homogeneous linewidth was found. Optically detected nuclear magnetic resonance measurements determined the hyperfine structure of the $^3H_4$ ground state for each site, and photon echo nuclear double resonance was used to determine the hyperfine levels of the lowest component of the $^1D_2$ manifold.

Absorption, fluorescence, fluorescence excitation and Zeeman experiments were performed to characterize the crystal field levels of 0.1% Tm^{3+} in Y_2SiO_5. Small splittings of only 13 cm^{-1} (site 1) and 1.6 cm^{-1} (site 2) were found for the lowest components of the $^3H_6$ ground state multiplet. The homogeneous linewidth of the $^3H_6 \rightarrow {}^3H_4$ transition was also measured yielding widths of 57 kHz (site 1) and 241 kHz (site 2) in zero magnetic field. These unexpectedly large widths were attributed to the accidental magnetic sensitivity of Tm^{3+} in this host due to the presence of enhanced nuclear magnetic moments resulting from the energy level structure.

CHAPTER 1

INTRODUCTION

The lanthanides, more commonly called the rare earths (Z = 57 - 71), lie between Barium and Hafnium in the periodic table. Insulators containing rare earth ions comprise a unique and extremely important class of solid state materials. The triply-ionized rare earths have an unfilled 4f electron shell that is shielded by outer filled $5s^2$ and $5p^6$ electron shells. In free space, the electronic structure of the 4f electrons is characterized by 2J+1-fold degenerate J-multiplets, with spacings resulting from the coulomb repulsion and spin-orbit interactions. In a solid, the "crystal field" acts only as a moderate perturbation on these multiplets because of the screening by the outer filled $5s^2p^6$ shells. The electronic structure of the rare earths in a solid can thus be treated as that of a free ion perturbed by a local crystal field specific to a given host material. As a result, rare earth ions in virtually any solid exhibit extremely sharp optical spectra originating from f to f electron transitions between crystal field levels of the $4f^n$ configuration. These properties make rare-earth-doped insulators ideal candidates for a wide variety of spectroscopic studies and applications. The clear and unambiguous nature of the spectra from rare earth activated solids allows for interpretation that provides insight not only into the material being studied, but also into the general area of solid state physics.

Motivation

The same properties that make rare earth doped solids interesting for fundamental scientific research also make them extremely valuable for application in a wide variety of commercial devices including solid state laser systems and optical fiber amplifiers. Recently, rare earth doped crystals have been shown to be of interest for application in new optical memory and signal processing devices based on persistent spectral hole burning (PSHB) and coherent transient phenomena.[1-11] Such devices have the potential to dramatically increase optical storage densities and provide extremely high speed data access.[1-11] In signal processing applications, these devices allow for processing of amplitude-, phase-, and frequency-modulated signals at GHz data rates.[11]

In rare-earth-doped crystals, the spectral width of a transition is due to several interactions that can be classified into two major categories: homogeneous and inhomogeneous broadening. Homogeneous broadening is due to dynamic perturbations on the transition frequency due for example to phonons or fluctuating nuclear and electronic spins of the host lattice. Inhomogeneous broadening results from variations in the local environments of the dopant ions and can arise from static lattice strains and crystal defects. For rare earth crystals at low temperature, the spectral width of the lowest level of a J-multiplet is usually dominated by inhomogeneous broadening with a width of a several GHz and a homogeneous linewidth that can be several orders of magnitude smaller. These differences in the linewidths can be exploited for use in optical memories. In frequency domain PSHB memory applications, data is stored as "structure" in a normally smooth inhomogeneously broadened absorption lineshape. This is accomplished by "burning holes" in the absorption profile by exposing the crystal to a narrow bandwidth laser that is resonant with some portion of the inhomogeneous line. This process selectively bleaches the absorption at the laser frequency by depleting the ground state population of ions resonant with the laser creating a "hole" in the inhomogeneously broadened line that is one bit of information. The width of these holes is limited by the homogeneous linewidth, and therefore the limit on the number of holes or bits which can be stored within the inhomogeneous profile is in principle determined by the ratio of the inhomogeneous to homogeneous linewidths Γ_{inh}/Γ_h. Thus a narrow homogeneous linewidth is important to obtain high storage densities.

In the time domain, information is stored in the form of optical pulse trains using stimulated photon echoes. The length of the pulse trains is limited by the homogeneous dephasing time, or coherence time, T_2. Thus from the time domain point of view, long coherence times allow the storage of information in the form of long optical pulse trains within the coherence time of the material system[2,3]. Long dephasing times in the time domain are exactly the same as narrow homogeneous linewidths in the frequency domain since $T_2 = 1/(\pi\Gamma_h)$. It is clear that the performance limits of such PSHB devices are material dependent. As a result, it is important to perform extensive material studies in order to characterize the potential of a given rare earth doped crystal for use in such applications. This thesis presents studies of three materials: Eu^{3+}:Y_2SiO_5, Pr^{3+}:Y_2SiO_5, and Tm^{3+}:Y_2SiO_5, that have recently been shown[4,6-9] to have potential for application in

PSHB memory and signal processing devices. The fundamental material properties which determine the ultimate performance limits of the material have been explored using a variety of linear and non-linear spectroscopic techniques.

In addition to applications in optical memories, sharp optical resonances (or long coherence times) are important in that they provide very sensitive probes of small interactions or external perturbations such as superhyperfine coupling[12,13], tunneling splittings[14], nuclear Zeeman effects[15], or Stark coefficients involving fields as small as mV/cm.[16]

Measurement Techniques

The measurement of sub-kHz wide optical resonances in the frequency domain puts very stringent requirements on laser frequency stability and has not yet been achieved directly in a solid state system, although it has been demonstrated in gases, or rather in trapped single ions.[17] The use of photon echoes in the time domain overcomes this need for stability, since the Fourier width of the excitation pulses can be chosen to be greater than the laser frequency jitter and this prepares a relatively broad packet in the inhomogeneous line; the second pulse of the echo sequence removes the inhomogeneous contribution to the linewidth.[18] On the other hand, for spectral hole burning or optical free induction decay it is necessary to prepare a very sharp packet, less than the homogeneous linewidth. One drawback with the photon echo technique is the possibility of exciting echo modulation due to coherent preparation of three or more levels.[19] In cases where small splittings fall within the bandwidth of the excitation pulses, even a weak modulation can seriously distort the echo decays. Chapter 2 provides a more detailed description of the concepts of hole burning and related techniques and the theory of coherent transients and their application in optical memories. Chapter 3 describes the experimental apparatus used for the measurement of photon echoes and for the other spectroscopic techniques used in the studies presented in this thesis.

Materials Studies

The optical dephasing time of isolated ions in solids can become very long at low temperatures [20]. At temperatures below about 2 K, dephasing times of optical transitions from the ground state to metastable levels in rare-earth doped crystals are usually limited by nuclear spin fluctuations. In the search for long coherence times, host materials have been chosen whose constituent ions have zero nuclear spin such as oxygen, low isotopic abundance of nuclear spins such as Si, or small magnetic moments such as yttrium. In this way and using long-lived metastable optical levels, subkilohertz wide optical resonances have been observed in Eu^{3+}:Y_2O_3[21,22], Eu^{3+}:Y_2SiO_5[23], and Eu^{3+}:$YAlO_3$[24,25] and resonances only several kHz wide in others such as Pr^{3+}: $YAlO_3$[18,26], Pr^{3+}:YAG[27], and Cr^{3+}:Al_2O_3.[28] We recently reported the measurement of a 122 Hz wide optical resonance in Eu^{3+}:Y_2SiO_5 - the narrowest yet observed in a solid and limited only by the population decay time T_1.[29]

Eu^{3+}:Y_2SiO_5

The Y_2SiO_5 host is an ideal one in many ways, as nuclear spins have been minimized and large crystals of good optical quality can be produced, primarily as a result of the demand for its use as a laser material.[30-32] Chapter 4 presents studies of Eu^{3+}:Y_2SiO_5 where we have used photon echoes to measure what we believe to be the longest dephasing time (i.e., the sharpest optical resonance) yet reported in a solid: T_2 = 2.6 ms for Eu^{3+} ions in Y_2SiO_5 at 1.4 K. This corresponds to an optical resonance width of 122 Hz (or a resonant $Q \geq 4 \times 10^{12}$). Most of the more than 8 orders of magnitude between this value and that of the room temperature width (~ 60 GHz) comes from phonon scattering and phonon absorption processes which usually become negligible below ~ 4 K for rare-earth or transition-metal ion impurity systems. The remaining sources of dephasing are population decay by radiative or nonradiative processes or dynamic local fields due either to nuclear spin fluctuations of the host lattice nuclei, in the present case ^{89}Y, or to the presence of other excited ions (so-called "instantaneous diffusion").

The $^7F_0 \rightarrow {}^5D_0$ transition of the Eu^{3+} ion is a good choice for these studies because the electronic magnetic moment is quenched in the $^7F_0$ ground state and is very small in the $^5D_0$ excited state[33], making the transition frequency insensitive to magnetic fluctuations. Further, the excited state lifetime of ~1 ms in many materials contributes only ~100 Hz to the total linewidth and allows one to study other sources of dephasing with great sensitivity. For example, most of the compounds studied contain yttrium, because yttrium can be substituted by trivalent rare-earth ions without charge compensation and the fluctuating local fields due to the ^{89}Y nucleus are expected to be small since its magnetic moment is only $-0.14\mu_N$. By reducing other sources of line broadening, we have for the first time determined the contribution of the yttrium nucleus to optical line broadening and for the $^7F_0 \rightarrow {}^5D_0$ transition of Eu^{3+} found it to be only about 100 Hz. In all the work by other groups cited above, the lifetime (T_1) limited value was not reached, although efforts to remove the effects of nuclear spin fluctuations by coherent spin decoupling[34,35] or choice of host matrix[18,21,23] led to substantial linewidth reductions. One of the effects which makes it difficult to achieve the T_1 limit is excitation-density-dependent instantaneous diffusion in which time varying fields produced by optical excitation of neighboring ions contribute to dephasing.[22,36-44] As coherence times become longer, the possibility that phonon contributions may contribute ~100 Hz needs to be kept in mind and the sample temperature carefully monitored.

$Pr^{3+}:Y_2SiO_5$

Like the Eu^{3+} ion, Pr^{3+} is a good choice for low sensitivity to dynamic local fields since it is an even electron ion so that in crystallographic sites with lower than axial symmetry the levels are electronic singlets where the orbital angular momentum is quenched. Chapter 5 describes an investigation of optical dephasing of the Pr^{3+} ion in Y_2SiO_5. As in the case of $Eu^{3+}:Y_2SiO_5$[29] we find two contributions to T_2 - one that is magnetic in origin, involving magnetic field-dependent ^{89}Y nuclear spin fluctuations, and another that is due to field-independent population decay. For site 2 where the Pr^{3+} ion has the smaller enhanced nuclear moment, the magnetic contribution can be largely suppressed, giving near-T_1-limited dephasing. For site 1, a contribution of several hundred Hz remains due to spin-induced dephasing. These results were obtained after a detailed investigation of the contribution of instantaneous diffusion. Our studies show that, as in the case of Eu^{3+}:Y_2SiO_5, Pr^{3+}:Y_2SiO_5 is a useful material for demonstrations of time-domain storage and processing and it has an advantage that Pr^{3+} ions in site 1 have an oscillator strength two orders of magnitude higher than that in the Eu^{3+} material.

<u>Tm^{3+}:Y_2SiO_5</u>

Tm^{3+} is of particular interest because it has a transition at ~ 800 nm which is accessible with commercially available diode lasers. The Eu^{3+} and Pr^{3+} ions have been the primary rare earth ions of interest for optical memory applications, since, in addition to their insensitivity to the magnetic properties of the host lattice spins, they also have a nuclear spin of 5/2 that results in hyperfine structure in the electronic singlets. The hyperfine structure provides a mechanism for persistent spectral hole burning that is necessary for memory applications. For signal processing applications, however, only long dephasing times are necessary. The Tm^{3+} ion has a nuclear spin of 1/2 and therefore does not have hyperfine structure or a mechanism for persistent spectral hole burning, but it is of considerable interest for signal processing applications.

Chapter 6 presents studies of Tm^{3+} doped Y_2SiO_5. The Y_2SiO_5 host has been shown to be a nearly ideal host for achieving long dephasing times.[29] Previous studies of

Tm^{3+} showed that even in a host like YAG with large magnetic moments present (the aluminum magnetic moment is -3.6 μ_N) the $^3H_6 \rightarrow {}^3H_4$ transition has a long fluorescence lifetime of ~800 μs and a relatively long coherence time of T_2 = 105 μs.[45] This corresponds to a homogeneous linewidth of ~3 kHz. Measurement of the dephasing times of Tm^{3+} in Y_2SiO_5 yielded unexpectedly short values of $T_2 \cong 5$ μs. Spectroscopic studies of the Tm^{3+} crystal field levels show much more complicated spectra than expected for such a low symmetry site. Small ground state crystal field splittings were found that contribute to an enhanced nuclear magnetic moment which may explain the anomalously rapid dephasing seen in the photon echo experiments. At present, Tm^{3+}YAG remains the best candidate for use in diode laser pumped signal processing devices.

CHAPTER 2

SPECTRAL HOLEBURNING AND PHOTON ECHOES

Homogeneous and Inhomogeneous Broadening

There are two main classes of line broadening, homogeneous and inhomogeneous, that give rise to the observed spectral width of optical transitions of rare earth ions in real crystals. Homogeneous broadening of a spectral line is experienced equally by all ions in the solid and is due to dynamic fluctuations in the local crystal field or magnetic environment that act as perturbations on the transition frequency of the ion of interest. For rare earth doped solids, these dynamic perturbations on the transition frequency are typically a result of phonons and fluctuations of nuclear and electronic spins of the host lattice. In contrast to homogeneous broadening due to dynamical processes, inhomogeneous broadening is due to any static perturbation that makes the local environment around one ion in the solid different from that of another ion. These variations in the local crystal field are due to static lattice stresses and strains, crystal defects, and impurities. Inhomogeneous broadening mechanisms result in a distribution of transition frequencies which reflect the various local environments in the crystal. This is shown schematically in figure 2.1 for an inhomogeneously broadened transiton of width Γ_{inh}, where each homogeneously broadened packet of width Γ_h represents a given

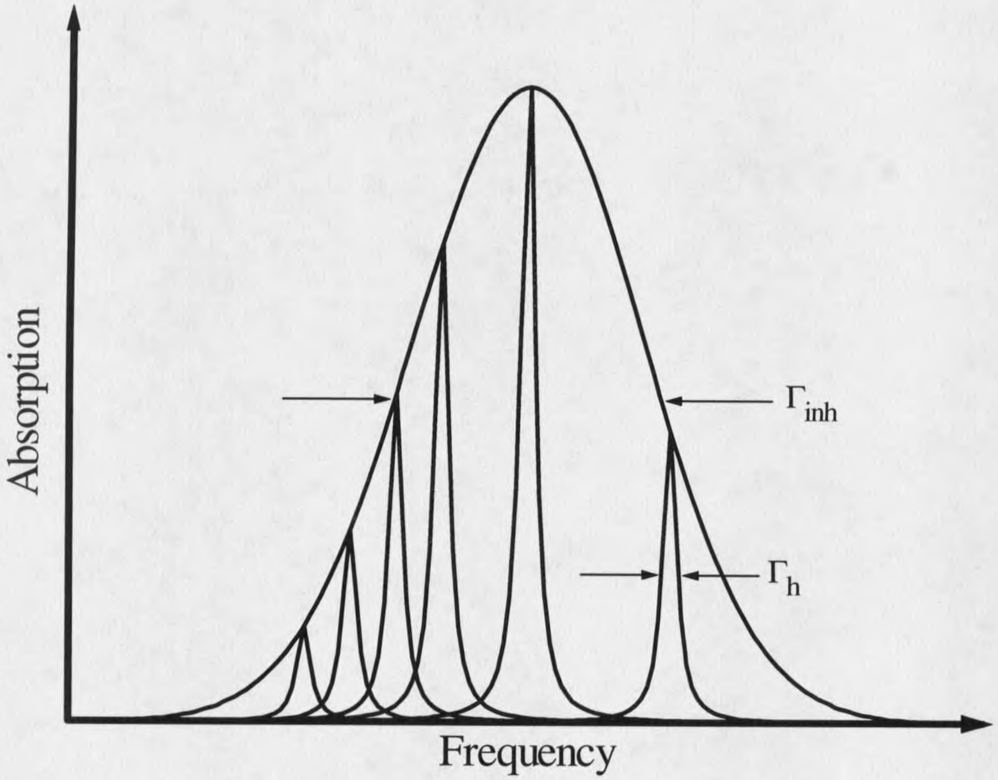

Figure 2.1 Inhomogeneous and homogeneous linewidths shown schematically for the lowest level in a J-multiplet. The homogeneous width is much smaller than the inhomogeneous width. Each homogeneously broadened "packet" represents a group of ions in the crystal that experience the same local environment.

group of ions which experience the same local environment. In rare earth doped crystals at liquid helium temperatures, the upper components of a given J-multiplet tend to have homogeneous linewidths comparable to or greater than the inhomogeneous width. This is primarily due to spontaneous phonon emission to the other lower levels in the multiplet. However, the observed spectral width of the lowest level of the multiplet is usually dominated by inhomogeneous broadening with a linewidth of a few GHz to a few

10's of GHz, and homogeneous widths of a few hundred Hz to Mhz or GHz. For studies or applications where long fluorescence lifetimes and narrow homogeneous linewidths are important, the lowest level of a manifold is typically the only state of that J-multiplet which is of interest. Since optical memory applications require these properties, the studies in this thesis were performed on transitions which are inhomogeneously broadened. While this is necessary for optical memory applications, the inhomogeneous linewidth obscures other important spectroscopic information like hyperfine or superhyperfine splittings which are on the order of kHz - MHz. The homogeneous linewidth itself contains information about the dynamics of the system and is also buried within the inhomogeneously broadened profile. Conventional spectroscopic techniques can quite easily allow for measurement of the inhomogeneous linewidth by performing a simple absorption experiment where the intensity of the transmitted light is monitored as a function of frequency. It is however a much more difficult task to determine the homogeneous linewidth, and nonlinear spectroscopic techniques must be employed to gain the extremely high resolution required to measure these structures. In the frequency domain, spectral holeburning and optically detected nuclear magnetic resonance (ODNMR) are two of the most widely use techniques, and they will be discussed in the next section. In the time domain, photon echoes and related techniques like photon echo nuclear double resonance (PENDOR) are used and are discussed in greater detail later in this chapter.

Spectral Holeburning

Basic Mechanisms

In spectral hole burning, a laser is used to selectively excite a narrow portion of the inhomogeneously broadened line. The ions which are resonant with the laser are pumped from the ground state to an excited state. These ions can then relax back to the ground state or to some other levels of the system which can act as population reservoirs. Those ions which relax back to the ground state are excited again and have another chance to decay to the other reservoir levels. In this manner, it is possible to deplete the ground state population of ions that are resonant with the laser. This selective bleaching of the absorption by the pump laser results in a spectral "hole" that may be observed by scanning the frequency of a low intensity laser across the inhomogeneously broadened line. When the low intensity laser is resonant with the original pump laser, a decrease in the absorption (increase in the transmission) is observed due to the depletion of the ground state population of ions at that frequency. This was first demonstrated in solids by Szabo in his studies of ruby,[46] and was first applied to rare earths by Erickson.[47] The holeburning process is shown schematically in figure 2.2.

The hole width and the hole lifetime are important parameters for the use of holeburning as a spectroscopic technique as well as in optical memory applications. Given a laser with a linewidth much narrower than the homogenous broadening, it is

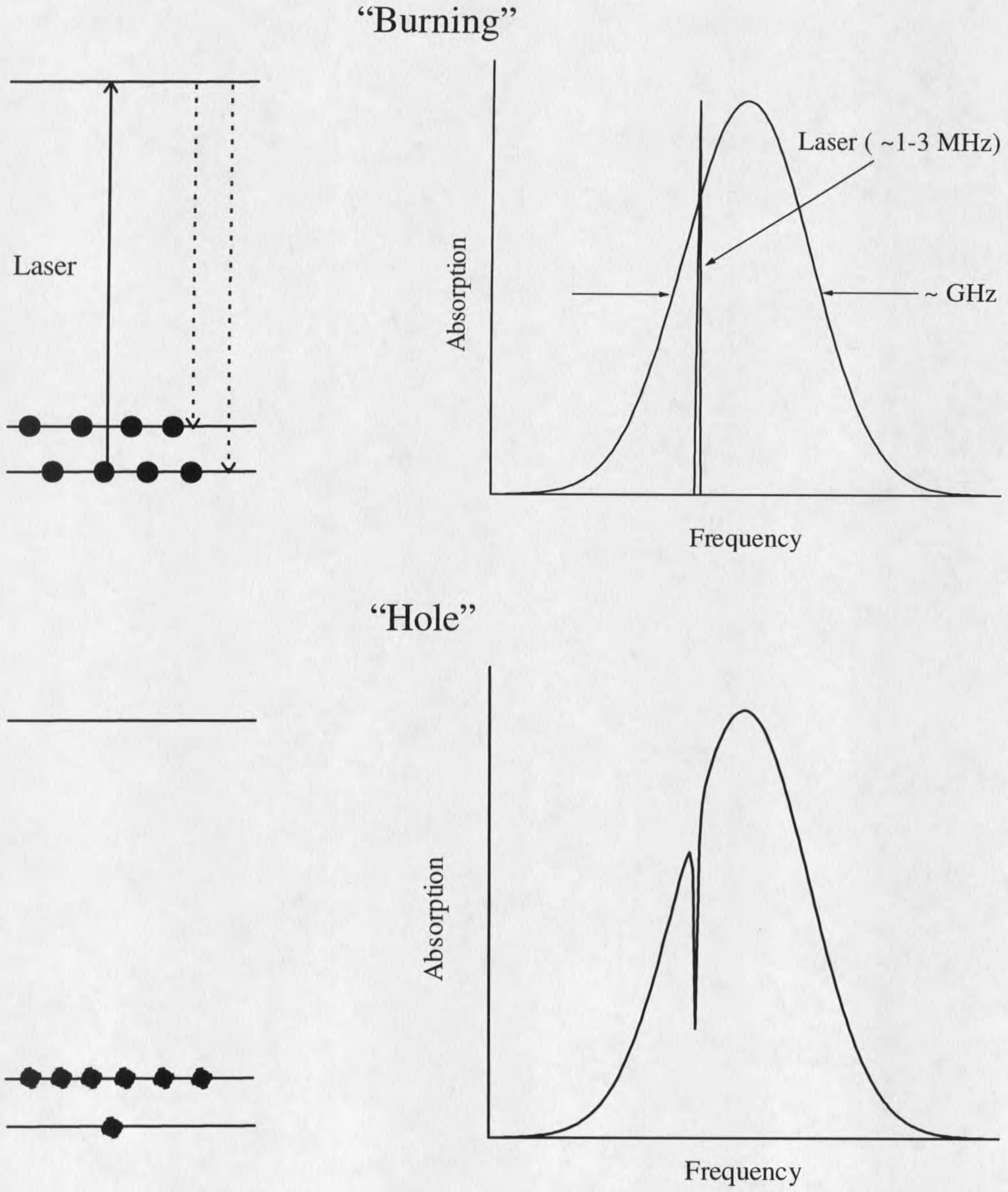

Figure 2.2 The holeburning process. A narrow band laser excites a portion of the inhomogeneous line, depleting the ground state population and enhancing the population of some other level in the system. The "Hole" can be seen as a reduction in the absorption at the frequency of the original laser.

possible to excite a single homogeneous packet, and it can be shown[48] that the hole width is twice the homogeneous linewidth plus possible power broadening effects. Commercially available single frequency cw dye lasers have jitter limited linewidths of ~ 1-3 Mhz, though, and homogeneous linewidths can be several kHz or even as narrow as a few hundred Hz. As a result, the practical resolution of the holeburning technique is determined by the stability of the laser. Much work has been done to build lasers stable to a few kHz.[49] Such lasers are not widely available though and are still too broad for use with a significant number of materials with even narrower homogeneous linewidths

The lifetime of a spectral hole is determined by the lifetime of the population reservoir and for the lowest level in a J-multiplet can range from μsec to as long as several hours in some materials.[2] The various mechanisms for holeburning in rare earth doped solids, shown in figure 2.3, are classified by the type of population reservoir in which the ions are stored after optical pumping from the ground state. The simplest case uses two level saturation of the absorption as the holeburning mechanism, where the excited state acts as the population reservoir. The lifetime of the hole is determined by the lifetime of the excited state, typically μsec to msec. Longer hole lifetimes can be achieved in systems where a third metastable state or hyperfine or superhyperfine structure acts as the population reservoir. Holeburning of the $^3H_6 \rightarrow {}^3H_4$ transition of the Tm^{3+} ion uses a three level scheme like that shown in figure 2.3b with the $^3F_4$ metastable level acting as the population reservoir. For Eu^{3+} and Pr^{3+}, hyperfine levels are the population reservoir as shown in figure 2.3c, and hole lifetimes of more than 13 hours have been observed.[2] With this potential for extremely long hole lifetimes, optical

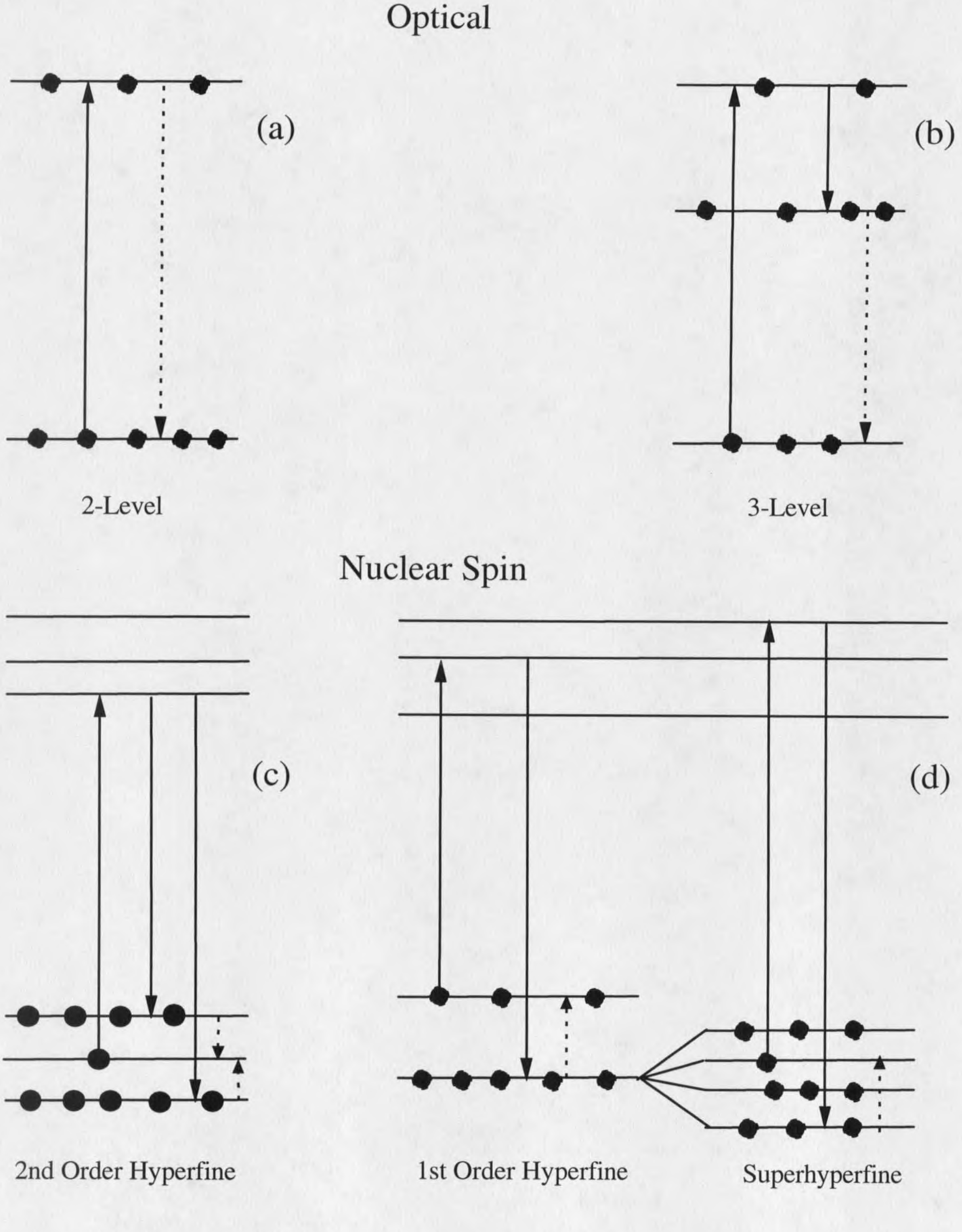

Figure 2.3 Population reservoirs for holeburning in rare earth doped solids. The solid arrows pointing up (down) show the excitation (decay) processes to (from) the excited state. The dotted arrows show the hole recovery processes that determine the lifetime of the hole.

pumping of the nuclear hyperfine levels is a very useful holeburning mechanism for the trivalent rare earths. Both Eu^{3+} and Pr^{3+} ions have a nuclear spin of 5/2 so that in zero external magnetic field there will be three Kramers doublet nuclear hyperfine levels associated with each electronic state. In the case of Eu^{3+}, there is a significant nuclear quadrupole interaction that splits the hyperfine levels of the $^7F_0$ ground state and $^5D_0$ excited state by 10's of MHz. In Pr^{3+} the pure quadrupole interaction is quite weak but the second order magnetic hyperfine interaction or pseudo-quadrupole interaction splits the hyperfine levels of the ground state and lowest $^1D_2$ level on the order of 10 MHz. Holeburning is performed by using a narrow band cw laser of 1-2 MHz bandwidth to excite a single transition between the ground state and excited state hyperfine levels for one specific packet of ions in the crystal. The ground state hyperfine level which was optically pumped will have a depleted population, while the other two levels will have an excess population. If an absorption experiment is then performed, decreased absorption or holes will be seen at frequencies corresponding to transitions between the depleted level and the three excited state hyperfine levels. Enhanced absorption or antiholes will be seen at frequencies corresponding to transitions from the two ground state hyperfine levels with excess population. The relative intensities of the holes and antiholes will depend on the optical transition probability and thus on the overlap of the nuclear spin wave function of the ground and excited states. It is important to note that this pattern of holes and antiholes is for a single subset of ions in the solid. For the Eu^{3+} $^7F_0 \rightarrow {}^5D_0$, and Pr^{3+} $^3H_4 \rightarrow {}^1D_2$ transitions, the inhomogeneous broadening is very large compared to the splittings of the hyperfine levels, so all of the allowed transitions between every ground state hyperfine level and excited state hyperfine level will be excited for some subset of ions. As a result there will be a much more complicated pattern of holes and anti holes. For an I = 5/2 system there are 9 different subsets of ions which can result in seven holes (the main hole and 3 holes on each side called side holes) and 42 antiholes (21 on each side of the mail hole). The frequency differences between the main and side holes will give the excited state hyperfine splittings and the frequency differences between the antiholes and corresponding hole will give the ground state hyperfine splittings. It is thus possible to use holeburning as a spectroscopic tool to determine the hyperfine splittings that are masked by the inhomogeneously broadened absorption profile. As noted earlier, the resolution of this technique is limited by the laser jitter which is typically a few MHz.

Optically Detected Nuclear Magnetic Resonance (ODNMR)

It is possible to greatly enhance the resolution of the measurement of hyperfine splittings by using holeburning in conjunction with an applied radio frequency (RF) field. Just as the holeburning process perturbs the population distribution among the hyperfine levels, application of a RF field resonant with the hyperfine splittings will also drive these populations. Changes in the population distribution among the hyperfine levels due to application of the RF field is detected as a change in the absorption or fluorescence intensity while burning a hole. This technique is usually referred to as optically detected nuclear magnetic resonance or ODNMR. The resolution of ODNMR is limited by the inhomogeneously broadened linewidth of the nuclear transition or the RF source rather than laser jitter. This allows one to measure the hyperfine splittings at least an order of magnitude more precisely than by holeburning.

To perform an ODNMR experiment, a laser is used to burn a hole depleting the population of one of the ground state hyperfine levels. Unlike normal holeburning where the burn laser is turned off while the hole pattern is read, the laser is left on and the absorption or fluorescence intensity is monitored while an RF field is applied to the sample. When the RF is resonant with any of the hyperfine splittings, the intensity of the holeburning will change, resulting in a change in the absorption or fluorescence intensity. When the RF is resonant with a ground state splitting, population is driven into the depleted level (hole filling) decreasing the amount of holeburning and thus increasing the absorption and fluorescence intensity. If the RF is resonant with an excited state splitting, an increase in the branching to the levels acting as population reservoirs can occur resulting in enhanced holeburning. This is seen as a decrease in absorption and fluorescence intensity. This technique is extremely useful in determining ground state hyperfine splittings but signals can be quite weak for excited state resonances. For example, in cases where the ion is in sites of non-axial symmetry, the branching among the excited states can already be strong and the RF has little additional effect. In these cases the holeburning pattern or some other technique must be used to determine the excited state splittings.

Application to Optical Memory Devices

Spectral holeburning clearly has great utility as a high resolution spectroscopic technique, but it also has been shown recently to be useful for optical memory and signal processing devices. For this application, one is usually interested in *persistent* spectral holeburning (PSHB), where persistent usually means holes with extremely long lifetimes of hours to days. In this application, the inhomogeneously broadened profile is divided into frequency bins as shown in figure 2.4. Data is then stored as a hole burned in a given frequency bin representing a binary 1, or no hole is burned representing a binary 0. The laser can then be moved to a different location in the crystal to sample a different set of ions and another set of data can be stored at this location. The ultimate limit on the number of bits that can be stored at each spot in the crystal is the ratio of the inhomogeneous to homogeneous linewidths (Γ_{inh}/Γ_h), which is typically between 10^4 to 10^6 but has been shown to be as high as 10^7 for some Eu^{3+} doped crystals.[29] As a result, this technique has the distinct advantage of increasing the storage density of optical memory devices by these factors of 10^4 to 10^7. This application of PSHB has caused a recent surge in the search for rare earth doped materials with long hole lifetimes and very narrow homogeneous linewidths. However, even given a system that meets these requirements, there are significant limitations to the use of frequency domain PSHB techniques described here.

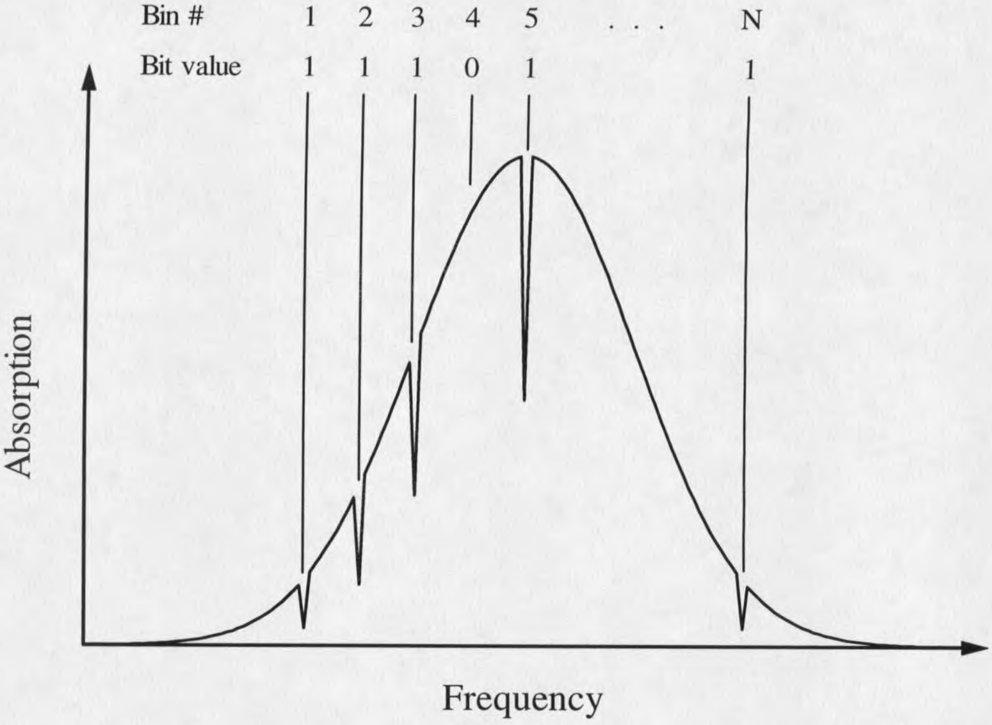

Figure 2.4 Frequency domain PSHB optical data storage. The inhomogeneously broadened absorption profile is divided into N frequency bins. A hole is either burned in a bin representing a binary 1 or not burned representing a binary 0.

One limitation is imposed by the fact that commercially available lasers have jitter limited linewidths significantly larger than the homogeneous linewidth. This causes a significant reduction in the number of holes that can be burned in a given inhomogeneously broadened profile since the hole width is limited by laser jitter rather than the homogeneous linewidth. In addition, the readout process of a hole is quite slow and must be performed on a time scale on the order of $1/\Gamma_h$ to prevent broadening of the hole by the reading process itself. Because of these limitations in the frequency domain, the time domain analog to holeburning called photon echoes is usually used in PSHB optical memory applications as well as for measurement of homogeneous linewidths.

Two Pulse Photon Echoes

Optical coherent transients in the time domain provide an alternative method to holeburning techniques for determining the homogeneous linewidth and in some cases the nuclear hyperfine or superhyperfine splittings. As described in the previous section, measurement of the homogeneous linewidth via spectral holeburning requires a laser with a linewidth narrower than the homogeneous broadening thus placing very stringent limitations on the laser stability. The photon echo technique, however, uses short pulses whose spectral width is large compared to the homogeneous broadening relaxing the need for ultra sharp laser linewidths. The effects of inhomogeneous broadening are removed by the pulse sequence itself allowing measurement of the homogeneous linewidth in the form of a characteristic dephasing time T_2 called the homogeneous dephasing time.

The two pulse photon echo experiment is performed by exciting the sample with two pulses of laser light separated in time by a delay τ. The first pulse creates a coherent superposition of the ground and excited state. This coherence in the sample is seen physically as a macroscopic oscillating dipole moment that radiates. The reradiation is referred to as an optical free induction decay (FID).[50] As time evolves the various ions excited will accumulate relative phases (dephase) due to the spread in transition energies resulting from inhomogeneous broadening. This dephasing results in a loss of coherence at a rate $T_2^* = 1/\Gamma_{exc}$, where Γ_{exc} is the spectral width of the excitation pulse or the inhomogeneous linewidth whichever is smaller. The second excitation pulse has the effect in some sense of exchanging the amplitudes of the ground and excited states in the coherent superposition. This results in a change in sign of the accumulated phase of the ions. After the second pulse the ions rephase, and at a time τ later the relative phases of the ions are zero resulting once again in a macroscopic oscillating dipole that is seen as a burst of coherent radiation called a photon echo. The amplitude of the echo will decay at a characteristic rate T_2 as the separation of the first and second excitation pulses is increased. Since dephasing due to the static effects of inhomogeneous broadening has been erased by the echo excitation sequence, the echo decay rate versus τ yields information about the dynamical processes in the solid that give rise to the homogeneous linewidth. The homogeneous linewidth is related to the dephasing time by $\Gamma_h = 1/(\pi T_2)$. Working in the time domain, the photon echo technique provides a method for measuring extremely narrow homogeneous linewidths (as narrow as 100Hz[29]) while using a laser with a much broader spectral width of 1-2 MHz.

The Density Matrix and the 2-Level System

A more detailed derivation of the photon echo process can be understood by analysis of the interaction of a two level quantum mechanical system with the radiation field of a laser.[48,51,52] In the analysis of quantum systems one typically wants to calculate expectation values of operators that represent physical observables, in this case the macroscopic polarization of the medium due to the coherent excitation of the ions by the laser field. When the state of the system is known exactly, the expectation value of an observable $\hat{A}$ for a system in the state $|\psi\rangle$ can be calculated in the normal manner as

$$\langle\hat{A}\rangle = \langle\Psi|\hat{A}|\Psi\rangle = \int \Psi^*(\mathbf{r},t)\hat{A}\Psi(\mathbf{r},t)d^3\mathbf{r}. \tag{2.1}$$

However, in many cases the exact state of the system is not known. In these circumstances an alternate approach which employs the density matrix or density operator is used to calculate expectation values. A full derivation of the density matrix formalism and its properties will not be presented here; the reader is referred to any of several excellent texts[48,51-54] for the details of this approach to quantum mechanical systems.

To introduce the density matrix, consider an isolated quantum mechanical system in a state $|\psi(\mathbf{r},t)\rangle$ given by

$$|\Psi(\mathbf{r},t)\rangle = \sum_n c_n(t)u_n(\mathbf{r}), \tag{2.2}$$

where the $u_n(\mathbf{r})$ are a complete orthonormal set of basis functions. The density operator is then defined by

$$\rho(t) = |\Psi(t)\rangle\langle\Psi(t)|, \tag{2.3}$$

with matrix elements

$$\rho_{mn} = c_m^*(t)c_n(t). \tag{2.4}$$

For an ensemble of quantum mechanical systems (like ions in a solid experiencing dynamic field fluctuations and occupying slightly different local environments due to inhomogeneous broadening) an ensemble average must be taken and the appropriate definition of the density operator is

$$\rho(t) = \sum_{\Psi} P_{\Psi} |\Psi(t)\rangle\langle\Psi(t)|, \tag{2.5}$$

where P_{Ψ} is the probability of finding the state $|\psi\rangle$ in the ensemble, and the sum is over all possible states. It can then be shown that the expectation value of an observable $\hat{A}$ is given by the trace of the matrix product of the operator and the density matrix

$$\langle\hat{A}\rangle = \mathrm{Tr}(\rho\hat{A}) = \sum_{n} (\rho\hat{A})_{nn}. \tag{2.6}$$

Thus once the density matrix is known, one can calculate expectation values of any observable. It is also important to note the physical meaning of the density matrix elements. The diagonal matrix elements $\rho_{nn} = |c_n(t)|^2$ represent populations of the system in the nth state, while the off-diagonal elements $\rho_{mn} = c_m^*(t)c_n(t)$ represent the coherence between the mth and nth state. Dynamical operators like the density operator satisfy the Liouville equation

$$\frac{\partial\rho(t)}{\partial t} = -\frac{i}{\hbar}\left[\hat{H}, \rho(t)\right], \tag{2.7}$$

where $\hat{H}$ is the Hamiltonian of the system.

Photon Echo Formation

Let us consider a two level system with eigenstates $|1\rangle$ and $|2\rangle$ described by a Hamiltonian $\hat{H}_0$ such that: $\hat{H}_0|1\rangle = E_1|1\rangle$, and $\hat{H}_0|2\rangle = E_2|2\rangle$. Let the zero of energy be E_1 and $E_2 = \hbar\omega$. The most general wave function for the system can be written as $|\Psi(t)\rangle = c_1(t)\ |1\rangle + c_2(t)e^{-i\varphi}\ |2\rangle$. If the system is exposed to an electric field $\mathbf{E}(t) = E_x(t)\hat{x} + E_y(t)\hat{y}$, and the states are coupled by an electric dipole interaction, the interaction Hamiltonian is

$$\hat{H}_i = -\mu \bullet \mathbf{E(t)} = -\left(\mu_x E_x + \mu_y E_y\right) = -\frac{1}{2}\left(\mu^+ E^- + \mu^- E^+\right), \tag{2.8}$$

where we have made the definitions $E^{\pm} \equiv E_x \pm iE_y$ and $\mu^{\pm} \equiv \mu_x \pm i\mu_y$. The transition dipole matrix elements are then defined as

$$\mu^-_{12} = \mu^+_{21} \equiv 2\mu, \text{ and } \mu = \langle 2|\mu_x|1\rangle. \tag{2.9}$$

The dynamical response of the system is governed by

$$\frac{\partial\rho}{\partial t} = \left[\hat{H}_0 + \hat{H}_i + \hat{H}_{relax}, \rho\right], \tag{2.10}$$

where $\hat{H}_{relax}$ is the relaxation Hamiltonian describing all processes effecting the relaxation of the system to thermal equilibrium as well as processes which result in loss of phase coherence.[54-59] Due to the complexity of these relaxation interactions, they are often dealt with in a phenomenological manner.[51,60] Equation 2.8 for the density matrix elements of our two level system becomes

$$\frac{\partial \rho_{22}}{\partial t} = -\frac{i}{\hbar}\left[(H_i)_{12}\rho_{21} + (H_i)_{21}\rho_{12}\right] - \frac{i}{\hbar}\left[\hat{H}_{relax}, \rho\right]_{22}, \tag{2.11a}$$

$$\frac{\partial \rho_{21}}{\partial t} = -i\omega_0\rho_{21} - \frac{i}{\hbar}(H_i)_{21}\left[\rho_{11} + \rho_{22}\right] - \frac{i}{\hbar}\left[\hat{H}_{relax}, \rho\right]_{21}, \tag{2.11b}$$

$$\frac{\partial \rho_{12}}{\partial t} = \frac{\partial \rho_{21}^*}{\partial t}, \tag{2.11c}$$

$$\frac{\partial \rho_{11}}{\partial t} = -\frac{\partial \rho_{22}}{\partial t}. \tag{2.11d}$$

It is quite illustrative to rewrite equations 2.11 in a form first contrived by Block[61] and later Feynman, Vernon and Hellwarth[62] who developed a geometrical interpretation of this interaction by defining a pseudo-dipole vector

$$\mathbf{R} = r_1\hat{1} + r_2\hat{2} + r_3\hat{3}, \tag{2.12}$$

with components

$$r_1 = \rho_{21} + \rho_{12}, \tag{2.13a}$$

$$r_2 = i(\rho_{21} - \rho_{12}), \tag{2.13b}$$

$$r_3 = \rho_{22} - \rho_{11}, \tag{2.13c}$$

and a pseudo-field vector

$$\Omega = \frac{2}{\hbar}\mathrm{Re}(H_i)_{21}\hat{1} - \frac{2}{\hbar}\mathrm{Im}(H_i)_{21}\hat{2} + \omega\hat{3}. \qquad (2.14)$$

Equations 2.11 can now be written in the classic form

$$\frac{\partial \mathbf{R}}{\partial t} = \Omega \times \mathbf{R} + \frac{1}{T_2}\left(r_1\hat{1} + r_2\hat{2}\right) + \frac{r_3}{T_1}\hat{3}, \qquad (2.15)$$

known as the optical Block equation.[61] The relaxation terms in equation 2.15 were added phenomenologically. The term associated with the diagonal elements of the density matrix namely r_3 is characterized by a time T_1 which represents population decay from the excited state to the ground state. T_1 is called the fluorescence lifetime or longitudinal relaxation time. The decay of off diagonal elements of the density matrix (r_1 and r_2) is characterized by T_2 which describes the loss of coherence or "dephasing" of the system. T_2 is usually called the dephasing time or transverse relaxation time.

If we neglect the effects of relaxation for a moment, equation 2.15 indicates that the pseudo-dipole vector **R** precesses around the pseudo-field vector **Ω** which is rotating at the frequency of the applied electric field. This can be compared directly to the precession of a magnetic moment **M** about an oscillating magnetic field **H** in a magnetic resonance experiment. Therefore a direct analogy can be made between photon echoes and spin echoes.

Now consider the specific case where our two level system is exposed to a series of circularly polarized laser pulses as shown in figure 2.5. If the applied electric field is in the x, y plane, then $\mathbb{E}(t) = E\cos(\omega_0 t)\hat{x} + E\sin(\omega_0 t)\hat{y}$ so that the pseudo-field vector has components $\Omega_1 = -2\mu E\cos(\omega_0 t)/\hbar$, $\Omega_2 = -2\mu E\sin(\omega_0 t)/\hbar$, $\Omega_3 = \omega$ and is also circularly polarized in the 1,2 plane. As noted above, the pseudo-dipole precesses about this pseudo-field vector which is itself rotating at angular frequency ω_0. This results in some rather wild gyrations in the stationary 1,2,3 coordinate system. It is therefore very useful to transform to a reference frame rotating about the 3 axis at a frequency ω_0 defined by the axes

$$\mathrm{I} = \cos(\omega t)\hat{1} + \sin(\omega t)\hat{2}, \tag{2.16a}$$

$$\mathrm{II} = -\sin(\omega t)\hat{1} + \cos(\omega t)\hat{2}, \tag{2.16b}$$

$$\mathrm{III} = \hat{3}. \tag{2.16c}$$

In this reference frame the problem is simplified to the precession of the pseudo-dipole vector about a stationary pseudo-field vector that now has components $\Omega_{\mathrm{I}} = -2\mu E/\hbar$, $\Omega_{\mathrm{II}} = 0$, $\Omega_{\mathrm{III}} = \omega$. The equation of motion for the pseudo-dipole vector in the rotating frame is still of the same form as equation 2.15

$$\begin{aligned}\frac{\partial \mathbf{R}_{\mathrm{rot}}}{\partial t} &= \left[\left(-\frac{2\mu E}{\hbar}\right)\hat{\mathrm{I}} + (\omega - \omega_0)\hat{\mathrm{III}}\right] \times \mathbf{R}_{\mathrm{rot}} + [\mathrm{Relaxation\ terms}] \\ &\equiv \Omega_{\mathrm{eff}} \times \mathbf{R}_{\mathrm{rot}} + [\mathrm{Relaxation\ terms}]\end{aligned} \tag{2.17}$$

where the subscript "rot" indicates the vector transformation to the rotating coordinate system. It is important to note that Equation 2.17 describes the time evolution of a

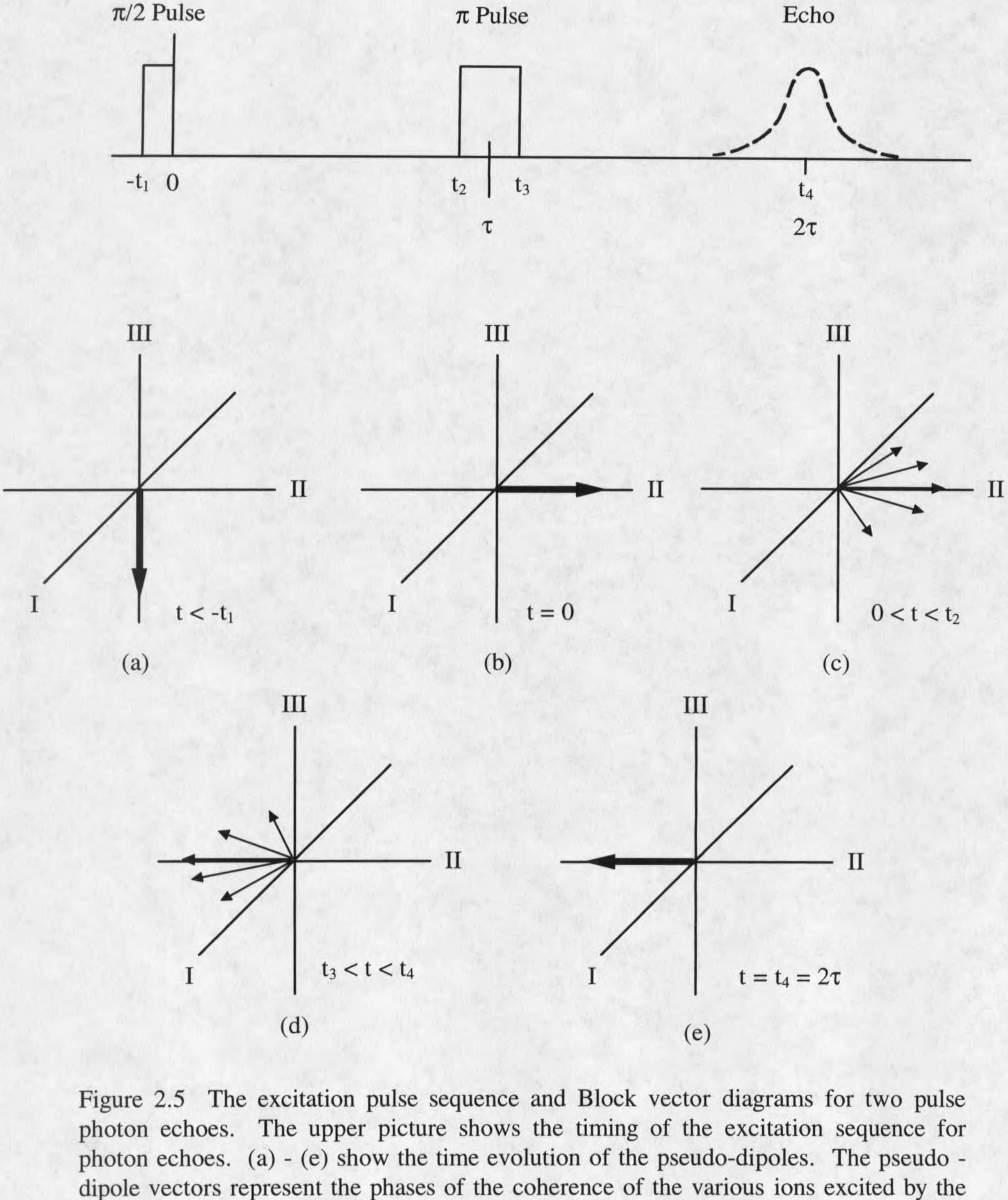

Figure 2.5 The excitation pulse sequence and Block vector diagrams for two pulse photon echoes. The upper picture shows the timing of the excitation sequence for photon echoes. (a) - (e) show the time evolution of the pseudo-dipoles. The pseudo - dipole vectors represent the phases of the coherence of the various ions excited by the pulse sequence. (This figure follows Levenson.[51])

single two-level system and therefore one group of ions that all experience the same local environment and thus have the same transition energy. If the ions are initially all in the ground state at time $t = -t_1$, all the pseudo-dipole vectors point along the -III direction as shown in figure 2.5a. During the interval $-t_1 \leq t \leq 0$ the system is exposed to the electric field of the first laser pulse. If we assume that the Rabi frequency $\mu E/\hbar$ is much greater than the detuning $\Delta \equiv \omega - \omega_0$, then the pseudo-dipoles will rotate about the strong applied field along the -I axis by an angle

$$\Theta_1 = \int_{-t_1}^{0} (\mu E / \hbar) dt \tag{2.18}$$

called the pulse area. Ideally, $\Theta_1 = \pi/2$ so that all the pseudo-dipole vectors for the ensemble of ions are along the II axis as in figure 2.5b. During the time interval between the two laser pulses the individual **R** vectors for the various ions rotate about the III axis (as described by equation 2.17 with $E = 0$) at a variety of rates determined by the detuning Δ_i for each ion. This "fanning out" of the pseudo-dipole vectors, shown in figure 2.5c, results in a loss of coherence and therefore a decay of the radiating macroscopic dipole moment called FID as noted earlier. At a time t_2 a second laser pulse is applied, again causing the pseudo-dipole vectors to rotate about the -I axis by an angle

$$\Theta_2 = \int_{t_2}^{t_3} (\mu E / \hbar) dt = \pi, \tag{2.19}$$

as shown in figure 2.5d. After the second pulse, the pseudo-dipoles continue to rotate about the III axis in the same manner as before the second pulse. At a time $t_4 = 2\tau$ twice the time interval between the pulses, all the pseudo-dipoles are once again in phase resulting in a coherent pulse of radiation which is the photon echo.

In the previous discussion of the formation of the photon echo, relaxation processes have been neglected. While the photon echo process does reverse dephasing due to static inhomogeneous broadening, dynamic processes result in dephasing that cannot be reversed. If relaxations are not neglected, the solution to equation 2.17 for the individual pseudo-dipoles between the two pulses becomes

$$\mathbf{R}_\Delta = \left(\sin(\Delta t)\hat{\mathrm{II}} + \cos(\Delta t)\hat{\mathrm{I}}\right)e^{-t/T_2} + r_{\mathrm{III}}\hat{\mathrm{III}}. \tag{2.20}$$

Now, in addition to the dephasing associated with the rotation of the pseudo-dipoles about the III axis, the length of these vectors decay with time as e^{-t/T_2}. Thus when the pseudo-dipoles have rephased at $t = 2\tau$, the amplitude of the macroscopic dipole moment will have decayed by the factor $e^{-2\tau/T_2}$. Therefore the intensity of the photon echo will decay as a function of the separation between the first and second laser pulse as a simple exponential

$$I(\tau) = I_0 e^{-4\tau/T_2}, \tag{2.21}$$

allowing measurement of the homogeneous dephasing time T_2.

In real experimental situations, conditions are rarely as ideal as those depicted in the derivation above. Fortunately, photon echoes will actually occur under far more general conditions. Specifically, the pulse areas Θ_1 and Θ_2 are often significantly less than the ideal values of $\pi/2$ and π, but still produce photon echoes nearly as strong as the ideal case. For arbitrary pulse areas, the photon echo intensity will be modified by a factor $\{(\sin^2(\Theta_2/2)\sin(\Theta_1))^2\}$.[63,64] In addition to the less than ideal conditions encountered in real experiments, the physical systems studied are not always modeled by a simple two level system. In some cases, the ground and/or excited states have hyperfine or superhyperfine splittings which are less than the Fourier width of the exciting laser pulses. When this occurs, interference or quantum-beats between the coherences excited for the various transitions result in an echo decay that modulates at the frequencies of the ground and excited state splittings and their sums and differences.[19,65,66] In the case of nuclear hyperfine splittings, the explicit functional form of the echo modulation will depend on the overlap of the nuclear spin wavefunctions for the ground and excited state. The structure of this type of echo decay curve makes measurement of the homogeneous dephasing time difficult; however, Fourier transforming the resulting echo decay curve gives the superhyperfine or hyperfine splittings.

Even in the absence of echo modulation, where a system can be modeled by a two level picture, the echo decay curves are not always a simple exponential. If the dephasing is due to a reservoir whose dynamics change on the same time scale as the echo decay time T_2, very non-exponential decays will result.[67] Rare earth doped crystals often exhibit nonexponential decays when the strong magnetic moment of the rare earth ion perturbs the nuclear spin dynamics of atoms in the host lattice.[45,68-74] This large magnetic moment causes a "frozen core" of nuclear spins surrounding the rare earth ion resulting in an inhomogeneous distribution of spin fluctuation rates and a nonexponential echo decay.

Stimulated Photon Echoes

In addition to the two pulse photon echo described in the previous section, several other types of photon echoes can be created by using more elaborate pulse sequences. The stimulated photon echo involves the use of three excitation pulses and can be thought of in terms of the two pulse photon echo $\pi/2$ and π pulses where the π pulse has been broken into two $\pi/2$ pulses separated by a long delay T. This pulse sequence is shown in figure 2.6. The first pulse creates a coherent superposition of the ground and excited states as in the case of the two pulse echo. In terms of the Block vector model of equation 2.17, the first pulse puts all the pseudo-dipoles in the I, II plane along the II axis. The pseudo-dipoles then dephase in the I,II plane as in the previous discussion of two pulse echoes. The second pulse is now a $\pi/2$ pulse and rotates the $\mathbf{R}_\Delta$ vectors into a plane containing the III axis. In effect, the second pulse stores the coherence present at time t_2 as a pattern of population differences (often called a population grating) in the ground and excited states. The population grating will decay at the longitudinal rate T_1 which can be much longer than the dephasing time T_2. Thus in

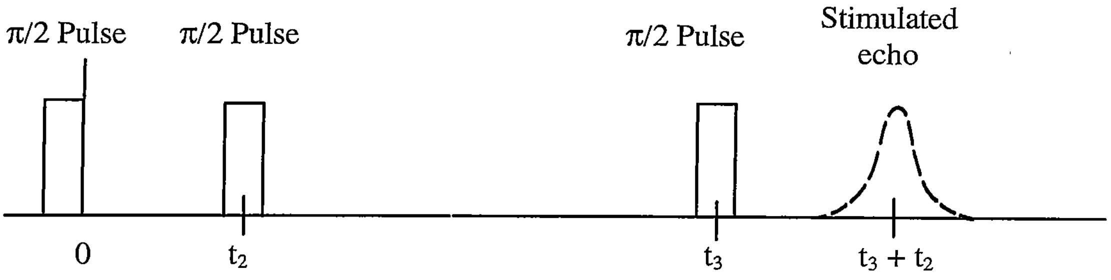

Figure 2.6 Excitation pulse sequence for stimulated photon echoes. The second pulse stores the coherence information present at t_2 in the form of a population difference which varies as a function of frequency across the inhomogeneous line.

between the second and third pulses, the transverse components of the $\mathbf{R}_\Delta$ can relax to zero but the longitudinal components will still be non-zero. The third π/2 pulse rotates the longitudinal components of the pseudo-dipoles back into the I, II plane where they rephase as in the second half of the two pulse echo sequence. At a time t_2 after the third pulse the pseudo-dipoles are in phase again and radiate the stimulated echo.

For the above description, the amplitude of the stimulated echo would depend on the pulse 1- pulse 2 separation t_2 and the pulse 2 - pulse 3 separation $t_{32} = t_3 - t_2$ as

$$E_{\mathrm{echo}}(t_2 + t_3) \propto e^{-(t_3 - t_2)/T_1} e^{-t_2/T_2}. \tag{2.22}$$

Thus the stimulated echo allows for measurement of both the longitudinal and transverse relaxation times in a single experiment. In some systems, it is possible for the excited state to decay to a long lived reservoir other than the ground state. An example of such reservoirs are nuclear hyperfine levels associated with the ground state. In this case the excited state population grating will still decay in a time T_1, but the grating in the ground state will decay at a different rate corresponding to the spin-lattice relaxation time T_{sl}. The time dependence of the stimulated echo amplitude will be given by

$$E_{echo}(t_2+t_3) \propto \frac{1}{2}\left(e^{-(t_3-t_2)/T_1} + e^{-(t_3-t_2)/T_{sl}}\right)e^{-2t_2/T_2}. \tag{2.23}$$

In some rare-earth doped materials the spin-lattice interaction is very weak resulting in a relaxation time T_{sl} that is as long as a day.[2] From 2.23 we see that it is possible to let the time delay between pulse 2 and 3 be as long as days and still get a stimulated echo. For systems such as these, the stimulated echo also provides a method for measurement of the spin-lattice relaxation time. In addition, since t_{32} can be much longer than the dephasing time, the stimulated echo can also provide information about slow spectral diffusion. From all this, it may seem like the stimulated echo experiment is the experiment of choice over the two pulse photon echo, but the intensity of the stimulated echo is always much smaller than that of the two pulse echo. This can make detection a significant problem and the experiment much more difficult.

Application to Optical Memory Devices

Earlier in this chapter, the use of PSHB (in the frequency domain) for application in optical memory devices was discussed. Recall that the primary limitations imposed by working in the frequency domain were the need for an extremely stable laser (less than the homogeneous linewidth) to maximize storage density and the need to slowly readout the data. Such limitations can be alleviated by working in the time domain rather than the frequency domain. Time domain storage is accomplished by using stimulated photon echoes and is referred to as coherent time-domain optical memory (COTM)[2] or stimulated photon-echo memory.[75] The write process which stores the information is accomplished by the first two pulses of the stimulated echo sequence. In this application, the second pulse is broken into a series of shorter "bits" of data as shown in figure 2.7a. As in the previous section, the second pulse "stores" the information in the form of a population grating in the ground and excited states. Just as in frequency domain storage, a long lived reservoir like nuclear hyperfine levels must be available in order for the ground state population grating to remain for longer than the fluorescence lifetime. The third pulse in the stimulated echo sequence acts as the read pulse after which the data is reproduced as the stimulated photon echo.

The physical storage mechanism in COTM is identical to that of frequency domain PSHB. In the frequency domain, a pattern of holes were burned in the inhomogeneously broadened profile which were read as a series of 1's and 0's (see figure 2.4). The physical origin of the holes is the redistribution of the populations of the ground state hyperfine levels or in other words a ground state population grating. In the time domain the data pulse interferes with the coherence created by the write pulse storing the information in the form of a redistribution of the ground state population as a function of frequency. This population grating created by the pulse sequence is a pattern of holes burned in the inhomogeneously broadened profile that is the Fourier transform

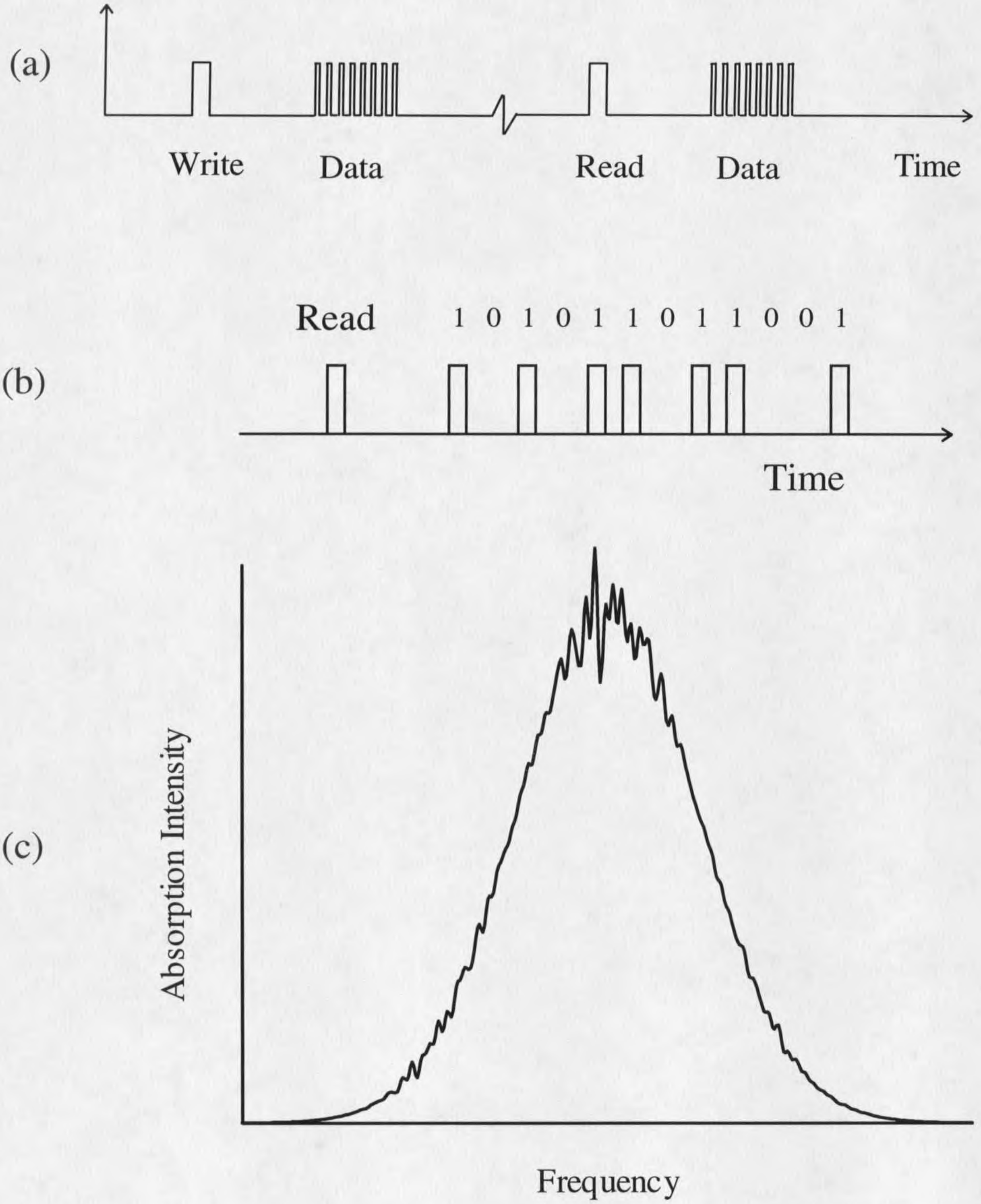

Figure 2.7 Schematic for coherent time-domain optical data storage. (a) shows the modified stimulated echo pulse sequence for storage and readout of the data. The interference of the data pulse with the read pulse shown in (b) results in the ground state population grating which can be seen in (c) as a pattern of holes burned in the inhomogeneous line. The hole pattern is the Fourier transform of the excitation pulse sequence.

of the pulse sequence. This can be seen by looking at the diagonal element of the density matrix representing the ground state population which is given by[6]

$$\rho_{11} = 1 - (\mu/2\hbar)^2\{|E_1(\omega)|^2 + |E_2(\omega)|^2 + 2\mathrm{Re}[|E_1^*(\omega)|^2\,|E_2(\omega)|^2]\}, \qquad (2.24)$$

where $E_i(\omega)$ is the Fourier transform of the ith pulse. The Fourier inverse relationship between stimulated echoes and holeburning has been demonstrated experimentally[76] and is shown schematically in figure 2.7b. Thus while CTOM is physically the same as PSHB, it places much less stringent requirements on the frequency stability of the laser. In addition it provides a method by which data can be stored at GHz rates in packets on the order of 100's of μs long.

Stimulated echoes can also be used in optical signal processing applications where they can perform convolutions and correlations of the three temporally modulated excitation pulses.[11] In any stimulated echo sequence, the echo amplitude represents the cross correlation of the first pulse's temporal waveform with the convolution of the second and third pulses' waveforms. Usually one of the three pulses is temporally short, such that its Fourier transform can be considered constant over the bandwidth of the other two pulses. In this case, the output is determined only by the temporal properties of the other two pulses; if the first pulse is short, the stimulated echo is the convolution of the second and third pulses, while if the second pulse is short the echo is the cross correlation of the first and third pulses. The use of stimulated echoes in this manner allows for the processing of amplitude-, phase-, and frequency-modulated signals with predicted data bandwidths exceeding 5 GHz.[11]

As for PSHB in the frequency domain, the ultimate limits on the performance of coherent transient signal processors or CTOM are determined by the fundamental material parameters Γ_{inh} and $\Gamma_h = 1/(\pi T_2)$. The limit on the length of the data pulse train is established by the homogeneous dephasing time T_2 since the stimulated echo amplitude decays as a function of the separation between the first and second laser pulses at this transverse relaxation rate (see equation 2.23). The inhomogeneous linewidth limits the rate at which the amplitude of the data pulse can be modulated, since the highest frequency component of the Fourier transform of this data pulse must be within the inhomogeneously broadened line.

In addition to these fundamental limits, there are many practical problems associated with implementation of coherent transients in such devices. A significant problem is the extra dephasing introduced by the storage process itself. This excitation-intensity-dependent process[22,36-44] involves both of the excitation (write and data) pulses in the echo sequence, which can cause abrupt random shifts in the transition frequency of the echo ions due to the optical excitation of neighboring ions. When these shifts are not present throughout the entire echo pulse sequence, they cause incomplete rephasing and effectively shorten the coherence time T_2. This reduces the length of the data pulse trains that can be stored or processed. A variety of interactions, which are material dependent, can cause this effect and are discussed in greater detail in chapter 4.

CHAPTER 3

EXPERIMENTAL TECHNIQUES AND APPARATUS

A variety of linear and non-linear spectroscopic techniques were employed in the characterization of the materials studied in this thesis. The techniques and experimental apparatus used will be presented in this chapter, while the actual data and details specific to a given material or experiment will be presented in the following chapters. In general, a material is initially studied using conventional spectroscopic techniques like absorption and fluorescence to determine the crystal field levels, inhomogeneous linewidths, and fluorescence lifetimes T_1. Variations on these general techniques such as time-resolved fluorescence and fluorescence-excitation experiments can provide additional information about the dynamics of energy transfer in the material as well as correlation of energy levels with crystallographic sites. These linear techniques usually have lower spectral resolution than nonlinear techniques. Higher resolution non-linear techniques like two pulse photon echoes, ODNMR, and PENDOR were used to measure homogeneous linewidths and nuclear hyperfine splittings of the ground and excited states. Stimulated photon echoes were also used to detect slow spectral diffusion. Table 3.1 summarizes

Table 3.1 Experimental techniques and their spectral resolutions. Where equipment is the liming factor, the resolution is for the equipment described in this chapter.

Experimental Technique	Spectral Resolution	Limiting Factor
White light absorption	3 Ghz ~ 0.1 cm^{-1}	SPEX 14018 Monochromator
Laser absorption	Mhz ~ 10^{-5} cm^{-1}	Laser jitter
Spectral holeburning	Mhz ~ 10^{-5} cm^{-1}	Laser jitter
ODNMR	KHz ~ 10^{-8} cm^{-1}	Inhomogeneous linewidth of nuclear levels (or RF source linewidth)
PENDOR	KHz ~ 10^{-8} cm^{-1}	Inhomogeneous linewidth of nuclear levels (or RF source linewidth)
Photon echoes	10's of Hz ~ 10^{-10} cm	Homogeneous linewidth

these experimental techniques, the associated spectral resolution for the equipment described below, and the factor which places the ultimate limit on the resolution.

All experiments were performed using a glass liquid helium cryostat with 3 windows providing transverse optical access to the sample. The crystals were immersed in the liquid helium which was pumped to 1.4 K.

Conventional Spectroscopy

Absorption

White light absorption experiments are typically performed to determine the crystal field levels of the rare earth doped material. The experimental setup for both white light and laser absorption is shown in figure 3.1. White light absorption spectra

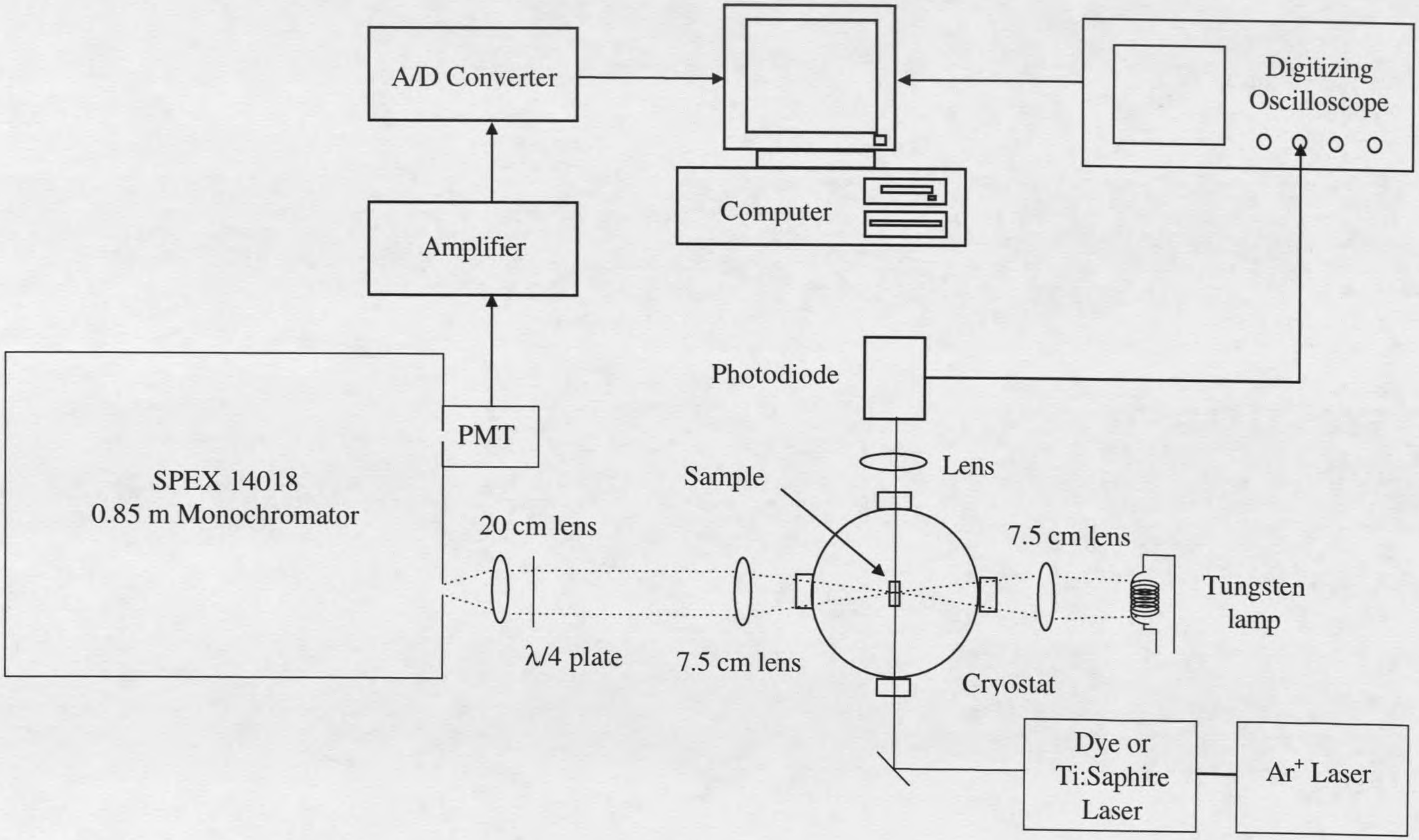

Figure 3.1 Experimental apparatus for white light absorption and laser absorption. The solid line indicates the beam path of the laser for laser absorption and the dashed line shows the light path for white light absorption. Arrows indicate electrical connections. The electronics connected to the monochromator are associated with the white light experiment and the electronics connected to the photodiode are for the laser absorption experiment.

were recorded using a 20 W tungsten halogen lamp as a light source. An image of the lamp filament was focused onto the crystal with a 7.5 cm lens, and the light transmitted through the crystal was collimated by a 7.5 cm f/2.8 camera lens. The collimated light was then focused by a 20 cm f/3.5 camera lens onto the entrance slit of a SPEX 14018 0.85-meter double monochromator (hereafter referred to as the SPEX). A quarter-wave plate was placed in front of the 20 cm lens to scramble the polarization of the light entering the monochromator. The SPEX uses two 1800 line/mm holographic gratings and has a maximum resolution of 0.1 cm^{-1}. The light passing through the exit slit of the monochromator was detected with an EMI model 9558QB photomultiplier tube (PMT). The signal from the PMT was amplified and filtered using a Tektronix 7A22 amplifier in a 7904 oscilloscope and then digitized by a 12 bit A/D converter.

The experiment was computer controlled by a DEC MicroVAX II or an 80486 PC. The MicroVAX was equipped with Data Translation DT2762 12 bit A/D converter, DT2766 12 bit D/A converter, and DT2769 real-time clock boards. The PC used a National Instruments AT-MIO-16F-5 multi-function board that had 12 bit D/A's, and A/D's and a 16 bit counter/timer. The data were acquired by stepping the SPEX and then measuring the transmitted light intensity. Signal averaging was accomplished by reading the A/D converter a very large number of times at each setting of the monochromator. The SPEX was calibrated with a uranium hollow cathode lamp.

Laser absorption experiments were also performed to obtain higher resolution measurement of the inhomogeneous profiles. Laser absorption provides a much higher resolution than white light absorption since its resolution is limited by the linewidth of the laser 1-2 MHz $\cong$ 3 x 10^{-5} cm^{-1} as compared to the 0.1 cm^{-1} of the monochromator. The Eu^{3+} $^7F_0 \rightarrow {}^5D_0$ and Pr^{3+} $^3H_4 \rightarrow {}^1D_2$ transitions are in the visible and were probed using a Coherent 599-21 single-longitudinal-mode cw dye laser pumped by a Spectra Physics Stabilite 2016 Argon laser. The dye laser has a jitter limited spectral linewidth of ~1-2 MHz and can be scanned 30 GHz continuously. The Tm^{3+} $^3H_6 \rightarrow {}^3H_4$ transition is in the near infrared and was probed with a Coherent 899-21 cw Ti:Saphire ring laser pumped by a Coherent Innova 400/20 Argon laser. To avoid spectral hole burning, which could alter the amount and shape of the absorption profile, a large beam diameter of ~1cm and very low laser powers of < 1 mW were used. The transmitted laser light was detected by an EG&G photodiode or Hamamatsu R928 PMT. As the laser was scanned 20 GHz, the signal from the detector was sampled by a Tektronix TDS620A digitizing oscilloscope that was triggered by the start of the laser scan, and data were transferred from the scope to a computer via the GPIB bus. The intensity of the laser was recorded with and without the crystal in the beam path as the laser was scanned. The absorption data obtained with the crystal in the beam were then ratioed by the “raw” laser intensity to remove variations due to changes in the laser intensity as a function of frequency.

Fluorescence

Fluorescence was excited using the Coherent 599-21 or 899-21 cw laser described above or a nitrogen-laser-pumped pulsed dye laser. The experimental setup for pulsed and cw excitation is shown in figure 3.2. The cw lasers were focused onto the sample using a 33 cm lens and the pulsed laser was focused with a 25 cm lens. When the laser was resonant with a transition, the sample fluoresced along the path of the laser beam. Fluorescence was collected at 90° relative to the laser beam. For cw excitation, data acquisition and the remainder of the setup was identical to the white light absorption experiment described in the previous section with the exception of a dove prism between the 7.5 cm and 20 cm lenses. The dove prism rotates the horizontal fluorescence streak to vertical so that more light is imaged onto the vertical entrance slit of the SPEX. Pulsed fluorescence experiments used the same optical setup as for cw fluorescence but required different electronic equipment for photon counting as shown in figure 3.2. For photon counting, the output of the PMT was passed through a preamplifier and discriminator then converted to TTL pulses. The pulses were counted by a GPIB controlled Fluke 1953A counter/timer, and the entire experiment was computer controlled.

Fluorescence lifetimes (T_1) were measured using the same optical setup shown in figure 3.2 for the cw laser, with the addition of two 80 MHz acousto-optic (A/O) modulators placed in the laser beam The A/O modulators were used in series to gate the cw laser, generating pulses of 1 μs duration. The fluorescence detected by the PMT was

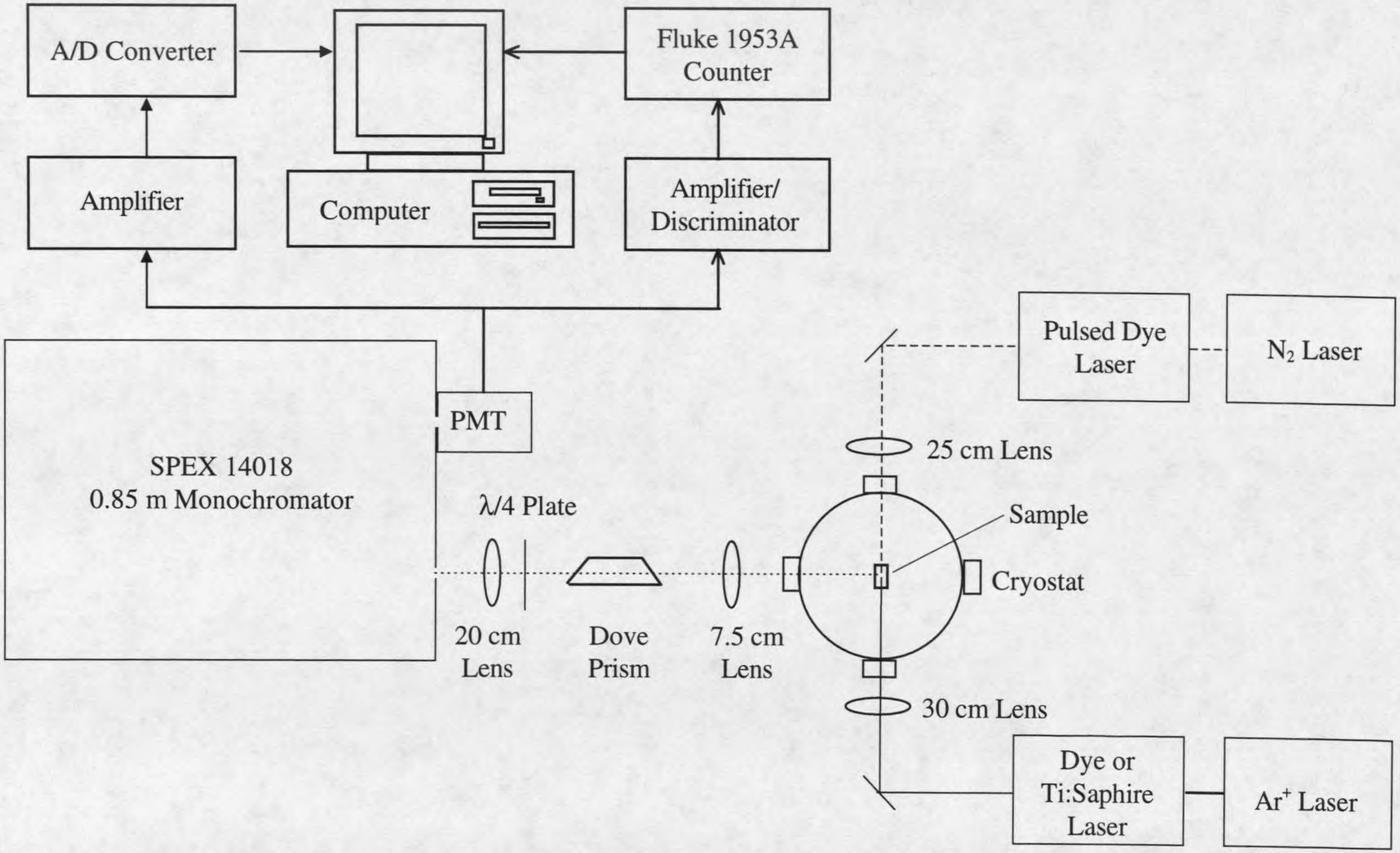

Figure 3.2 Experimental apparatus for cw and pulsed fluorescence measurements. The solid line indicates the beam path of the cw laser, the dashed line shows the beam path for the pulsed laser, and the dotted line show the path of the fluorescence. Solid arrows indicate electrical connections for the pulsed fluorescence experiments and open arrows are for cw fluorescence experiments.

averaged with a Tektronix TDS620A digitizing oscilloscope. In cases where wavelength selectivity was not required, the SPEX was not used and the PMT was placed at the window of the cryostat.

Fluorescence Excitation

In the previous section, experiments were described in which fluorescence spectra were obtained by fixing the laser excitation frequency and scanning the monochromator. Those types of experiments provide information about the lower lying multiplets to which the excited states fluoresce. At times, addition information is needed regarding the excited states that could not be determined by white light absorption. For example, some absorptions are simply too weak to be detected in a white light absorption experiment, but pumping the transition with a laser can result in easily detected fluorescence. Fluorescence-excitation experiments were performed by monitoring the fluorescence while scanning the excitation frequency of the laser, providing an alternative method for measuring the location, strength and width of absorbing transitions.

In addition to detecting weak absorptions, fluorescence excitation experiments also allow for site selective identification of absorbing transitions. In crystals where the rare earth ions can substitute into multiple crystallographic sites, absorptions will be observed for the same transition at various energies due to the differences in the local crystal field for the different sites. Crystal defects can also cause additional lines in the spectra. In these cases, fluorescence from a transition belonging to a given site is monitored (by using a monochromator to detect fluorescence from only that transition) while the laser is scanned over the various absorption peaks. When the laser is resonant with other transitions associated with the same site, fluorescence will be detected. It is important to note however, that spectra recorded using this technique can become quite complicated if there is energy transfer among the sites. In this case it may be difficult to assign transitions since pumping one site may cause fluorescence in another.

Site selective fluorescence excitation experiments were performed using the same experimental setup shown in figure 3.2. Spectra acquired using the pulsed dye laser were obtained by scanning the laser under computer control while monitoring the fluorescence from each crystallographic site. Experiments using the cw laser were performed by monitoring the fluorescence for a given site while tuning the laser by hand to the various absorption lines to determine the site to which they corresponded.

Nonlinear Spectroscopy

Photon Echoes

Two pulse photon echo experiments were performed to measure the homogeneous linewidths. All photon echo measurements were made with the single-frequency cw dye laser or Ti:Saphire laser and the apparatus shown in figure 3.3. The two-pulse excitation sequence was generated by gating the cw laser with two 80 MHz acousto-optic modulators in series before the sample. This resulted in an on/off ratio of

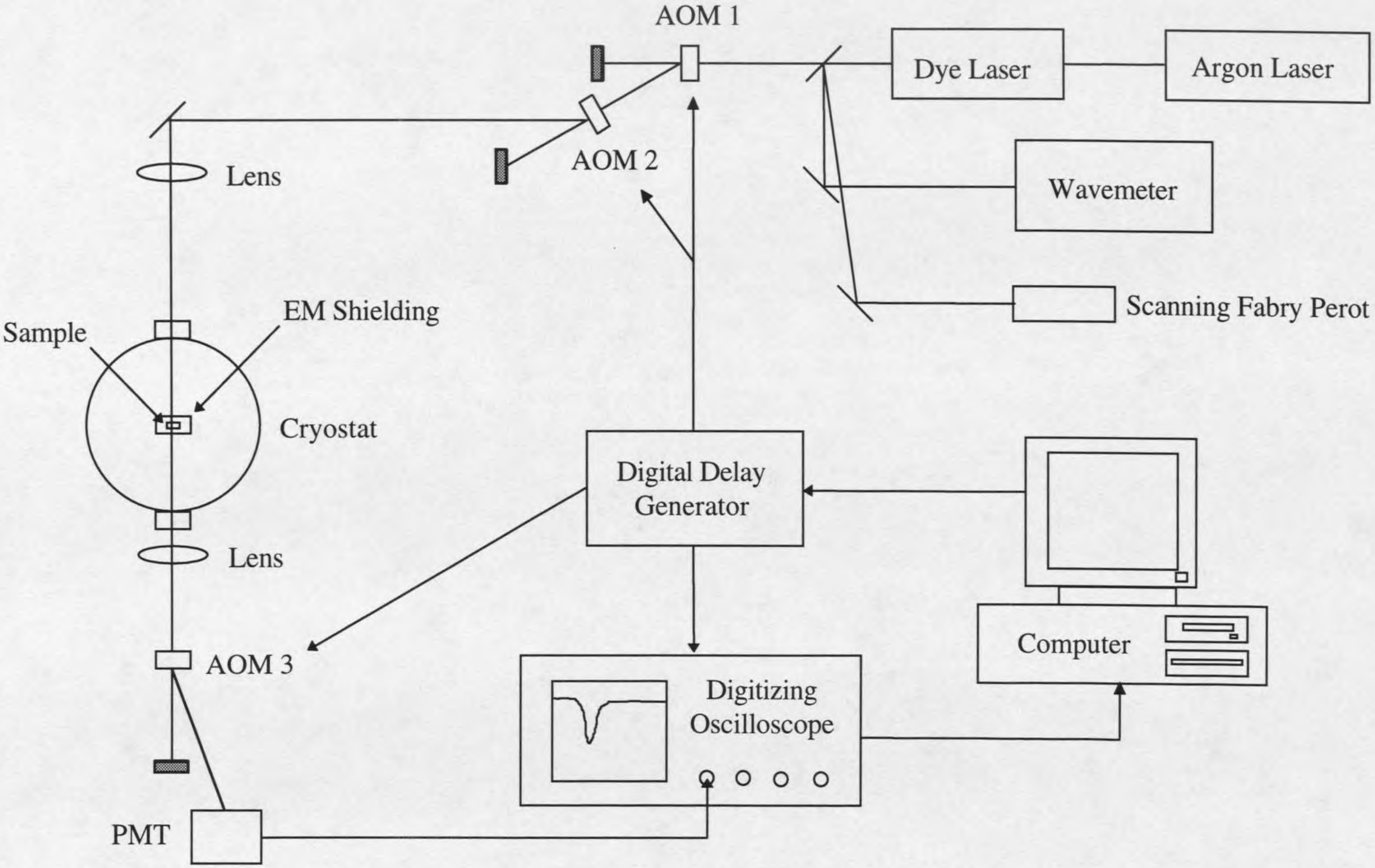

Figure 3.3 Experimental apparatus for two pulse and stimulated photon echoes. Lines show the path of the light and arrows indicate electronic connections. AOM 1, 2, and 3 are acousto-optic modulators and the EM shielding was a copper box surrounding the sample.

greater than 1000:1. Use of a single A/O modulator resulted in enough "leakage" of the laser between pulses to cause significant holeburning. The beam was focused using one of two different lenses to obtain a broad range of power densities. A lens of focal length f = 33 cm was used to obtain power densities of 5 - 50 W/cm^2, and focused the beam to a waist of radius w_0 = 30 µm. A longer focal-length lens of f = 1 m resulted in a beam waist of radius w_0 = 130 µm and was used to obtain power densities of 0.2 - 10 W/cm^2. The beam exiting the cryostat was then collimated with a 7.5 cm lens. A third A/O modulator was placed after the collimating lens to reject the transmitted excitation laser pulses, allowing collinear phase-matched detection of the echo with a fast Hamamatsu R928 PMT. The excitation pulse sequence timing was produced by a computer-controlled Stanford Research Systems DG535 digital delay generator. The photon echo signal from the PMT was averaged using a Tektronix TDS620A digitizing oscilloscope. The echo preparation pulses had a duration of 1 µs (unless otherwise noted) giving a laser bandwidth of ~ 2 MHz. The excitation power density was measured with an electrically calibrated Scientech model 362 thermopile power meter.

The output of the cw laser was monitored to verify single longitudinal mode operation using a Coherent model 240-2 optical spectrum analyzer with a free spectral range of 1.5 GHz driven by a home built ramp generator. The absolute frequency of the laser was measured to a resolution of 0.5 GHz with a home built wave-meter described prevously by Sun.[77]

An additional complication in the photon echo experiments on the Eu^{3+} and Pr^{3+} doped silicates was the ease with which holes were burned in the inhomogeneous profile. The 1 μs echo excitation pulses at a repetition rate of 7 Hz and laser powers of less than 0.2 mW were capable of bleaching the absorption within a few seconds to such a degree that the photon echo intensity had dropped by more than a factor of two. This creates addition problems since the absorption intensity is not a constant throughout the photon echo experiment. These reductions in absorption strength and therefore echo intensity can lead to nonexponential or anomalously short decays due to the holeburning rather than dephasing mechanisms. To avoid such spectral holeburning, the laser was repetitively scanned 300 MHz at intervals ranging from 250 ms to 2.5 seconds depending on the magnitude of time delays between excitation pulses used in a given experiment. It is important to note that while scanning the laser helps alleviate the complications of spectral holeburning one must be careful not to scan the laser too rapidly in order to maintain spectral overlap of the two excitation pulses at long delay times.

Photon Echo Nuclear Double Resonance (PENDOR)

PENDOR combines the use of optical coherent transients with the application of radio-frequency (RF) magnetic fields, and has been used in the measurement of hyperfine and superhyperfine structure.[78-80] This technique involves the detection of a reduction in the photon echo intensity when the applied RF field is resonant with a transition among the sublevels of the electronic transition. PENDOR was first used with the three pulse stimulated photon echo sequence[81] but has also been used with two pulse photon echoes.[79] When using two pulse photon echoes, there are at least two mechanisms which can cause the reduction in echo intensity. In the first, the RF removes population from the sublevel being pumped optically for the photon echo process to others which are not resonant with the laser. This results in a loss of coherence and therefore a reduction in the echo intensity by removing ions from the echo process. The second mechanism involves the generation of sidebands on the sublevels at the RF Rabi frequency.[79] These sidebands can be optically pumped resulting in echo modulation as discussed in the previous chapter, resulting in a reduction in the detected echo intensity.

The spectral resolution of the PENDOR technique is the same as for ODNMR and is limited by the inhomogeneous linewidth of the hyperfine transitions or the linewidth of the RF source rather than laser jitter. In fact PENDOR provides essentially the same information as that obtained by ODNMR, but has the advantage of being applicable to both ground and excited state resonances. However, it is often easier to obtain a better signal to noise ratio with ODNMR, and PENDOR requires a reasonably long coherence time T_2 in order for the RF to affect the echo intensity.

PENDOR measurements were performed on the Eu^{3+} and Pr^{3+} doped Y_2SiO_5 crystals using the photon echo apparatus described in the previous section with the addition of a radio-frequency (RF) magnetic field of ~ 1 G applied to the sample with a ten turn copper coil driven by a PTS 500 RF synthesizer and ENI model 411LA 10 watt RF amplifier. The amplified output of the RF synthesizer was sent to the coil by coax cables. After passing through the coil, the RF power was dumped into a 50 Ω dummy load. The photon echo intensity was monitored at a fixed excitation pulse time delay while the RF frequency was scanned under computer control. When the RF field was resonant with an excited state or ground state hyperfine splitting, a reduction in the photon echo intensity was recorded.

Optically Detected Nuclear Magnetic Resonance (ODNMR)

ODNMR involves the application of an RF field in combination with a holeburning experiment and was described in detail in the previous chapter. In short, if a hole is burned with a narrow band laser, the application of an RF field resonant with the hyperfine splittings results in a redistribution of populations among these levels that changes the degree of holeburning. For ground state resonances, this change in hole burning can be detected as an increase in fluorescence or decrease in the transmitted beam.

ODNMR experiments were performed using an experimental setup similar to that shown in figure 3.2 for cw fluorescence with the addition of the coil, synthesizer and amplifier described in the previous section. Changes in fluorescence rather than transmission were detected to obtain greater sensitivity. In these experiments, the fluorescence was not dispersed by the monochromator, rather a glass filter was placed in front of the PMT to reduce scattered laser light and the PMT was placed against the dewar window. The signal from the PMT was amplified by a Tektronix 7904 oscilloscope and read by an A/D converter in the computer. Data were acquired by setting the RF then reading the fluorescence intensity in a repetitive manner.

CHAPTER 4

SPECTROSCOPY AND DYNAMICS OF Eu^{3+}:Y_2SiO_5

The Y_2SiO_5 crystal shown in figure 4.1 is monoclinic and belongs to the C_{2h}^6 space group with eight molecules per unit cell. Triply ionized rare-earth ions substitute for the Y^{3+} ions and occupy two inequivalent crystallographic sites with no rotational point symmetry (C_1).[82] This host lattice was originally chosen by Yano *et al.*[23] as a good candidate for long dephasing times since the nuclear magnetic moments of the ligands are either very small or of low isotopic abundance. The nuclear magnetic moments of the constituent elements of Y_2SiO_5 are given as -1.89 μ_N for 0.04% abundant ^{17}O, -0.56 μ_N for 4.7% abundant ^{29}Si, and -0.14 μ_N for 100% abundant ^{89}Y.

Spectroscopy

The spectroscopy of Eu^{3+} in Y_2SiO_5 has been previously reported by Yano *et al.*[7,23,83] All of the energy levels for the $^7F_0$, $^7F_1$, $^5D_0$ $^5D_1$ and $^5D_2$ manifolds for each crystallographic site were identified using fluorescence, fluorescence excitation and absorption spectroscopy.[7,23,83] Since the crystal is of such low symmetry, all of the 2J+1-fold degeneracy of the free ion has been lifted and transitions from the ground state to all

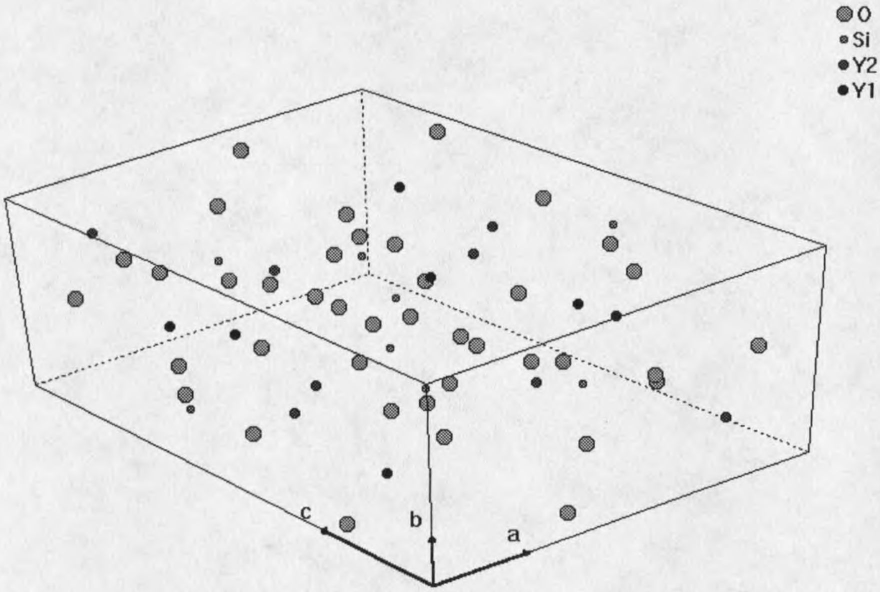

Figure 4.1 The monoclinic Y_2SiO_5 crystal structure. Y1 and Y2 indicate the two crystallographic sites with C_1 point symmetry occupied by yttrium. There are eight molecules per unit cell, and the lattice parameters are: a = 10.410 Å, b = 6.721 Å, c = 12.490 Å, $\beta = 102^\circ 39'$.

of the excited state levels are allowed. Figure 4.2 summarizes the energy level structure for Eu^{3+}:Y_2SiO_5.

The hyperfine splittings for the $^7F_0$ ground state were also measured[7] for the two isotopes of Eu using ODNMR and are summarized in Table 4.1. The $^5D_0$ excited state hyperfine splittings were determined using spectral hole burning and were reported in an earlier work of Yano *et al.*[23] that is summarized in table 4.2.

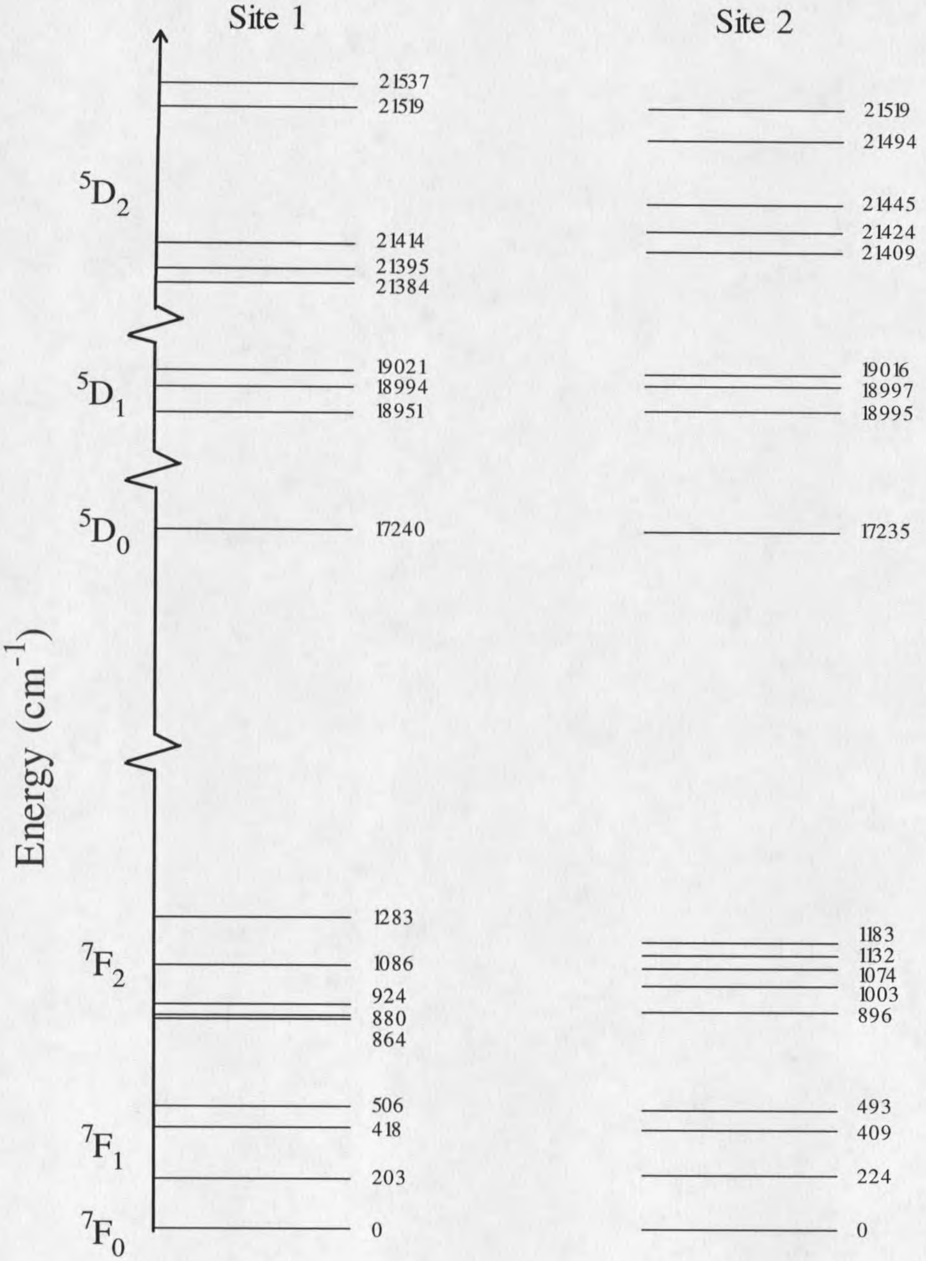

Figure 4.2 Energy level diagram for several of the ^7F_J ground state multiplets and ^5D_J excited state multiplets of Eu^{3+} in Y_2SiO_5 for the two crystallographic sites as measured by Yano *et al.*[7,23] Energy units are cm^{-1}.

TABLE 4.1. Hyperfine levels and spin Hamiltonian parameters for the $^7F_0$ ground state of Eu^{3+} in Y_2SiO_5 as measured by Yano *et al.*[7] using ODNMR (in Mhz).

	Site 1		Site 2	
	^{151}Eu	^{153}Eu	^{151}Eu	^{153}Eu
δ_1	34.5	90.0	29.5	76.4
δ_2	46.2	119.2	57.3	148.1
$\|D\|$	12.4	32.0	14.4	37.2
η	0.661	0.674	0.152	0.157

TABLE 4.2. Hyperfine levels and spin Hamiltonian parameters for the $^5D_0$ excited state of Eu^{3+} in Y_2SiO_5 as measured by Yano *et al.*[23] using hole burning (in Mhz).

	Site 1		Site 2	
	^{151}Eu	^{153}Eu	^{151}Eu	^{153}Eu
δ_1	75	194	63	160
δ_2	102	260	108	274
$\|D\|$	27.3	69.7	27.7	70.4
η	0.644	0.660	0.368	0.369

The sample used in these studies was a commercially produced unoriented crystal with dimensions 5 mm x 5 mm x 10 mm. The crystal was colorless and contained nominally 0.1% Eu. The Eu^{3+} ions substitute for Y^{3+} ions and absorb at 579.879 nm (site 1) and 580.049 nm (site 2). High resolution laser absorption spectra for the $^7F_0 \rightarrow {}^5D_0$ transition are shown in figure 4.3 for each site. Spectra were measured as described in the previous chapter by monitoring the transmitted laser intensity while scanning the cw dye laser over 20 GHz. The inhomogeneous linewidths were 4.1 GHz (site 1) and 3.8 GHz (site 2) FWHM. These are considerably narrower than the inhomogeneous linewidths of 8.6 GHz (Site 1) and 5.6 GHz (site 2) reported for the crystal used in the studies by Yano *et al.*[7,23] Our crystal had peak absorption coefficients of $\alpha = 0.5\ cm^{-1}$ (site 1) and $\alpha = 1.4\ cm^{-1}$ (site 2) in the direction studied, corresponding to oscillator strengths of 1.2×10^{-8} and 3.1×10^{-8}, respectively. A path length of 10 mm resulted in an absorption of 40% (site 1) and 76% (site 2).

Fluorescence lifetimes (T_1) were measured by exciting from the $^7F_0$ ground state to the $^5D_0$ excited state using gated cw laser pulses of 1μs duration. Fluorescence from the $^5D_0 \rightarrow {}^7F_2$ was detected with the PMT at the window of the cryostat. A Corning 3-66 glass filter was used to block scattered laser light that would saturate the PMT. The $^7F_0$ lifetimes were $T_1 = 1.9 \pm 0.1$ ms (site 1) and $T_1 = 1.6 \pm 0.1$ ms (site 2).

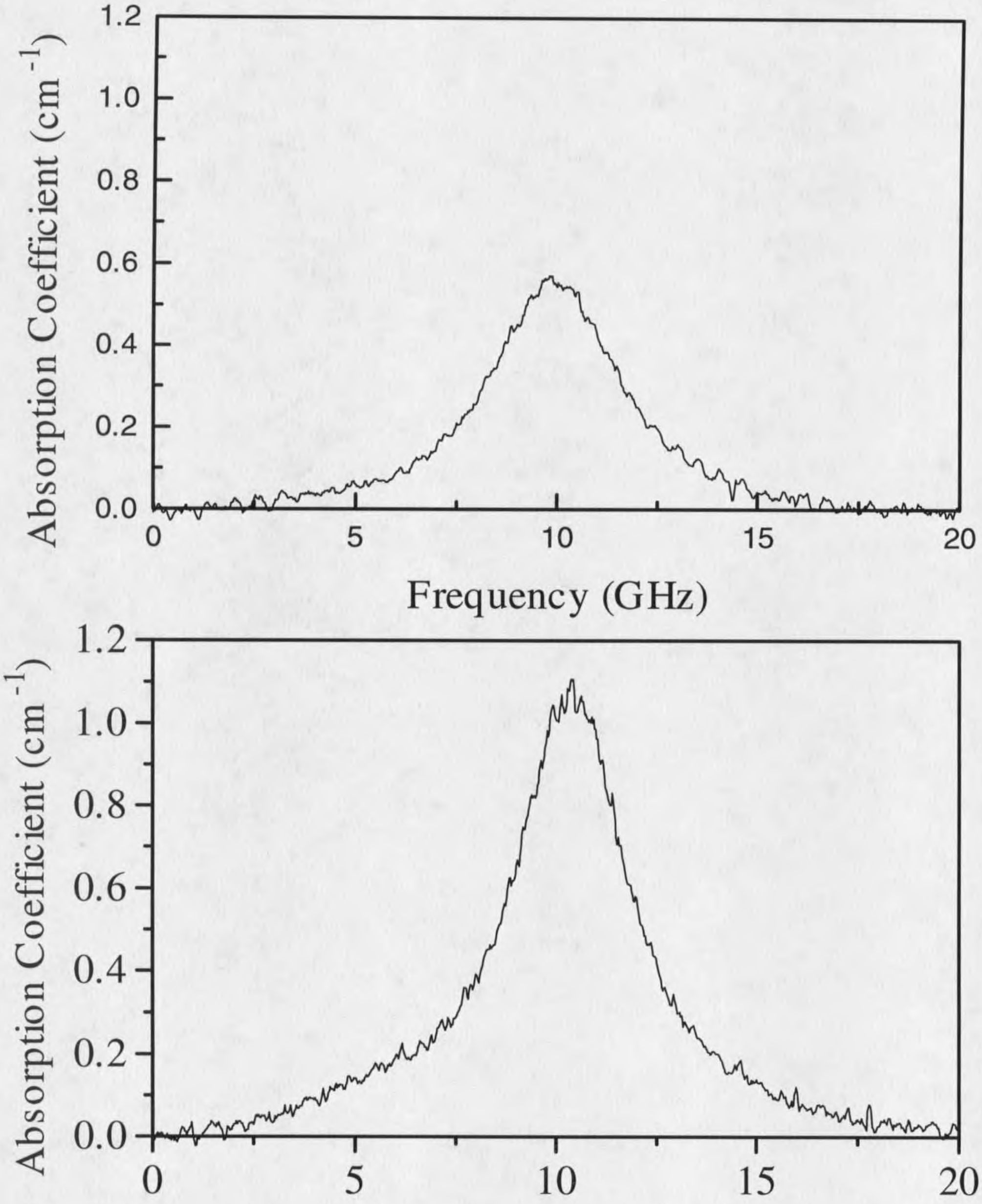

Figure 4.3 Absorption coefficients versus frequency for the $^7F_0 \rightarrow {}^5D_0$ transition of Eu^{3+}:Y_2SiO_5 for both crystallographic sites. Spectra were recorded by monitoring the transmission of a single frequency cw dye laser.

Dephasing Mechanisms in Real Crystals

Homogeneous broadening of optical transitions in rare earth doped crystals arises from dynamic perturbations on the transition frequency. The homogeneous linewidth Γ_h can be written as a sum of contributions from several mechanisms:

$$\Gamma_h = \Gamma_{pop} + \Gamma_{ion\text{-}spin} + \Gamma_{ion\text{-}ion} + \Gamma_{phonon}\ , \tag{4.1}$$

where Γ_{pop} is the contribution from the excited state population lifetime T_1, $\Gamma_{ion\text{-}spin}$ is the contribution due to nuclear and electronic spin fluctuations of the host lattice, $\Gamma_{ion\text{-}ion}$ is the contribution from changes in the local environment due to the optical excitation or population relaxation of other ions (so-called instantaneous spectral diffusion), and Γ_{phonon} includes pure dephasing contributions from temperature-dependent phonon scattering. Room temperature homogeneous linewidths for rare earth doped systems are typically dominated by Γ_{phonon}, but at low temperatures as is the case in all the experiments presented in this work, phonon scattering is frozen out so the Γ_{phonon} term in equation 4.1 is negligible.

The first term Γ_{pop} contains contributions from radiative and non-radiative decay of the excited state population, and establishes the ultimate limit on Γ_h. For the lowest component of multiplets below which there is a very large energy gap, the contribution to Γ_{pop} from spontaneous phonon emission is typically very small, leaving radiative decay as the dominant contribution. This is equivalent to noting that the fluorescence lifetime

T_1 for such metastable levels is dominated by radiative decay. The limit on the homogeneous linewidth or the so called "T_1 limit" is calculated using $\Gamma_{pop} = 1/(2\pi T_1)$.

Nuclear and Electronic Spins

The contribution from the second term $\Gamma_{\text{ion-spin}}$ is strongly dependent on the magnetic properties of the host lattice and can vary by more than an order of magnitude from material to material.[18,21-29] To minimize the $\Gamma_{\text{ion-spin}}$ contribution, it is important to choose an active ion with low sensitivity to field perturbations and to minimize the nuclear spins of the host lattice. Indeed, Y_2SiO_5 studied here was chosen by Yano *et al.*[23] to minimize the ion-spin contribution by reducing the nuclear magnetic moments of the ligands to zero (^{16}O), to very small values (^{89}Y) or to low isotopic abundance (^{29}Si and ^{17}O) as discussed earlier. Rare earth ions with an even number of 4f electrons are typically chosen as dopants, since in crystal sites of less than axial symmetry the electronic degeneracy is removed quenching the electronic magnetic moment. Thus traditional choices for dopant ions with low field sensitivity have been Eu^{3+}, Pr^{3+} and Sm^{2+} with a number of groups currently exploring Tm^{3+}. These ions do however, have an enhanced nuclear magnetic moment[84,85] resulting from a second order nuclear Zeeman interaction that is sensitive to the proximity of nearby electronic levels. The enhanced nuclear gyromagnetic ratio for a level $|0\rangle$ is given by[20]

$$\gamma_\alpha = \gamma_N + \frac{2 g_J \mu_B A_J \Lambda_{\alpha\alpha}}{\hbar}, \tag{4.2}$$

where

$$\Lambda_{\alpha\beta} = \sum_{n=1}^{2J+1} \frac{\langle 0|J_{\alpha}|n\rangle\langle n|J_{\beta}|0\rangle}{E_n - E_0} \tag{4.3}$$

and the sum is over the other crystal field levels in the J-manifold of the $|0\rangle$ level. This effect can be quite large for some ions. In particular, Tb^{3+} and Ho^{3+} are also even electron ions, but often have very large enhanced nuclear moments nearing that of an electron spin due to the presence of a crystal field component only a few cm^{-1} from the ground state. In addition to increasing the sensitivity of the ion to host-lattice spin fluctuations, this enhanced moment can cause a "frozen core" of host-lattice nuclear spins in the vicinity of the active rare earth ion.[68-74] The concept is that host lattice nuclei nearest the rare earth ion experiences a local field from the large enhanced moment that shifts these nuclei out of resonance with the bulk spins. These frozen spins are then unable to undergo resonant mutual spin flip-flop processes resulting in a distribution of flip rates that become faster with increased distance from the core, eventually reaching the bulk value. Such frozen cores give rise to non-exponential photon echo decays and make characterization of a pure dephasing time difficult. However, with the proper choice of lattice and dopant ion the ion-spin interactions can be minimized, and at extremely low excitation intensities, it is in principle possible to reach the limit of the homogeneous linewidth established by population decay.

Instantaneous Spectral Diffusion

The third term in equation 4.1, $\Gamma_{\text{ion-ion}}$, has recently been shown[7,22,29,36-44] to make important contributions to any measured value of the linewidth since the measurement process itself introduces this additional broadening. In an ideal photon echo experiment, as described in chapter 2, an ensemble of isolated two-level ions is “rephased” by the classic two-pulse excitation sequence, removing deterministic inhomogeneous dephasing effects and allowing accurate measurement of the dephasing time T_2. In photon echo experiments on real crystals, however, the excitation laser pulses cause abrupt and random shifts in the transition frequency of the echo ions due to perturbations arising from optical excitation of other rare earth ions. This effect is important even at low ion concentrations and low excitation densities such as that used here. When these random “static” frequency shifts are not present throughout the entire echo pulse sequence, they cause rephasing to be incomplete, and therefore they decrease the echo intensity.

Both the first and second laser pulses can contribute additional broadening to the measured linewidth. The effect of the second pulse can be understood by considering the evolution of the phases of ions participating in the echo sequence as shown in figure 4.4. The ions dephase in the first half of the echo sequence according to their detuning from the laser frequency. The second laser pulse can then excite other ions in the vicinity of some of the echo ions, abruptly changing their local fields and therefore their transition frequencies. This causes the affected ions to rephase at a different rate in the second half of the sequence as compared to the first half, resulting in incomplete

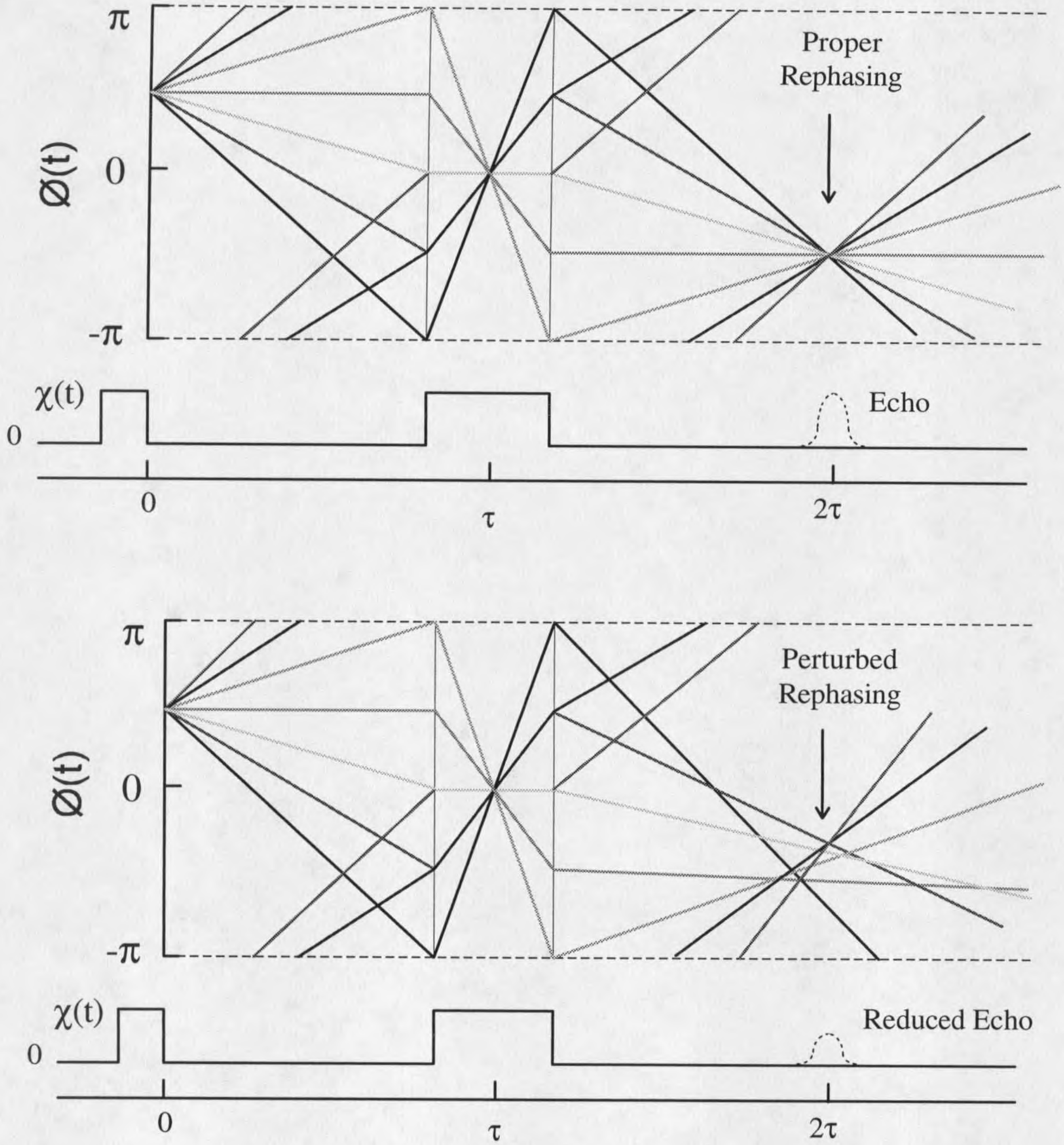

Figure 4.4 The effect of instantaneous spectral diffusion on the evolution of the phases of ions participating in the echo sequence. The upper picture shows the evolution of the phases in a ideal two level echo sequence.[51] The lower picture shows the effect of the second laser pulse in real echo experiments on the rephasing process.[86] The abrupt shift in the transition frequency of some of the ions due to excitation of other ions by the second pulse causes incomplete rephasing of the ensemble resulting in reduced echo amplitude.

rephasing. The resulting echo intensity is thus reduced yielding a shorter dephasing time or broader homogeneous linewidth. The effect of the first pulse is similar except that shifts in the ion's transition frequencies result from changes in the local fields due to the decay of neighboring ions. This process occurs at a rate determined by the excited state lifetime T_1, and for systems were $T_2 << T_1$ no population decay occurs on the time scale of the echo sequence and the first pulse intensity has no effect on the measured homogeneous linewidth.

Since the laser pulses are short compared to $T_2 = 1/(\pi\Gamma_h)$, these laser-induced inhomogeneous frequency shifts are often called instantaneous spectral diffusion. This effect has been studied for various rare-earth-doped materials and can contribute to the homogeneous linewidth through a variety of interaction mechanisms.[36-44] For ions in singlet states, as is the case for the ions studied here, electrostatic coupling is apparently the most important mechanism for the shifts. The magnitude of the instantaneous diffusion contribution to the linewidth is proportional to the number of excited ions and is therefore directly proportional to the excitation intensity. As a result, the homogeneous linewidth versus excitation intensity must be determined for each material and each set of experimental conditions (for example, each magnetic field) to allow extrapolation to the true zero-intensity homogeneous linewidth to be made. For a given sample, one can minimize the $\Gamma_{\text{ion-ion}}$ contribution by decreasing the sample excitation density (excitation laser intensity), but in doing so, the echo intensity is also reduced. In the present study, our low power measurements (small-pulse-area limit) approached the zero-intensity homogeneous linewidth limit quite closely.

Photon Echo Measurements

The contributions to the homogeneous linewidth described above have been investigated using two-pulse photon echo measurements. Echoes were excited using the cw dye laser and the experimental apparatus described in the previous chapter. The beam was focused with a lens of focal length 33 cm to a beam waist of 30 μm radius (or f = 1 m for the lowest point in power density). The excitation power density was varied between 5 and 50 W/cm^2, and the length of the two echo preparation pulses was 1 μs giving a laser bandwidth of ~2 MHz. The pulse areas were significantly less than the $\pi/2$ and π values that are optimal for echo intensity, but this prevented or minimized instantaneous diffusion. Echo decays were obtained by adding 16 scans together, where each scan was recorded by averaging four echoes at each delay between the two excitation pulses. This resulted in a total of 64 shots averaged at each delay. It was necessary to use this scheme of averaging to minimize the accumulation of population gratings in the ground state hyperfine levels (ie. minimize holeburning). Despite the use of this scan pattern, accumulated echoes at the earliest one or two delay values caused a significant enhancement of the recorded echo intensity such that it was necessary to truncate these data points. The pulse sequences were computer controlled and delays between the two excitation pulses (t_{12}) were varied between 10 μs and 3.5 ms. Samples were placed in liquid helium pumped to 1.4 K. All measurements were made at the center of the inhomogeneous line and to avoid spectral hole burning, the laser was scanned over 300 MHz in 2.5 s intervals.

Electromagnetic Shielding

In order to obtain the longest echo decays, it was necessary to shield the sample from stray electromagnetic fields by enclosing the crystal in a copper box. It was initially thought that the earth's magnetic field or stray dc magnetic fields present in the lab were responsible for some very small Zeeman splittings of the nuclear hyperfine levels. These splittings could cause echo modulation on the time scale of T_2 making the echo decay appear shorter. Based on this, the sample was shielded using a lead box with holes in each end to allow for optical access to the sample. Lead is superconducting at liquid helium temperatures and would therefore exclude all external magnetic fields. However, because there were holes in the ends of the box, the possibility that flux was trapped due to the presence of magnetic fields during the cool down must be considered. If this occurs, the sample would still not be in a totally field free region. Use of the lead shielding did in fact lengthen the observed echo decays, but it did not allow the application of larger (~100 G) external fields necessary to explore changes in the dynamics of the ^{89}Y mutual spin fluctuations and their effects on dephasing.

Experiments were then performed using 0.010" thick OFHC copper as a shield. With no external magnetic field applied, the copper shielding gave essentially the same results as for lead. Since copper is not superconducting, it was clear that it was not shielding DC fields but AC fields. In an attempt to measure the effects of various AC fields on the echo decays, PENDOR measurements were performed at frequencies ranging from 1 Hz to 40 kHz using the apparatus described in the previous chapter with a Stanford Research Systems DS345 synthesized function generator as the source. A dramatic resonance was observed at 2 kHz as shown in figure 4.4. Measurements of stray fields in the lab were also made using a Wavetek/Rockland 5820A spectrum analyzer with a simple wire as an antenna. When the Spectra Physics 2016 argon laser was turned on, the signal strength at 2 kHz increased by ~20db. Fields of this frequency would not be effectively shielded by 0.010" thick copper at room temperature since the skin depth at 2 kHz is ~ 0.075". However, at liquid helium temperatures the resistivity of OFHC copper has been shown[87] to decrease by a factor of 1,780 relative to the room temperature value. Using a factor of 1000 for the decrease in resistivity at liquid helium temperatures, the skin depth of OFHC copper at 2 kHz is 0.002". Thus our 0.010" thick OFHC copper box surrounding the crystal would effectively shield the sample from stray fields at this and higher frequencies. It is important to note that nuclear magnetic resonances are usually in the radio frequency domain and this resonance at an audio frequency was unexpected. The physical mechanism responsible for the 2 kHz resonance is still not understood and further investigations of this phenomenon are planned.

Discussion

In the shielded configuration described above, the measured linewidths were limited by a combination of the population decay time and dephasing due to yttrium

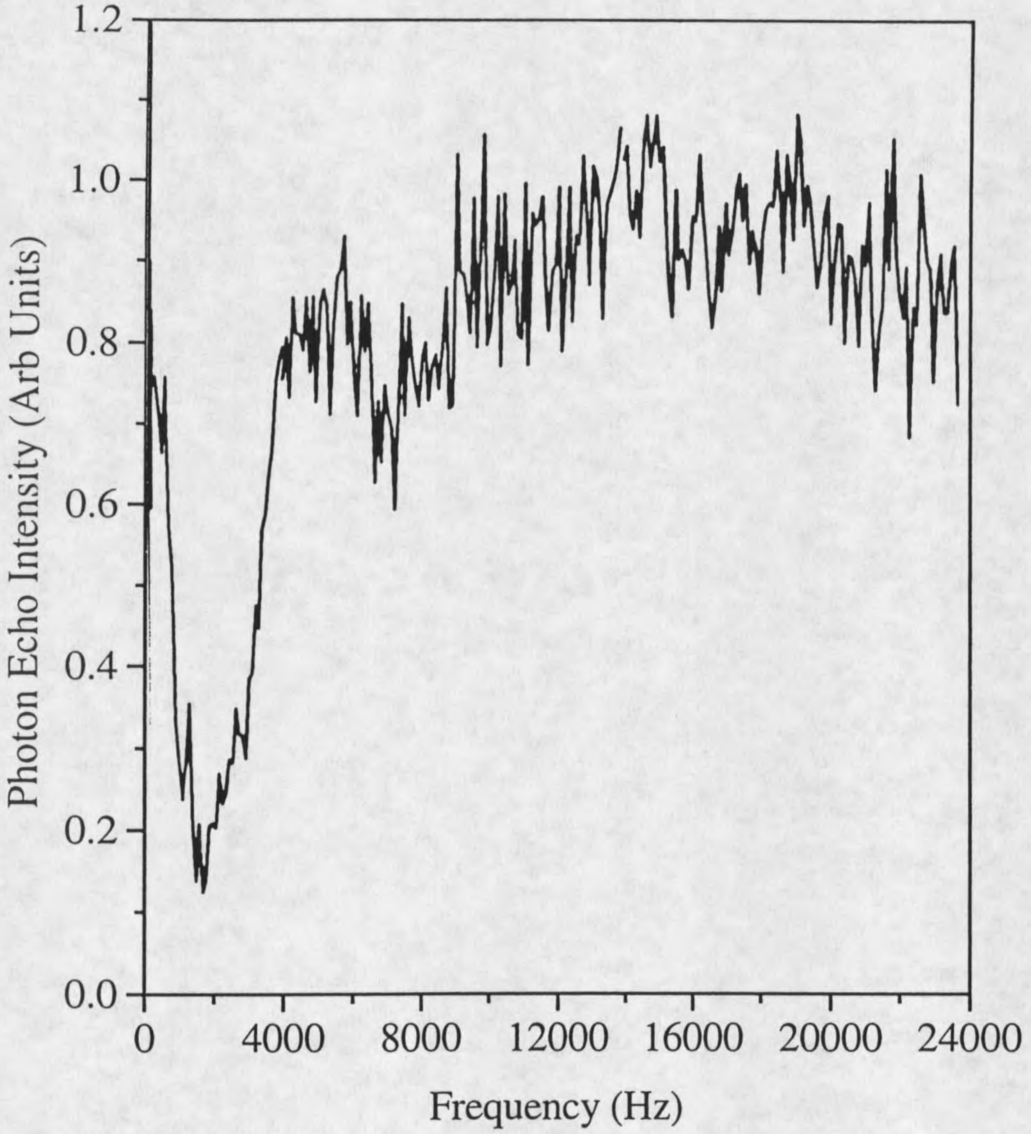

Figure 4.5 Kilohertz PENDOR measurements on the $^7F_0 \rightarrow {}^5D_0$ transition (site 1) of $Eu^{3+}:Y_2SiO_5$. The resonance at 2 kHz matches that of "noise" generated by the Argon laser power supply.

nuclear spin fluctuations. Table 4.3 summarizes the important spectroscopic and relaxation parameters for Eu^{3+} in the two sites of Y_2SiO_5. The fluorescence decay times of T_1 = 1.9 ms for site 1 and T_1 = 1.6 ms for site 2 contributes 85 and 100 Hz, respectively, to the homogeneous linewidths. Photon echo decays were recorded in zero field and in an applied magnetic field of 100 G, and a typical result is shown in figure 4.6. The decays as a function of excitation power density are shown in figure 4.7. The excitation power dependence is ascribed to instantaneous diffusion[22,36-44] due to the local multipole field or "crystal field" changes induced by the excitation of neighboring Eu^{3+} ions. In zero field the decays were exponential and corresponded to homogeneous linewidths of 210 Hz for site 1 and 290 Hz for site 2. We made the small correction for instantaneous diffusion using the results of figure 5.6, resulting in 195 Hz (site 1) and 230 Hz (site 2). These values are the sum of two contributions: that of population decay measured independently (above) and the contribution from ^{89}Y nuclear spin fluctuations obtained by subtraction to be 110 Hz (site 1) and 130 Hz (site 2). In $YAlO_3$ the dephasing of this transition is dominated by aluminum spins which have a magnetic moment 25 times larger than that of yttrium and contribute about 1 kHz to the linewidth.[25] A signature of nuclear spin-flip-induced dephasing is its sensitivity to external magnetic fields (H_0) since these modify the spin dynamics, slowing the nuclear mutual spin flips and narrowing the optical linewidth; in this case to 122 Hz (site 1) and 167 Hz (site 2) for H_0 =100 G. With the correction for instantaneous diffusion applied, this gives an extrapolated homogeneous linewidth of 105 Hz for both site 1 and site 2. Thus in a field of 100 G, the yttrium spin contribution to the homogeneous width of the

TABLE 4.3 Spectral and relaxation parameters for the $^7F_0 \rightarrow {}^5D_0$ transition of 0.1 % Eu^{3+} doped Y_2SiO_5.

	Site 1	Site 2
λ ($^7F_0 \rightarrow {}^5D_0$)	579.879 nm	580.049 nm
Γ_{inh}	4.1 GHz	3.8 GHz
T_1	1.9 msec	1.6 msec
Γ_{hom} (T_1)	85 Hz	100 Hz
$T_2^{meas\ a}$	2.6 msec (≡ 122 Hz)	1.9 msec (≡ 167 Hz)
$\Gamma_{hom}^{0\ b}$	105 Hz	105 Hz

[a] For H_0 = 100 G.

[b] Extrapolated to zero excitation intensity and for H_0 = 100 G.

Eu^{3+} transition drops to only 20 Hz for site 1 and 5 Hz (i.e., it is effectively zero) for site 2 in which case the T_1 limit is reached. This appears to be the first time that the contribution of the yttrium nucleus to optical line broadening has been obtained. In the past there have always been other, larger contributions masking it. The final measured and extrapolated linewidths are dominated by the T_1 contribution. Since the echo decays are exponential it appears that the yttrium spin fluctuation rate is rather homogeneous and "frozen core" effects seen in the echo decays of Pr^{3+} (Ref. [73]), Er^{3+} (Ref. [88]), and Cr^{3+} (Ref. [89]) are very weak here. This is consistent with the fact that the ground state of Eu^{3+} has a very small (quenched) magnetic moment of ~0.1-0.2 kHz/G[33].

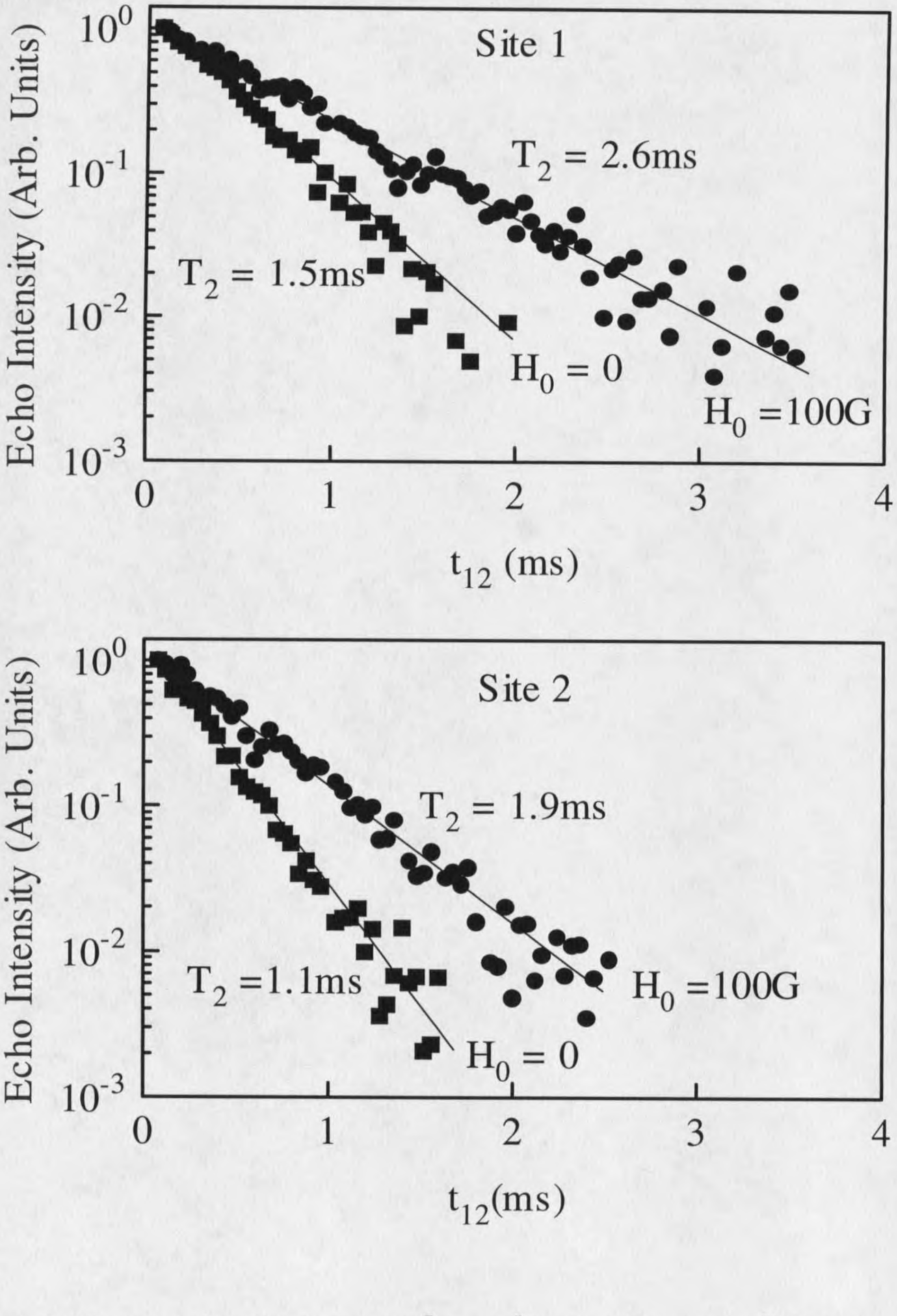

Figure 4.6 Photon echo decays on the $^7F_0 \rightarrow {}^5D_0$ transition of Eu^{3+}:Y_2SiO_5 at 1.4 K. The excitation density was 6 W/cm^2 and the straight lines are exponential fits to the decays yielding the dephasing times shown.

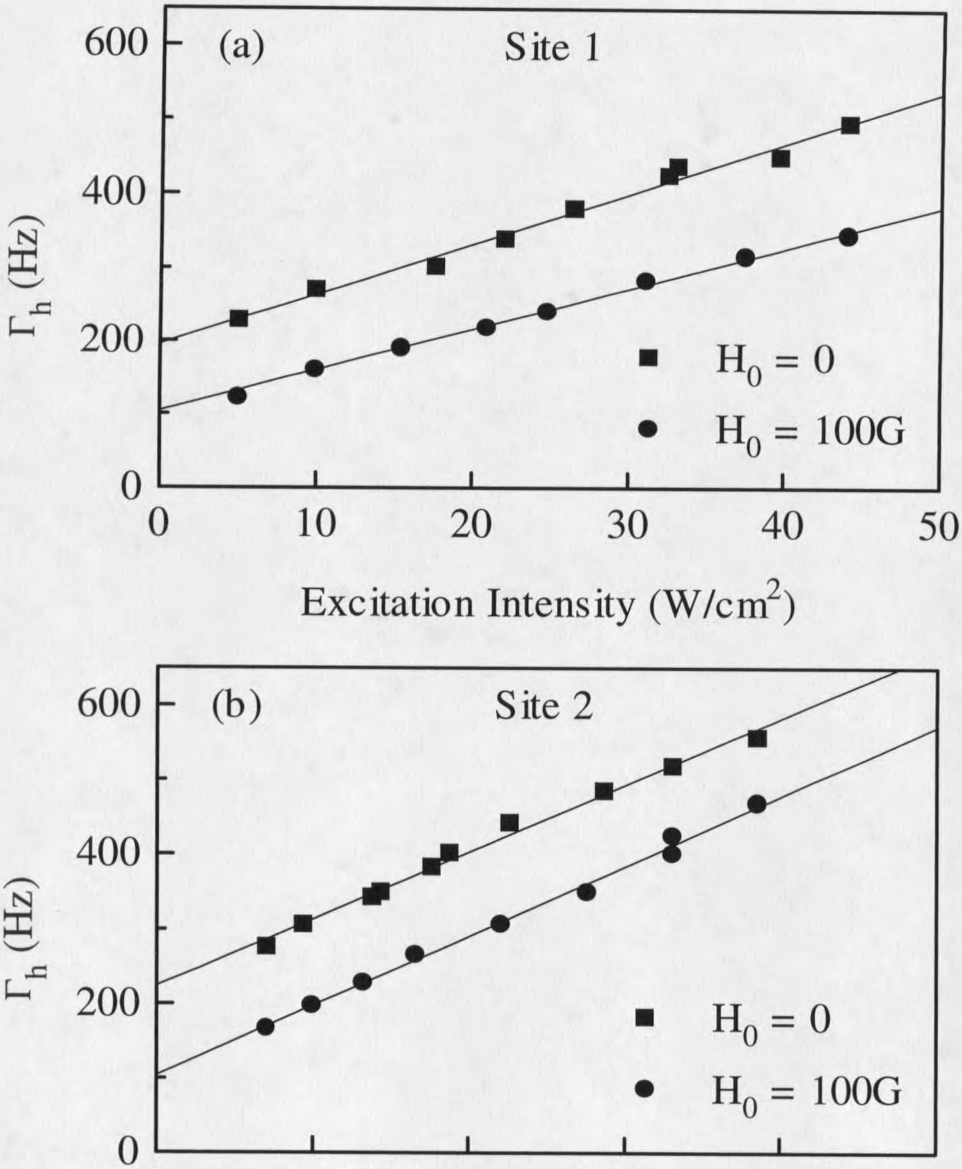

Figure 4.7 Dependence of the homogeneous linewidth on excitation power density (a) for site 1 and (b) for site 2, varying both echo preparation pulses simultaneously. This shows the contribution from instantaneous diffusion. The linewidths extrapolated to zero laser power for $H_0 = 100$ G are 105 Hz for both site 1 and site 2.

The contribution from instantaneous diffusion was also investigated by varying separately the power of the first and second pulses of the echo sequence. Figure 4.8 shows the dependence of the homogeneous linewidth on the individual pulse intensities. As found by Liu and Cone[40] and Huang *et al.*[22], increasing the second pulse intensity produced a stronger effect on the echo decay time. This is expected because the second pulse creates a local field during the rephasing half of the echo sequence that is different from that present in the first half. We observed, in addition, a noticeable shortening of the echo decay when varying the intensity of pulse 1. This was also observed in Y_2O_3:Eu^{3+} by Huang *et al.*[22] using an amplified first pulse. They attributed the effect to the decay of the excited state population during the echo sequence, and the same interpretation is given here. Kroll *et al.*[26,42] and Huang *et al.*[22] proposed a model predicting the effects of pulse 1 based on the excited state lifetime and the response of the system to pulse 2 effects. The magnitude of the pulse 1 effect observed here is consistent with the lifetime of $^5D_0$ and with the excess dephasing induced by population changes as measured from the pulse 2 power dependence as indicated by the theoretical fit in figure 4.6. This effect is particularly apparent for cases where T_2 is comparable with T_1 and is different from the usual manifestation of instantaneous diffusion, where excited ions do not decay appreciably during the echo pulse sequence such as in Tb:$YLiF_4$ where the lack of a pulse 1 dependence was very clearly shown[40]. We note that in $YAlO_3$:Pr^{3+} Bai and Kachru[43] observed a dependence of the dephasing on pulse 1 intensity and attributed it to dephasing induced by nonequilibrium phonons created during the relaxation of excited ions. This is not expected to be the mechanism in the

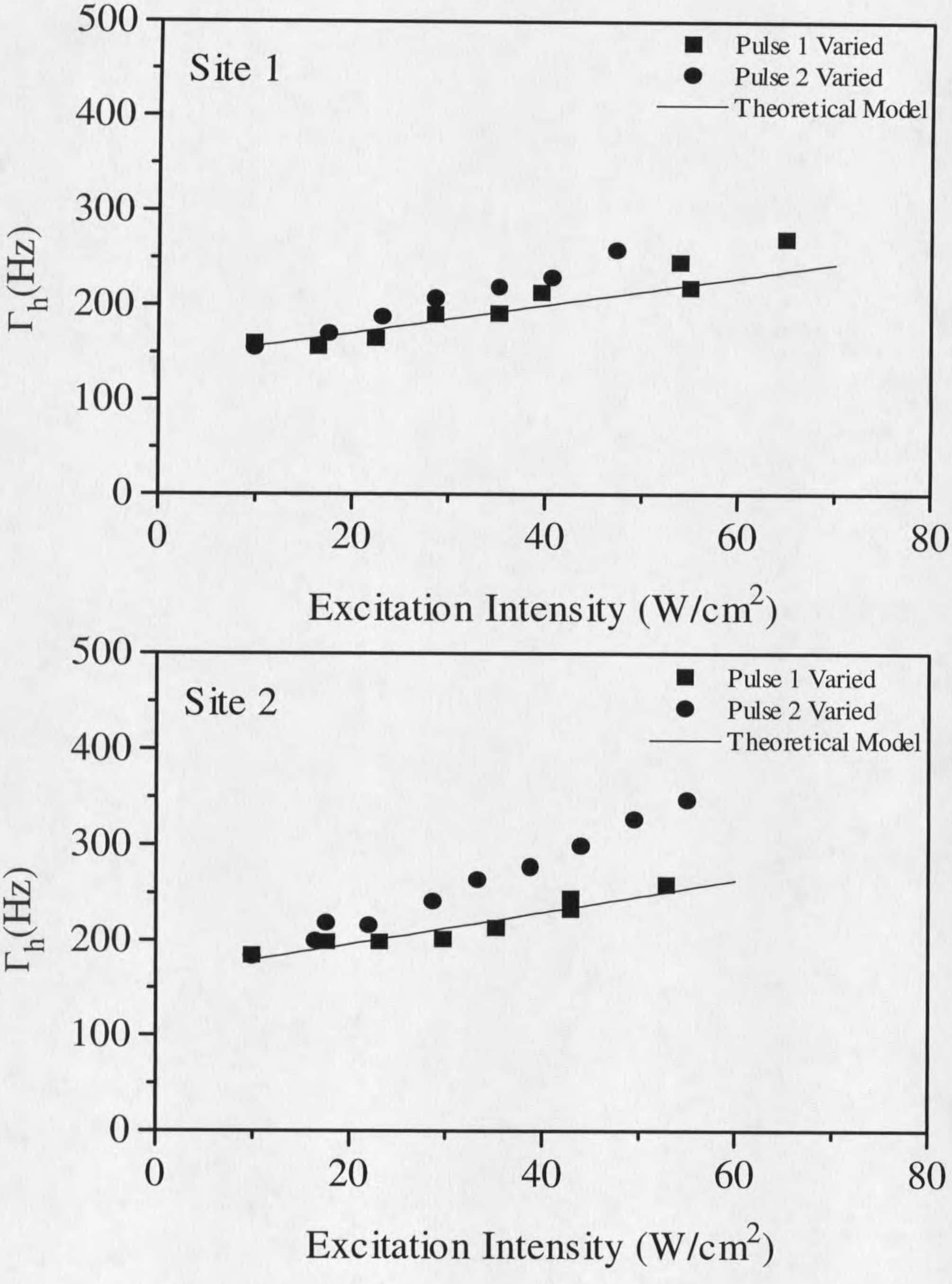

Figure 4.8 Dependence of the homogeneous linewidth on excitation power density for site 1 and site 2 measured by varying the intensity of the echo preparation pulses independently. Measurements for variations in the intensity of pulse 1 (2) were performed with pulse 2 (1) held constant at the lowest intensity used. The theoretical model is from Kroll *et al.*,[26,42] and Huang *et al.*[22]

present case because the lifetime of phonons created in the relaxation process will be very short.

CHAPTER 5

SPECTROSCOPY AND DYNAMICS OF Pr^{3+}:Y_2SiO_5

Our studies of Eu^{3+} doped Y_2SiO_5 presented in the previous chapter showed that this host was nearly ideal for achieving long optical dephasing times. For dopant ions, Pr^{3+} is perhaps not as good a candidate as the Eu^{3+} ion for magnetic insensitivity to host ion spins since it has a larger enhanced moment. However, Pr^{3+} is of interest since the lowest component of the $^1D_2$ manifold is a metastable level with a long fluorescence lifetime. In addition, the transition from the $^3H_4$ ground state to the $^1D_2$ excited state can have an oscillator strength that is an order of magnitude stronger than that of the Eu^{3+} $^7F_0 \rightarrow {}^5D_0$ transition. The Pr^{3+}:Y_2SiO_5 crystal used in these studies was commercially produced by the same source as the Eu^{3+}:Y_2SiO_5 sample and contained nominally 0.02% Pr^{3+}. The crystal was a colorless parallelepiped with dimensions 5 mm x 5 mm x 10 mm, and the two smaller faces were polished to glass like optical quality. It was determined by Laue X-ray diffraction that all crystal axes made oblique angles relative to the polished faces.

Spectroscopy

The $^3H_4$, $^1D_2$, $^3P_0$, and $^3P_1$ levels of Pr^{3+}:Y_2SiO_5 were studied via absorption, fluorescence, and fluorescence-excitation spectroscopy. Absorption and fluorescence spectra were recorded at a resolution of 0.5 cm^{-1} using the experimental apparatus described in chapter 3 and were calibrated with a uranium hollow cathode lamp. Fluorescence was excited using either the nitrogen-laser-pumped pulsed dye laser or the Coherent 599-21 single-mode cw dye laser. Site-selective fluorescence-excitation spectra were acquired using the pulsed dye laser scanned under computer control while monitoring the fluorescence from the lowest component of the $^1D_2$ manifold for each site. Fluorescence lifetimes (T_1) for each site were measured by exciting from the ground state $^3H_4(1)$ to the lowest energy component of the $^1D_2$ manifold, denoted $^1D_2(1)$, for each site with gated cw laser pulses of 1 μs duration. Emission to the $^3H_4$ and $^3H_5$ manifolds was detected with a photomultiplier tube and was averaged with a Tektronix TDS620A digitizing oscilloscope.

Spectroscopic measurements for $Pr^{3+}:Y_2SiO_5$ were first reported by Holliday *et al,*[90] who measured emission from the lowest component of the $^1D_2$ manifold to the $^3H_4$ and $^3H_5$ manifolds at a temperature of 20 K for both crystallographic sites. They also determined the ground state hyperfine levels using optically detected nuclear magnetic resonance (ODNMR), and the excited state quadrupole levels for site 1 only, using holeburning which has a lower resolution than PENDOR due to laser frequency jitter.

Our fluorescence and ODNMR measurements at 1.4 K gave ground state crystal field levels and hyperfine levels that are in good agreement with those of Holliday *et al.*[90] The site selective fluorescence spectra of figure 5.1 show identification of all nine components of the $^3H_4$ multiplet for each site; however, the peaks labeled (5) and (6) for

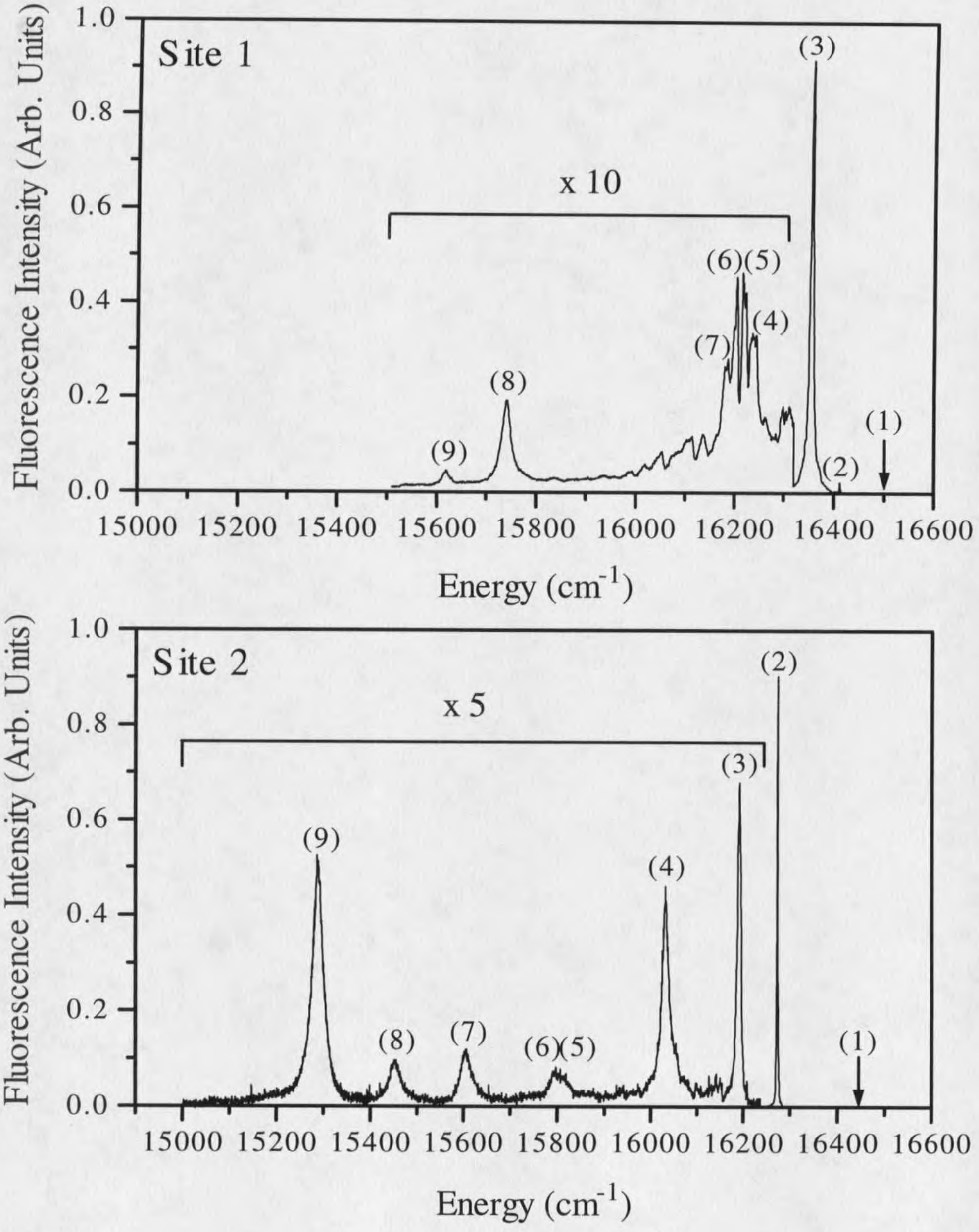

Figure 5.1 Fluorescence spectra showing emission from the $^1D_2(1)$ level to the $^3H_4$ manifold recorded by exciting the $^3H_4(1) \rightarrow {}^1D_2(1)$ transition for each crystallographic site of 0.02% Pr^{3+}:Y_2SiO_5. Emission from $^1D_2(1) \rightarrow {}^3H_4(1)$ is not shown since scatter from the laser saturated the PMT at that energy. Arrows indicate the location of the pump laser which was resonant with the $^3H_4(1) \rightarrow {}^1D_2(1)$ transition.

site 2 and (4) through (7) of site 1 are assigned with a lower degree of certainty than the remaining levels. In addition, we have performed absorption and site-selective excitation measurements on the $^1D_2$ multiplet and in the region of the ^3P_J and $^1I_6$ multiplets. The $^1D_2(1)$ hyperfine splittings have been measured for both sites with improved resolution.

Our absorption spectra for the $^1D_2$, $^3P_0$, $^3P_1$ and part of the $^1I_6$ manifolds are shown in figure 5.2. Assignment of the $^1D_2$ crystal field levels to the appropriate site was accomplished by recording a laser fluorescence-excitation spectrum while monitoring the fluorescence from the lowest $^1D_2$ component for each site. No evidence was found for energy transfer between sites.

High resolution laser absorption spectra for the zero phonon $^3H_4(1) \rightarrow {}^1D_2(1)$ transition for each site, shown in figure 5.3, were measured with the cw dye laser by monitoring the transmitted intensity while scanning the laser over 20 GHz. The inhomogeneous linewidths were 4.4 GHz (site 1) and 2.5 GHz (site 2) FWHM. It is worth noting that the inhomogeneous linewidths obtained for our sample are significantly narrower than the 30 GHz (Site 1) and 10 GHz (site 2) linewidths reported for the crystal used by Holliday *et al.*[90] Our crystal had peak absorption coefficients of $\alpha = 10$ cm^{-1} (site 1) and $\alpha = 1.3$ cm^{-1} (site 2) centered at 605.977 nm and 607.934 nm for site 1 and site 2 respectively. The corresponding oscillator strengths are 3×10^{-7} for site 1 and 2×10^{-8} for site 2 for the polarization and propagation direction used here. Sample lengths of 0.5 mm (site 1) and 10 mm (site 2) resulted in an absorption of 40% for site 1 and 73% for site 2.

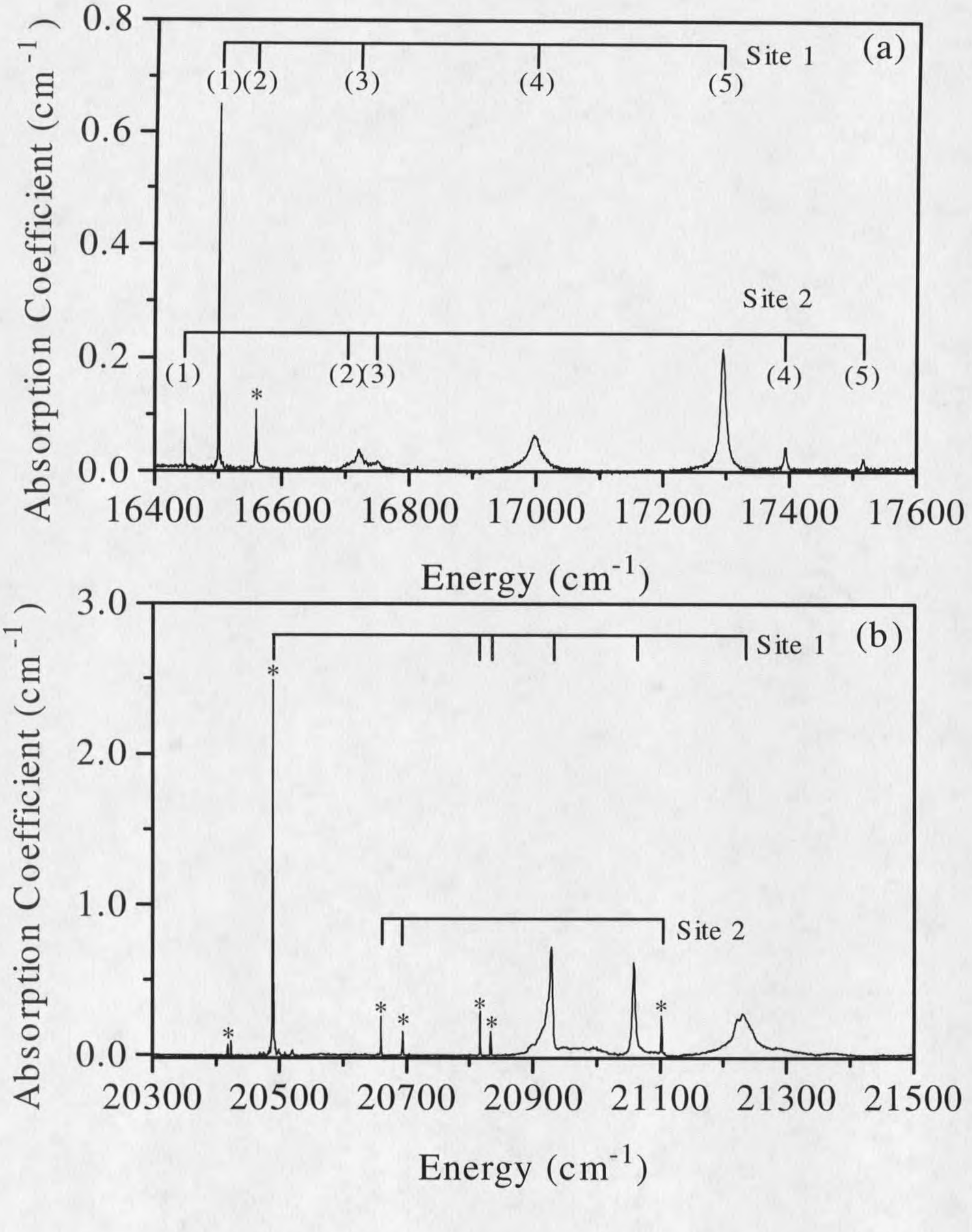

Figure 5.2 Absorption spectra showing (a) the $^1D_2$ multiplet, and (b) the ^3P_J and $^1I_6$ region for both sites of 0.02% Pr^{3+}:Y_2SiO_5. Energy and absorption coefficients are each displayed in cm^{-1} units. The widths of the lowest $^1D_2$ levels and others indicated by * were instrument limited, so the true peak absorption coefficients are proportionately reduced (see figure 5.3 for the actual values for the $^1D_2(1)$ transitions).

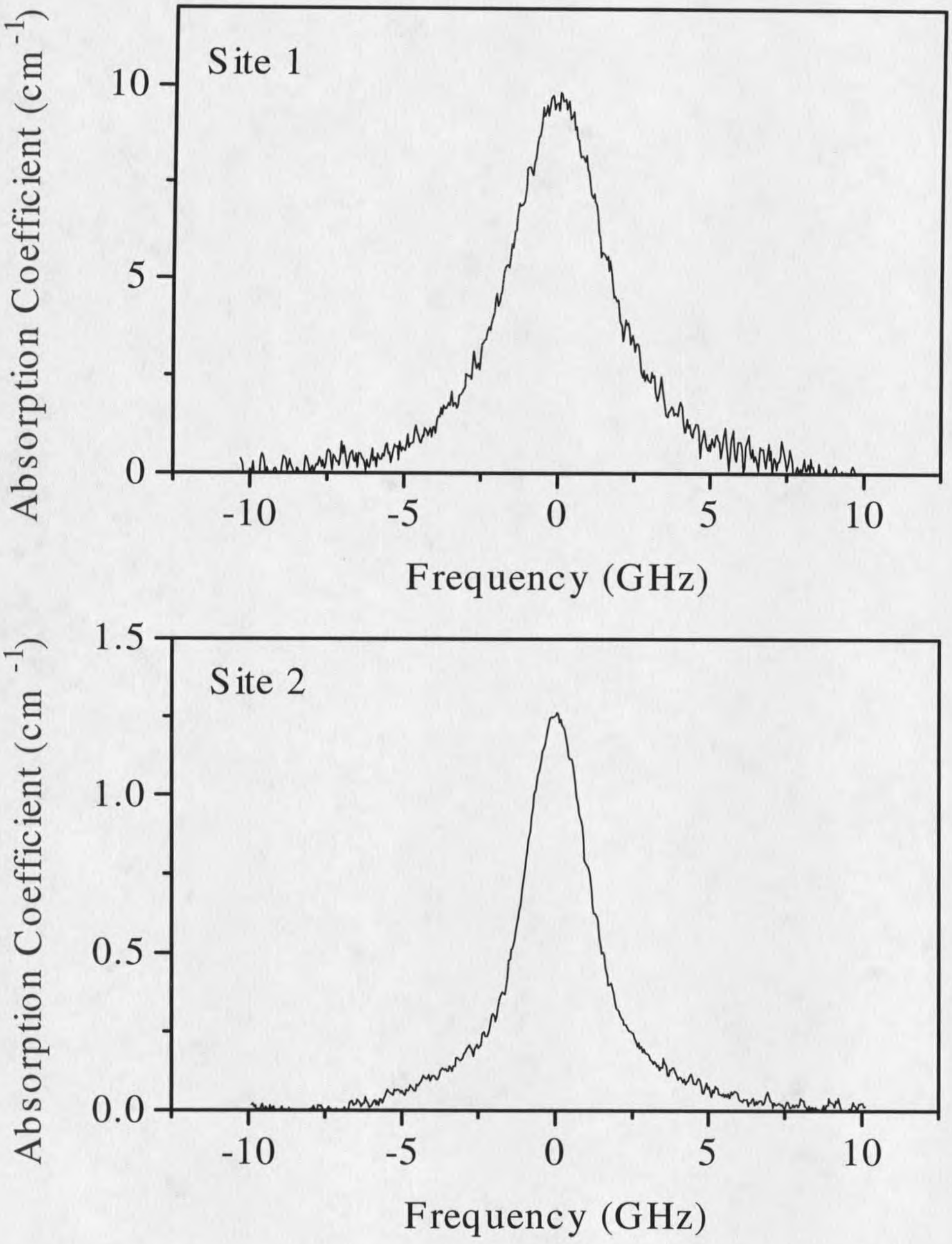

Figure 5.3 Absorption coefficients versus frequency for the Pr^{3+}:Y_2SiO_5 $^3H_4(1) \rightarrow {}^1D_2(1)$ transitions for sites 1 and 2 recorded by monitoring the transmission of a single frequency cw dye laser. Sample orientation is described in the text.

Fluorescence lifetimes were measured as described in the chapter 3. The $^1D_2(1)$ lifetimes were $T_1 = 164 \pm 5$ μs (site 1) and $T_1 = 222 \pm 5$ μs (site 2). These lifetimes are similar to those observed for other oxide hosts such as $YAlO_3$ ($T_1 = 180$ μs) and YAG ($T_1 = 230$ μs).

High resolution radio frequency measurements of the excited state hyperfine splittings were made using Photon Echo Nuclear Double Resonance (PENDOR). The photon echo intensity was monitored at a fixed excitation pulse time delay of 250 μs (site 2) and 100 μs (site 1), while the RF frequency was scanned. When the RF field was resonant with an excited state or ground state hyperfine splitting, a large reduction in the photon echo intensity was recorded. Excited state splittings of 4.595 MHz and 4.84 MHz were determined for site 1 from resonances observed experimentally at these frequencies and at the sum frequency, with widths of 30 kHz, 18 kHz and 7 kHz respectively. Resonances were observed only at 2.296 MHz and 4.592 Mhz for site 2 (both with widths of ~ 7 kHz), suggesting that the three excited state Kramer's doublets are equally spaced with separations of 2.296 Mhz. These more precise values for site 1 agree with those of Holliday *et al.*[90] to within their experimental error. Values for site 2 were not previously reported. Energy level diagrams summarizing the energies of the $^3H_4$ ground state multiplets and $^1D_2$ excited state multiplets are shown in figure 5.4.

The nuclear quadrupole interaction and second-order magnetic hyperfine or "pseudo-quadrupole" interaction can be combined[91,92] to give the effective quadrupole Hamiltonian

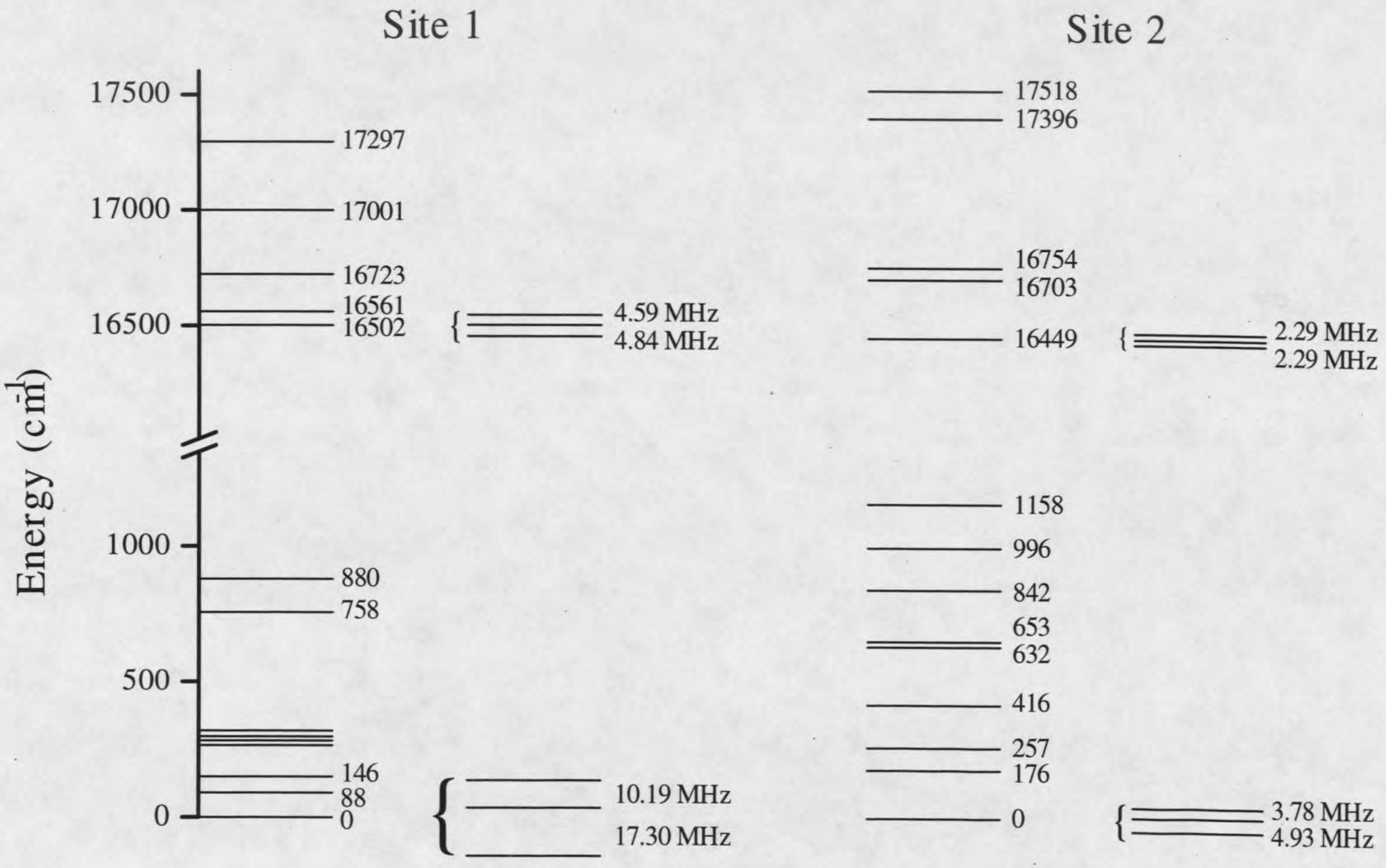

Figure 5.4 Energy levels for the $^3H_4$ ground state multiplets and $^1D_2$ excited state multiplets for the two crystallographic sites of Pr^{3+} in Y_2SiO_5 at 1.4 K. Energy units are cm^{-1}.

$$H_Q = D\,[I_z^2 - I(I+1)/3] + E(I_x^2 - I_y^2). \qquad (1)$$

The measured hyperfine splittings given above were used to calculate the combined quadrupole and second-order-hyperfine coupling constants D and E. Table 5.1 summarizes the observed hyperfine splittings and the fitted coupling parameters for the ground and excited states for both crystallographic sites. The signs of D and E are not specified since our experiments did not determine the ordering of the hyperfine levels.

Photon Echo Measurements

The primary goal of this work was the determination of the homogeneous linewidths of the $^3H_4(1) \rightarrow {}^1D_2(1)$ transitions for Pr^{3+} in the two sites and of the mechanisms responsible for those widths. Photon echo measurements of the homogeneous linewidths were made with a single-frequency cw dye laser and the apparatus described in chapter 3. The longer focal-length lens of f = 1 m was used in these experiments to focus the beam to a waist of radius $w_0 = 130$ μm, and the excitation power density was varied between ~ 0.4 and 20 W/cm^2. To avoid spectral holeburning, the laser was repetitively scanned 300 MHz in 250 msec intervals. Echo decays were recorded by averaging 64 echoes at each delay (t_{12}) between the extication laser pulses. It was not necessary to use the scanning technique described in the previous chapter since the ground state population grating did not form as easilly as for Eu^{3+}:Y_2SiO_5.

TABLE 5.1. Hyperfine levels and spin Hamiltonian parameters for the $^3H_4(1)$ to $^1D_2(1)$ transition for each site of Pr^{3+} in Y_2SiO_5 as measured by ODNMR and PENDOR (in Mhz).

	Site 1		Site 2	
	$^3H_4(1)$	$^1D_2(1)$	$^3H_4(1)$	$^1D_2(1)$
δ_1	10.19	4.59	3.78	2.29
δ_2	17.3	4.84	4.93	2.29
$\delta_1 + \delta_2$	27.5	9.43	8.71	4.58
$\lvert D \rvert$	4.44	1.36	1.32	0.651
$\lvert E \rvert$	0.564	0.425	0.305	0.217

Photon echo measurements for site 2 (607.76 nm) were performed using an optical path length of 10 mm along a direction that was determined by X-ray diffraction to be at an angle of 20° to the [010] axis. Measurements for site 1 (605.81 nm) were performed in a direction perpendicular to that used for site 2 on a sample of thickness 0.5 mm. All experiments were performed with the crystals immersed in liquid helium that was pumped to 1.4 K. All measurements were made at the center of the inhomogeneous line and with the sample shielded from stray electromagnetic fields by a copper box. Table 5.2 summarizes the important spectroscopic and relaxation parameters for Pr^{3+} in Y_2SiO_5.

TABLE 5.2. Spectral and relaxation parameters for the $^3H_4(1)$ to $^1D_2(1)$ transition for each site in 0.02% $Pr^{3+}:Y_2SiO_5$.

	Site 1	Site 2
$\lambda\ (^3H_4(1) \rightarrow {}^1D_2(1))$	605.977 nm	607.934 nm
Γ_{inh}	4.4 GHz	2.5 GHz
T_1	164 ± 5 μs	222 ± 5 μs
$\Gamma_h\ (T_1)$	970 ± 30 Hz	717 ± 16 Hz
T_2^a	152 μs (≡ 2,100 Hz)	377 μs (≡ 848 Hz)
Γ_h^b	1,800 Hz	850 Hz
f	3×10^{-7}	2×10^{-8}
α	$10\ cm^{-1}$	$1.3\ cm^{-1}$

[a] For H_0 = 77 G.

[b] Extrapolated to zero laser intensity for H_0 = 77 G.

Echo decays for each site were recorded as a function of excitation power density with the crystal in zero field and in a field of 77 G. The power dependence of the homogeneous linewidth is shown in figure 5.5. The echo decays were always exponential for both sites. The results shown in figure 5.6 are for the lowest excitation intensities used, corresponding to the most challenging experimental conditions.

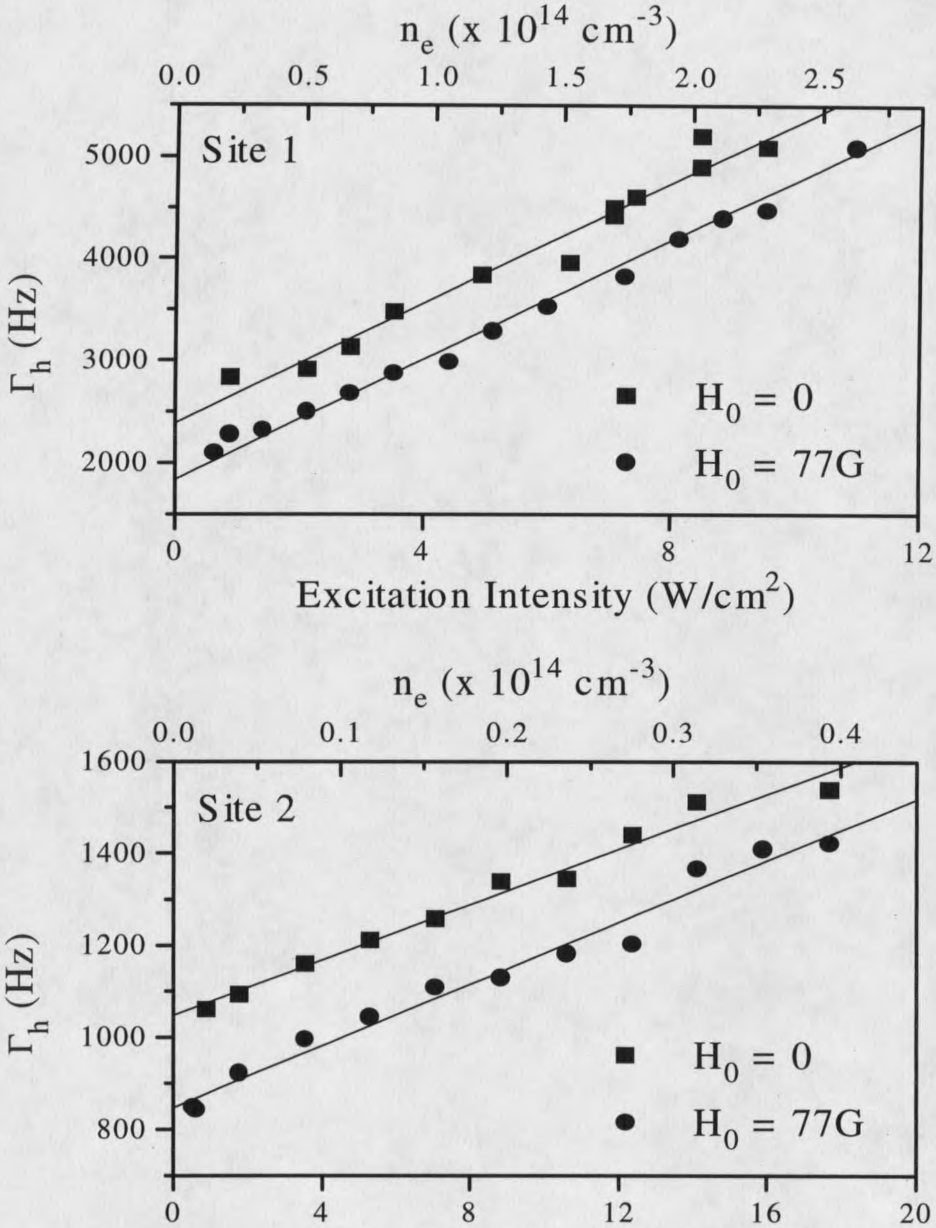

Figure 5.5 Dependence of the homogeneous linewidth of the ${}^3H_4(1) \rightarrow {}^1D_2(1)$ transition on excitation power density for site 1 and site 2 showing the contribution from instantaneous diffusion. Both echo preparation pulses had the same intensity and were varied simultaneously. Alternate axes relate the incident laser excitation power density to the Pr^{3+} excitation density n_e calculated using the absorption coefficients of figure 5.3. The slopes of Γ_h versus n_e are similar for the two sites.

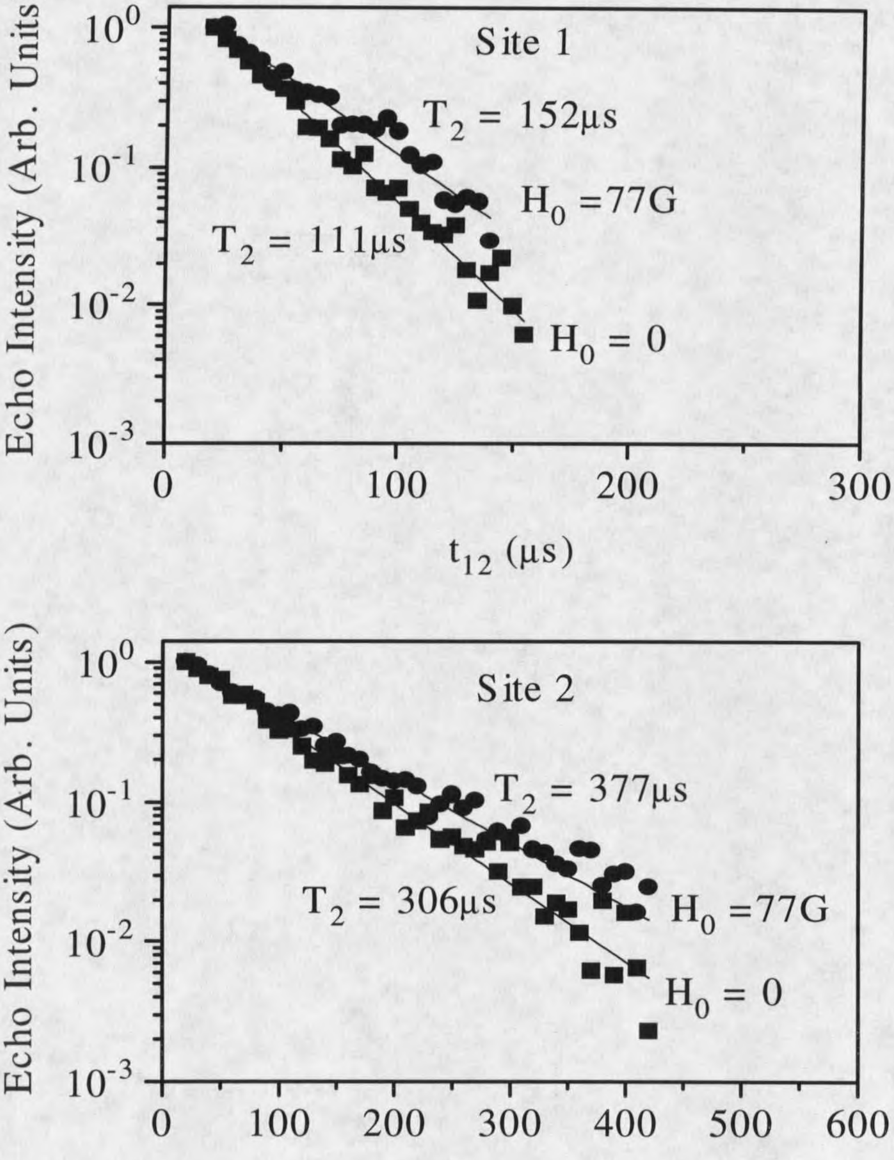

Figure 5.6 Photon echo decays on the $^3H_4(1) \rightarrow {}^1D_2(1)$ transition of $Pr^{3+}:Y_2SiO_5$ at 1.4 K. The excitation density was 0.64 W/cm^2 for site 1 and 0.52 W/cm^2 for site 2. The straight lines are exponential fits to the decays yielding the dephasing times shown. The magnetic field H_0 was applied with a Helmholtz coil.

Dephasing times of T_2 = 111 ± 4 μs for site 1 and T_2 = 306 ± 14 μs for site 2 were recorded at the lowest excitation intensities in zero applied magnetic field. These dephasing times correspond to homogeneous linewidths of 2.8 ± 0.1 kHz for site 1 and 1.04 ± 0.05 kHz for site 2. Extrapolation to zero excitation intensity yielded only a slightly narrower linewidth of 2.4 kHz for site 1 indicating that at the lowest intensities used instantaneous diffusion is adding ~ 400 Hz. The extrapolated value for site 2 was 1.05 ± 0.05 kHz, the same as the measured value within the experimental uncertainty, indicating no measurable contribution from instantaneous diffusion for that site at this excitation power density. The "T_1 limit" for the Pr^{3+}:Y_2SiO_5 crystal studied here is calculated from the measured fluorescence lifetimes given in the previous section. Using $\Gamma_{pop} = 1/(2\pi T_1)$, we found it contributes 970 ± 30 Hz for site 1 and 717 ± 16 Hz for site 2.

Echo decays were also recorded in a field of 77 G to explore the contribution to the linewidth from ^{89}Y nuclear spin fluctuations. The external magnetic field reduced the homogeneous linewidths to 2.1 ± 0.1 kHz (site 1) and 0.85 ± 0.04 kHz (site 2) at the lowest excitation intensities. As for the zero field case, extrapolation to zero excitation intensity yielded a slightly narrower linewidth of 1.8 kHz for site 1, with the value for site 2 essentially the same as that measured to within experimental error. Sensitivity of the homogeneous linewidth to a magnetic field (H_0) indicates nuclear spin-flip-induced dephasing; application of the field modifies the spin dynamics, slowing the ^{89}Y mutual nuclear spin flips thus reducing their contribution to the homogeneous linewidth. In the case of Pr^{3+} in Y_2SiO_5, the application of the 77 G field reduced the linewidth of site 1 by ~ 600 Hz and site 2 by ~ 200 Hz. In the case of site 2, the extrapolated (or measured) linewidth of 0.85 kHz is very close to the 0.72 kHz limit established by population decay. The residual 130 Hz is nearly within the combined experimental and fitting uncertainty of ~80 Hz, although it is expected that a small contribution (~ 50 Hz) due to ^{89}Y nuclear spin flips is still present. The extrapolated value of 1.8 kHz for site 1 is ~800 Hz broader than the T_1 limit. At least some of this additional broadening is due to effects of ^{89}Y mutual spin flips still present at a field intensity of 77 G. The contribution to the homogeneous linewidth due to ^{29}Si nuclear spin fluctuations is expected to be significantly smaller than the contribution from ^{89}Y. The magnetic moment of ^{29}Si (-0.55μ_N) is ~ 4 times that of ^{89}Y (-0.14μ_N), but the concentration of the former is ~40 times lower, resulting in a Pr^{3+} - ^{29}Si coupling strength that is about an order of magnitude smaller than for ^{89}Y. In addition, the dephasing due to ^{29}Si is expected to be less effective since the mutual spin flip rates for the ^{29}Si will be substantially lower than for ^{89}Y.

We recently reported the first observation of optical line broadening by ^{89}Y spin fluctuations for the $^5D_0 \rightarrow {}^7F_0$ transition of $Eu^{3+}:Y_2SiO_5$.[29] The contribution for each site was ~100 Hz. This is considerably smaller than the contributions of ~1.4 kHz for site 1 and ~300 Hz for site 2 observed here for Pr^{3+} ions. The larger contributions for Pr^{3+} are expected however, since the enhanced nuclear magnetic moments[83,84] in the Pr^{3+} ground and excited states are large compared to Eu^{3+} where the magnetic moment is quenched in the ground state and very small in the excited state. The Pr^{3+} ions also exhibit significant differences in the yttrium spin contribution to dephasing for each site; this is presumably a consequence of the differences in the crystal fields at the two sites. Site 1 has a ground state crystal field splitting of 88 cm^{-1} between the two lowest components of the $^3H_4$ manifold, while site 2 has a splitting of 176 cm^{-1}. Since the enhanced magnetic moment, which arises from the second order magnetic hyperfine interaction, is inversely proportional to this energy difference, a larger enhanced moment is expected for site 1 than for site 2.

When comparing the instantaneous diffusion contributions to the dephasing for the two crystallographic sites, it is appropriate to recall[40] that $\Gamma_{\text{ion-ion}}$ in equation 4.1 is proportional to the excitation density and to changes in electric dipolar coupling between Pr^{3+} ions as neighbors undergo transitions between the ground and excited states. When the Pr^{3+} ion excitation density n_e is chosen as the horizontal axis for the Γ_h versus laser excitation power density data, as shown on the alternate scales in figure 5.5, differences in slope arising from the $\Gamma_{\text{ion-ion}}$ contribution to Γ_h reflect differences in dipolar interactions and angular coordination to near and distant neighbors for the two sites. Using the measured absorption coefficients for sites 1 and 2, an effective beam area based on the top-hat approximation $A = \pi w_0^2/2$, and the methods outlined by Liu and Cone,[40] the instantaneous diffusion slopes were found to be 1.2 x 10^{-11} Hz·cm^3 for site 1 and 1.4 x 10^{-11} Hz·cm^3 for site 2. When experimental uncertainty is taken into account, these values are essentially the same, a result that perhaps arises at least in part from the angular averaging that occurs in the summation over large numbers of ions in measurements of $\Gamma_{\text{ion-ion}}$. Information on the dipole moments is not available, precluding a numerical estimate of $\Gamma_{\text{ion-ion}}$ at this time. The absorption coefficient for site 1 is approximately 10 times larger than for site 2, but there is no relationship between the off-diagonal electric dipole moments that determine the optical oscillator strength and the diagonal moments for the ground and excited states that are involved in the instantaneous diffusion. Future studies should include Stark effect measurements to obtain the dipole moment differences.

CHAPTER 6

SPECTROSCOPY AND DYNAMICS OF Tm^{3+}:Y_2SiO_5

The Tm^{3+} ion is of considerable interest for optical signal processing using coherent transients, since the $^3H_6 \rightarrow {}^3H_4$ transition at ~ 790 nm can be excited by commercially available diode lasers. This is an important consideration in efforts to build more compact less expensive devices for demonstration of these PSHB applications. A number of research groups are using Tm^{3+}:YAG for demonstration of signal processing devices,[93] but the presence of fluctuating aluminum spins in the host lattice can add a significant contribution to the homogeneous linewidth. In signal processing applications, long term persistence of the data is not always necessary, but long coherence times are important since the length of the data pulse trains is limited by the homogeneous dephasing time. In the previous two chapters it was shown that the Y_2SiO_5 host lattice was a nearly ideal choice for achieving long dephasing times for the Eu^{3+} and Pr^{3+} ions. As a result, this host was chosen as a good candidate for long dephasing times with the Tm^{3+} ion. Tm^{3+}:Y_2SiO_5 is also of interest as a solid state laser material and has been used in the demonstration of an efficient continuous-wave 2 μm laser.[32] This chapter presents spectroscopic and optical dephasing studies of Tm^{3+}:Y_2SiO_5.

The $Tm^{3+}:Y_2SiO_5$ was produced by Scientific Materials Corporation and contained nominally 0.1% Tm^{3+}. The crystals were unoriented cylinders of diameter 3 mm, with lengths of 1 mm and 5 mm. The ends of the cylinders were polished as were flats along the length of the cylinder to allow detection of fluorescence. The 5 mm sample was used for the white light absorption and Zeeman experiments, and the 1 mm sample for the laser absorption and photon echo experiments. All measurements were performed with the crystal immersed in liquid helium that was pumped to 1.4 K.

Spectroscopy

For memory or signal processing applications, only transitions from the ground state to the lowest level of a given multiplet are of interest. However, in non-zero angular momentum J-multiplets the other low lying levels must also be characterized since they can dramatically influence the dephasing rates of the lowest energy level. The $^3H_6$, $^3H_4$, and $^1G_4$ multiplets of Tm^{3+} in Y_2SiO_5 have therefore been investigated using absorption, fluorescence, fluorescence excitation, and Zeeman experiments. Moderate resolution spectroscopic measurements have been reported previously in studies aimed at characterizing this material as a laser medium.[32,94]

White light absorption spectra were recorded for the $^3H_4$, and $^1G_4$ multiplets at a resolution of 0.5 cm^{-1} using the apparatus described in chapter 3. Figure 6.1 shows the absorption spectrum of the $^3H_4$ multiplet for both crystallographic sites. The site assignment of the lower sharp absorption peaks shown in the inset of figure 6.1 was determined using fluorescence excitation experiments and Zeeman experiments.

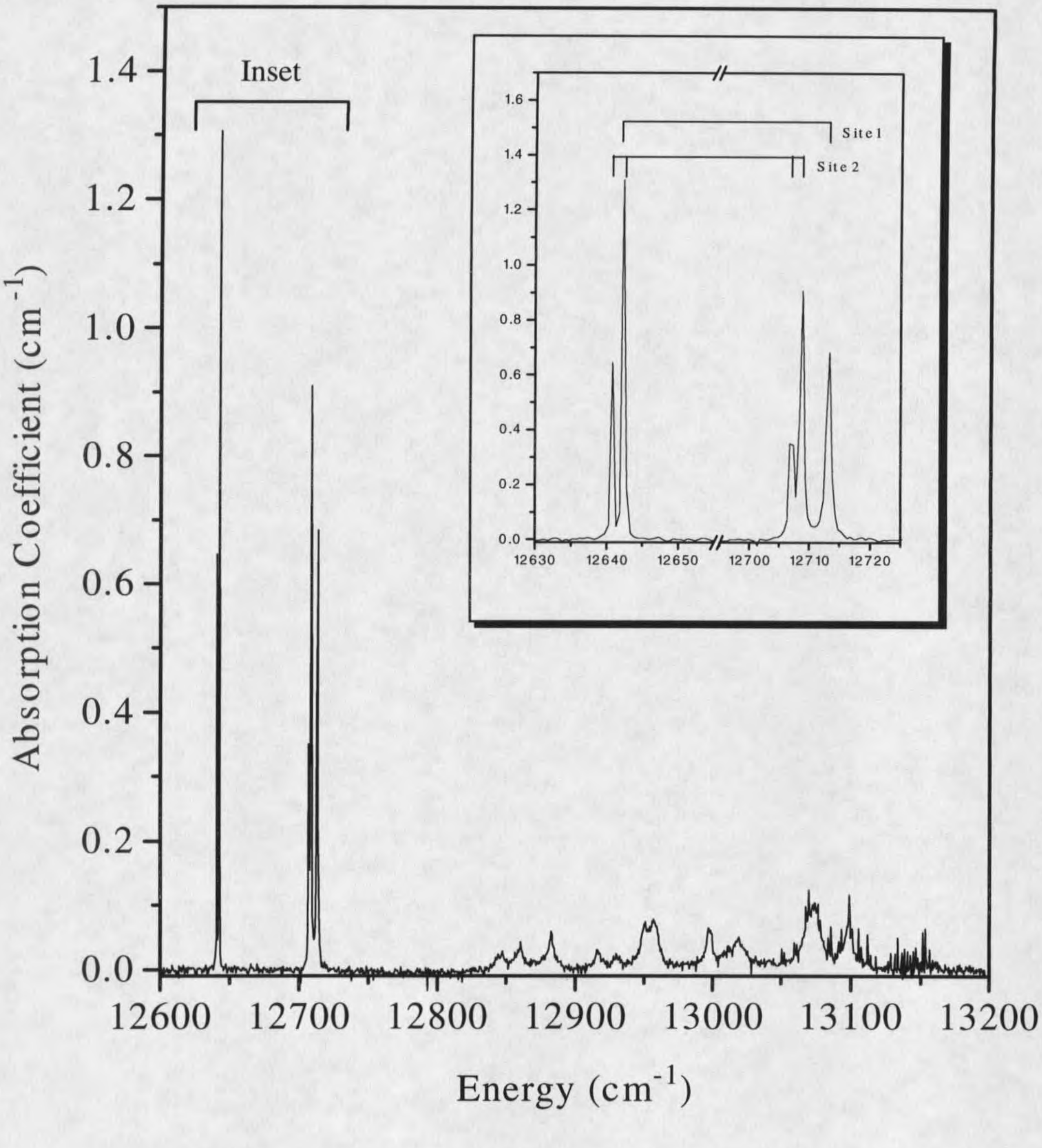

Figure 6.1 White light absorption spectra of the $^3H_4$ multiplet of 0.1% Tm^{3+}:Y_2SiO_5 for both crystallographic sites. Site assignment of the lower sharp peaks of the multiplet is shown in the inset. The broader upper levels have not been investigated since they have no impact on the dynamics of PSHB or echo decay. The peak at 12642 cm^{-1} is actually two peaks separated by 6 GHz (see figure 6.4).

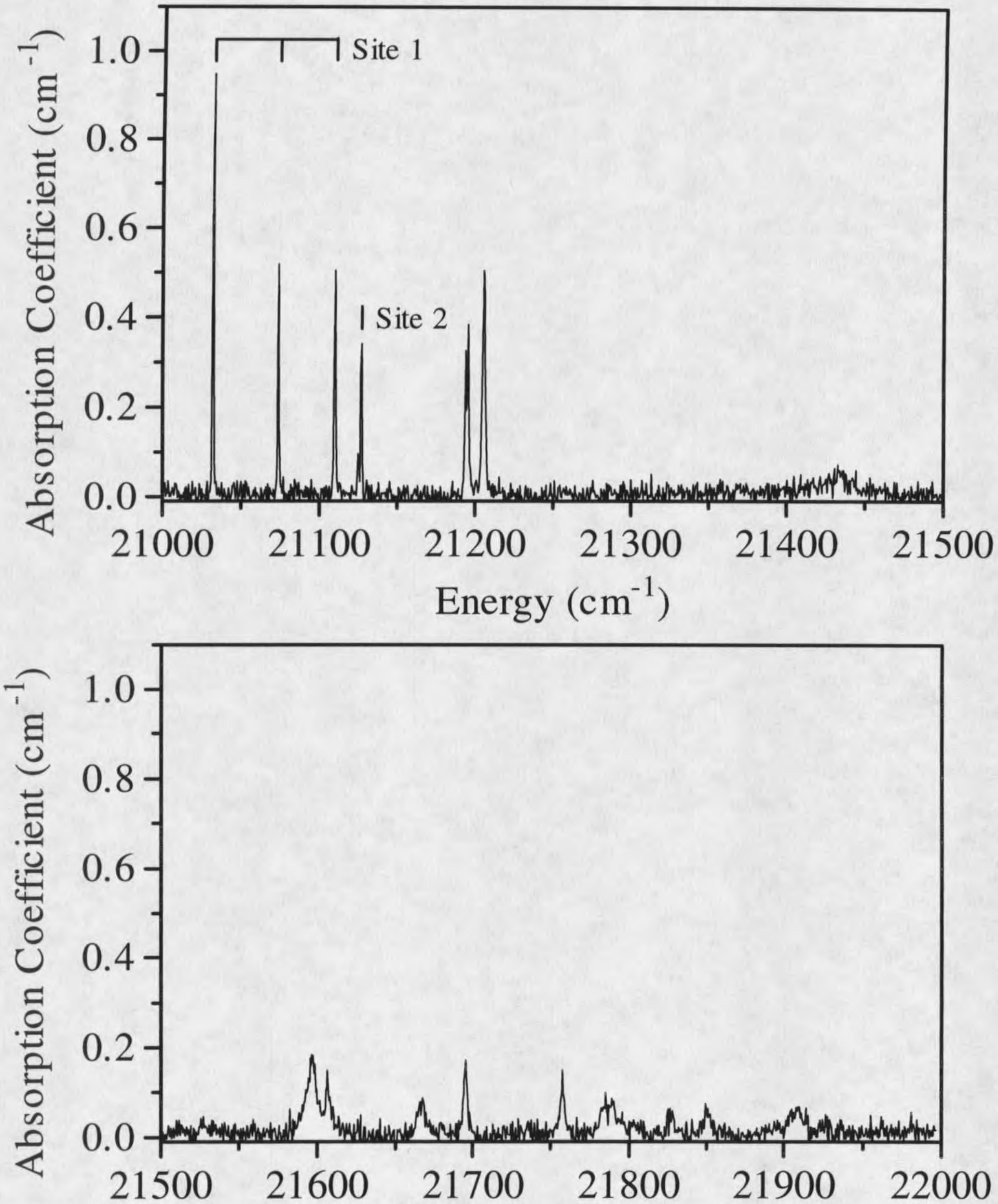

Figure 6.2 White light absorption spectra for the $^1G_4$ multiplet of 0.1% Tm^{3+} doped Y_2SiO_5 for both crystallographic sites. Assignment of the four lowest absorption peaks to the appropriate site was accomplished by correlation of the emission from the $^1G_4$ multiplet excited by an argon laser with the absorption spectra and comparison with site selective emission from the $^3H_4$ multiplet. The unassigned peaks have not been investigated.

Subsequent laser absorption experiments showed that the absorption peak at 12642 cm^{-1} is actually two peaks split by 0.2 cm^{-1}, an amount too small to be resolved by the monochromator in these white light absorption experiments. The $^1G_4$ absorption spectrum is shown in figure 6.2. Site assignment of the $^1G_4$ absorption peaks was accomplished using fluorescence measurements.

Site selective fluorescence measurements were performed for the $^3H_4$ multiplet by exciting from the lowest component of the $^3H_6$ ground state multiplet to an upper component of the $^3H_4$ multiplet for each site; emission from the lowest component of the $^3H_4$ multiplet to the $^3H_6$ multiplet was monitored. For site 1, the $^3H_6$ manifold has a crystal field component only 13 cm^{-1} above the ground state with the next higher level at 226 cm^{-1}, well beyond the range for participation in optical dephasing. Site 2 has an even smaller ground state crystal field splitting with a level only 1.6 cm^{-1} above the ground state. The next higher crystal field level for site 2 is greater that 200 cm^{-1} above the ground state. Higher levels of the ground state manifold are not relevant to optical dephasing at low temperatures and were not investigated.

Fluorescence from the $^1G_4$ multiplet was excited using the 457.9 nm line of an argon laser[95]. Since the excitation was not site selective, both sites fluoresced. Sharp emission lines were observed at 21128 cm^{-1}, 21032 cm^{-1}, and 21019 cm^{-1} with a number of broader lines at lower energies. The first two lines correspond to peaks in the absorption spectra and therefore determine the lowest energy components of the $^1G_4$ multiplet for the two sites; the emission at 21019 cm^{-1} is 13 cm^{-1} above the 21032 cm^{-1}

line, thus identifying the 21032 cm^{-1} level as site 1 by comparison with the $^3H_4$ fluorescence data. The absorption peaks at 21074 cm^{-1} and 21110 cm^{-1} must also belong to site 1 as no emission was detected at these energies. A partial energy level diagram is shown in figure 6.3 summarizing the important low-lying levels of the $^3H_6$, $^3H_4$, and $^1G_4$ multiplets for the two crystallographic sites.

High resolution laser absorption was also performed for the lowest component of the $^3H_4$ multiplet for each site by monitoring the transmission of the single mode Ti:Sapphire laser as it was scanned over 20 GHz. The spectra shown in figure 6.4 were obtained using the unoriented 1 mm sample. The two peaks for the 12642 cm^{-1} line shown in figure 6.4a were clearly resolved, and they correspond to the transitions from the lowest component of the $^3H_6$ ground state multiplet (Z_1) to the lowest component of the $^3H_4$ excited state multiplet (W_1) for the two crystallographic sites. The peak in figure 6.4b corresponds to the transition from the next higher crystal field level of the $^3H_6$ manifold (Z_2) to the lowest component of the $^3H_4$ multiplet (W_1) for site 2. Since the Z_2 level of site 2 is only 1.6 cm^{-1} above the ground state, it is thermally populated at 1.4 K. This crystal had peak absorption coefficients of $\alpha = 12\ cm^{-1}$ (site 1), and $\alpha = 8\ cm^{-1}$ (site 2) for the $Z_1 \rightarrow W_1$ transition in the arbitrarily chosen propagation direction studied here. The $Z_2 \rightarrow W_1$ transition of site 2 had a peak absorption coefficient of $\alpha = 5.3\ cm^{-1}$. A path length of 1 mm resulted in absorptions of 70% for site 1, 55% ($Z_1 \rightarrow W_1$), and 40% ($Z_2 \rightarrow W_1$) for site 2 centered at 790.781 nm, 790.769 nm, and 790.873 nm (in air) respectively.

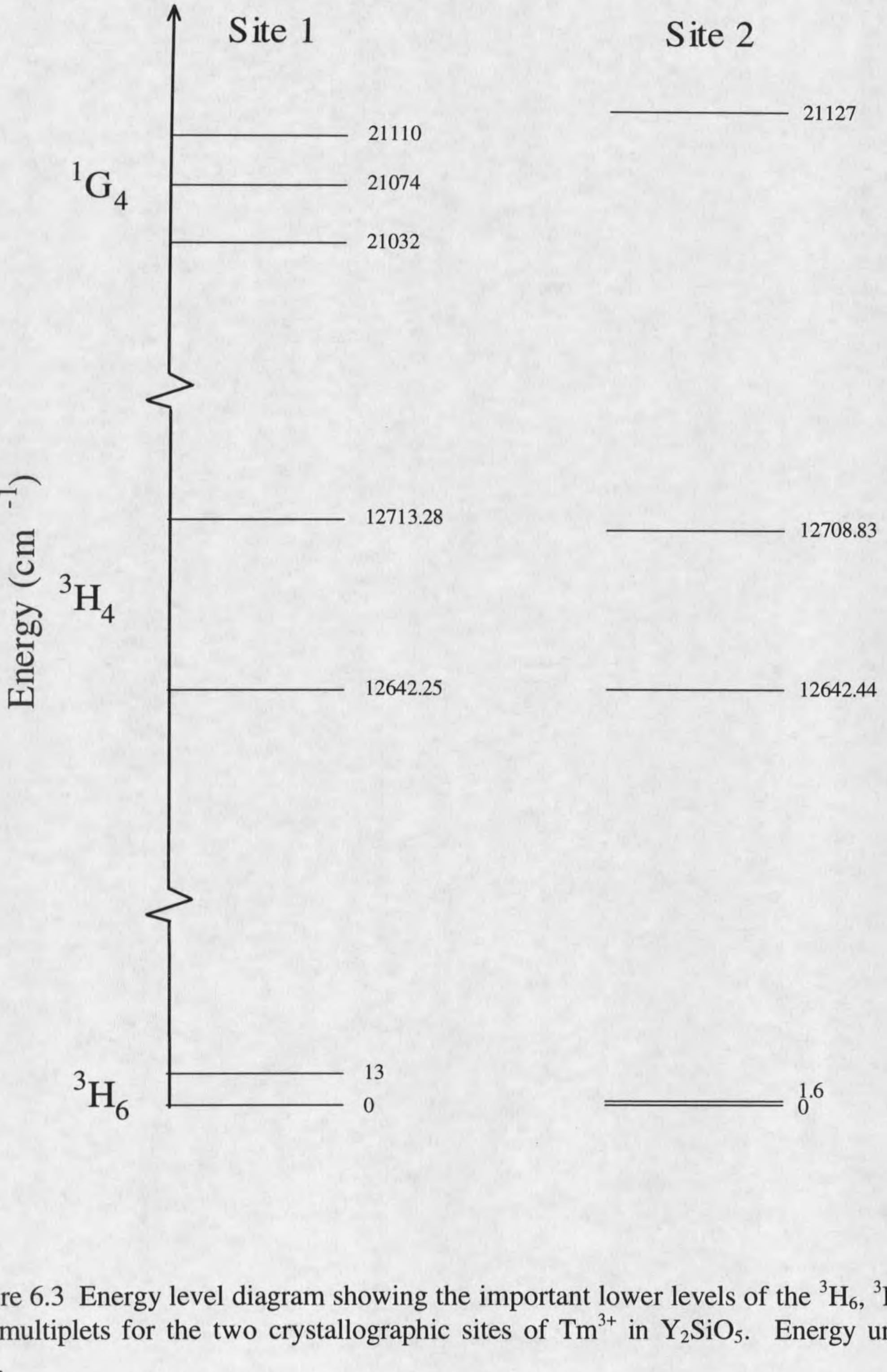

Figure 6.3 Energy level diagram showing the important lower levels of the $^3H_6$, $^3H_4$, and $^1G_4$ multiplets for the two crystallographic sites of Tm^{3+} in Y_2SiO_5. Energy units are cm^{-1}.

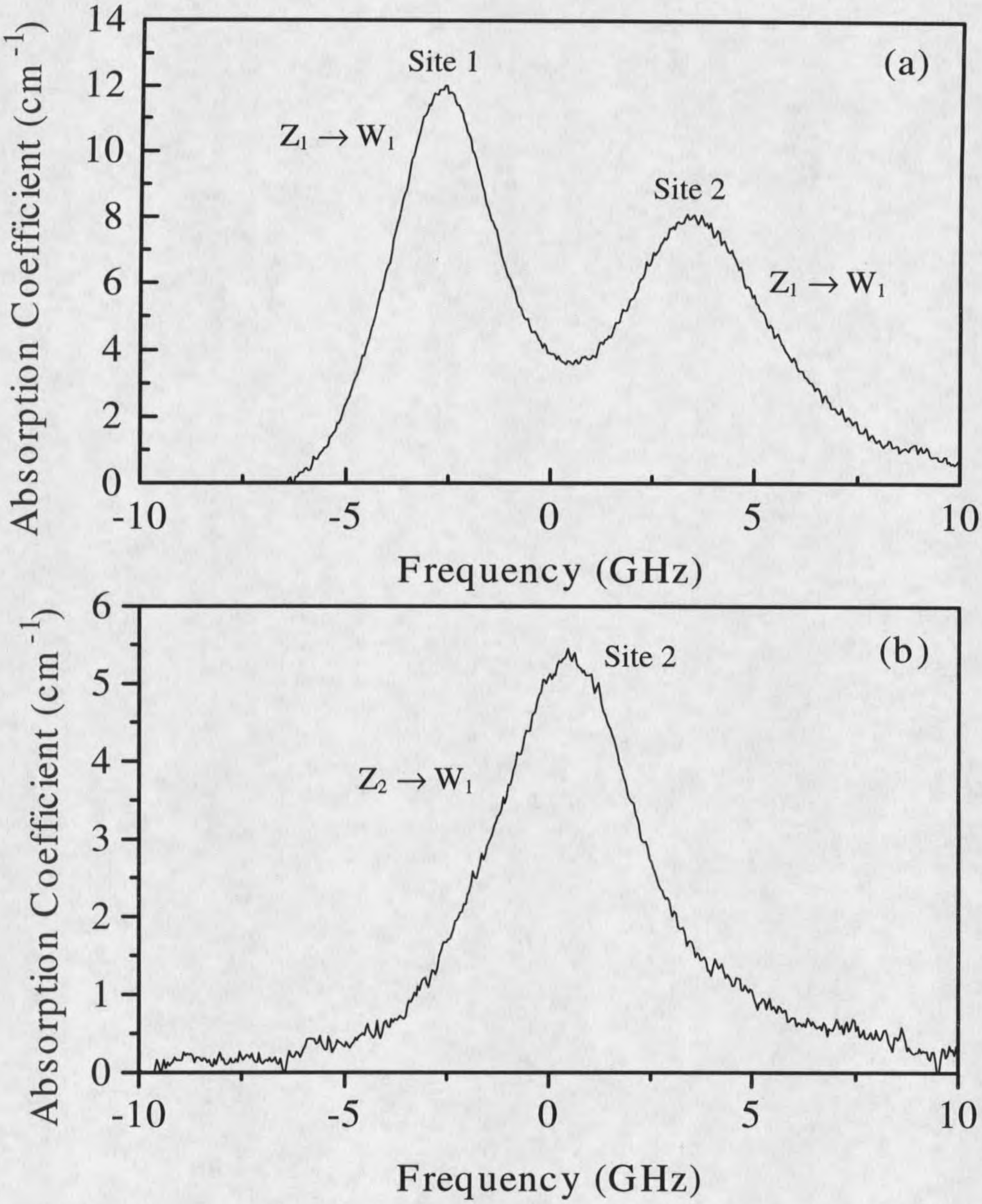

Figure 6.4 Absorption coefficient versus frequency for the lowest components of the $^3H_4$ manifold for each site. The two peaks (12642.25 cm^{-1}, 12642.44 cm^{-1}) in (a) correspond to transitions from the lowest component of the $^3H_6$ ground state multiplet to the lowest component of the $^3H_4$ excited state multiplet ($Z_1 \rightarrow W_1$) for each crystallographic site. The peak (12640.77 cm^{-1}) shown in (b) corresponds to the transition from the next higher level in the $^3H_6$ multiplet to the lowest component of the $^3H_4$ multiplet ($Z_2 \rightarrow W_1$) for site 2.

respectively. The inhomogeneous linewidths were 2.6 GHz for site 1, 4.5 GHz ($Z_1 \rightarrow W_1$), and 5.3 GHz ($Z_2 \rightarrow W_1$) for site 2.

Fluorescence lifetimes were measured by resonantly exciting from the $^3H_6$ ground state to the lowest components of the $^3H_4$ excited state with gated pulses of 1 μs duration from the cw Ti:Sapphire laser. Fluorescence was detected at 90° relative to the laser beam with the PMT at the dewar window. The crystal surfaces were polished quite well and only minimal laser scatter was detected by the PMT. The fluorescence lifetimes were T_1 = 55 μs for site 1 and T_1 = 110 μs for site 2. These are considerably shorter than the 790 μs lifetime reported for 0.15% Tm^{3+}:YAG.[45] This most likely reflects a stronger multiphonon relaxation rate in Y_2SiO_5.

The Zeeman effect has been measured for the sharp $^3H_6 \rightarrow {}^3H_4$ absorption lines shown in the inset of figure 6.1. For the Zeeman experiments, the sample was placed in a small split-pair superconducting magnet designed by Harry Jones and MJM Leask at the Clarendon Laboratory of the University of Oxford. The magnet had a bore of 8 mm and four holes of 4 mm diameter in the sides to provide radial optical access to the sample. The magnet had a field to current ratio of 0.800 kG/A. Zeeman splittings were detected using white light absorption. Spectra were recorded with the SPEX operated at a theoretical resolution of 0.1 cm^{-1} and with external magnetic fields of up to 44 kG. In practice, the observed resolution of the monochromator was approximately 0.3 cm^{-1}. Figure 6.5 shows Zeeman data for the lowest component of the $^3H_4$ multiplet (W_1) for both sites. Figure 6.6 shows absorption spectra at the same values of the applied magnetic field for the next higher crystal field level (W_2) for site 1 and 2. The absorption peaks in figures 6.5 and 6.6 have been labeled indicating the transition and site to which they belong.

Each absorption peak for sites 1 and 2 became two peaks when an external magnetic field was applied as shown in figures 6.5 and 6.6. The possibility that these additional peaks were due to Zeeman splittings of degenerate levels was ruled out since the Zeeman effect was not linear and all of the 18 levels of the $^3H_4$ multiplet are seen in the white light and laser absorption spectra. The additional peaks are thus attributed to differences in the quadratic Zeeman shifts for the two magnetically inequivalent sites that are expected for this monoclinic crystal of the C_{2h}^6 space group. Operating on a magnetic field vector of arbitrary orientation with each of the elements of this space group predicts that ions of given crystallographic sites will experience two different orientations of the magnetic field. Since these two magnetically inequivalent sites see different magnetic field vectors, they can have different Zeeman shifts. The effect of this can then be seen when two levels of the same crystallographic site are in close proximity and shift differently in an external magnetic field.

For site 1 of Tm^{3+} in Y_2SiO_5, the two lowest components of the $^3H_4$ excited state multiplet are separated by 71 cm^{-1} and have an extremely weak Zeeman interaction. The ground state and the next crystal field level are separated by only 13 cm^{-1}, and these two coupled singlet levels repel each other at different rates for the two magnetically inequivalent sites in an external magnetic field due to the

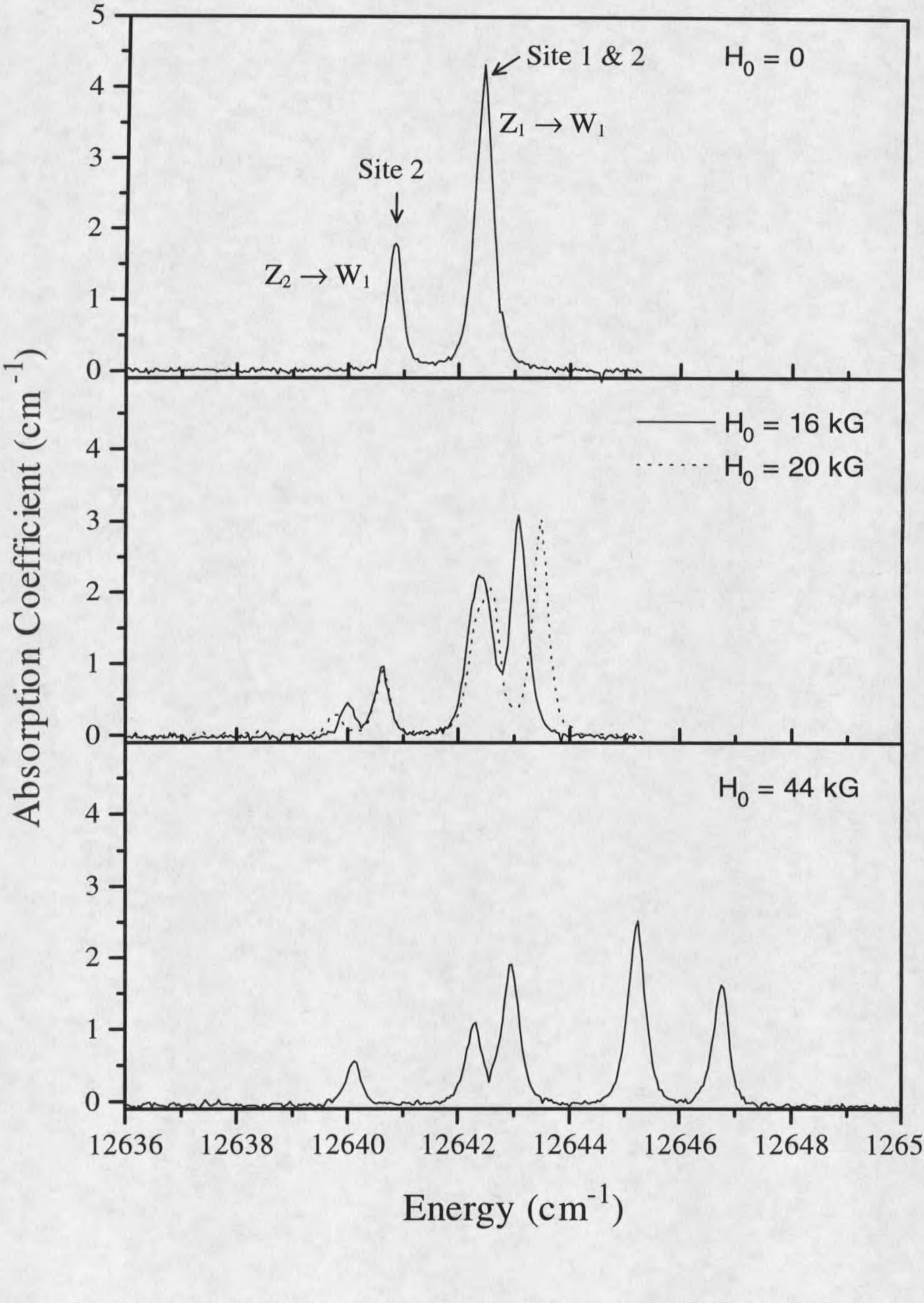

Figure 6.5 Absorption spectra with an external magnetic field applied showing the Zeeman effect for the lowest levels of the $^3H_4$ multiplet for the two crystallographic sites.

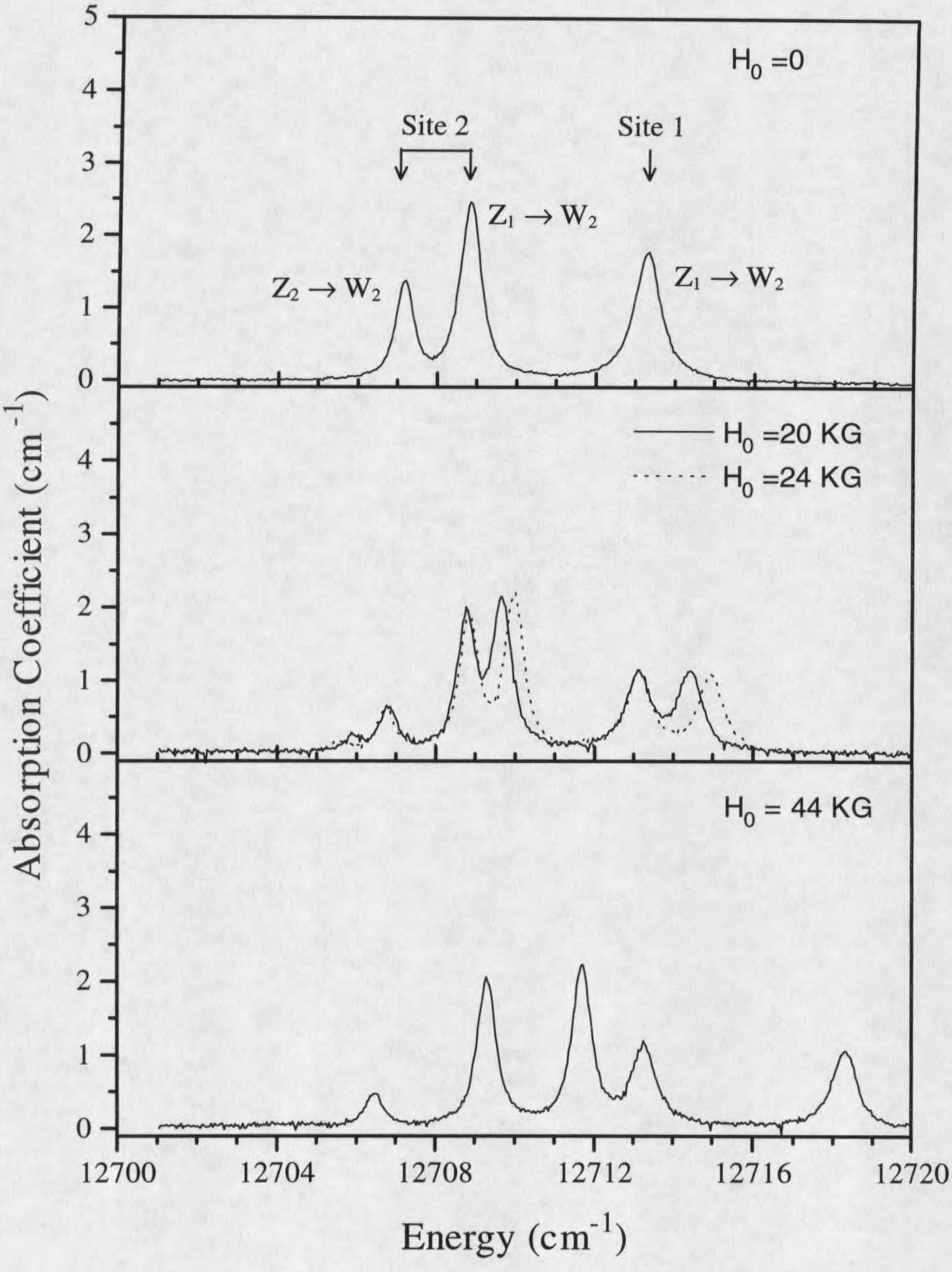

Figure 6.6 Absorption spectra showing the Zeeman effect for the next higher crystal field levels of the $^3H_4$ multiplet for both sites.

quadratic Zeeman effect, resulting in two absorption peaks for each zero field transition as observed. The positions of the absorption peaks for site 1 are plotted in Figure 6.7(a) showing the Zeeman effect of the ground state and 13 cm^{-1} level for the two magnetically inequvalent sites. One magnetic site showed a significant Zeeman effect resulting in a shift of several wavenumbers in the energy levels. However, the other magnetic site showed no observable shifting of the ground state levels. Identical behavior was observed for the site 1 $^1G_4$ absorption level shown in figure 6.8, where one peak remained stationary and the shifting of the other peak to higher energy as a function of magnetic field matched the motion of the $^3H_4$ $Z_1 \rightarrow W_1$ and $Z_1 \rightarrow W_2$ transitions.

Site 2 exhibited similar behavior since the two lowest components of the $^3H_4$ excited multiplet are separated by 67 cm^{-1} and as for the case of site 1 do not interact appreciably in an applied magnetic field. The two lowest components of the ground state multiplet are separated by only 1.6 cm^{-1} and repel in an external magnetic field. This motion of the ground state and 1.6 cm^{-1} level can be seen as shifts in the $^3H_4$ absorption peaks as shown in figure 6.7(b).

The spectroscopy of Tm^{3+} doped into other low symmetry hosts like Y_2O_3[96], $YAlO_3$[97], and YAG[98] has been reported previously. In the case of Y_2O_3, the ground state and next higher crystal field level are separated by 30.7 cm^{-1}, while the two lowest levels of the $^3H_4$ multiplet are split by 78.6 cm^{-1}. Tm^{3+}:YAG has very similar crystal field splittings of 27 cm^{-1} for the $^3H_6$ ground state multiplet and 72 cm^{-1} for the $^3H_4$ multiplet. Tm^{3+} in $YAlO_3$ had a much smaller ground state splitting of only 3 cm^{-1} and a

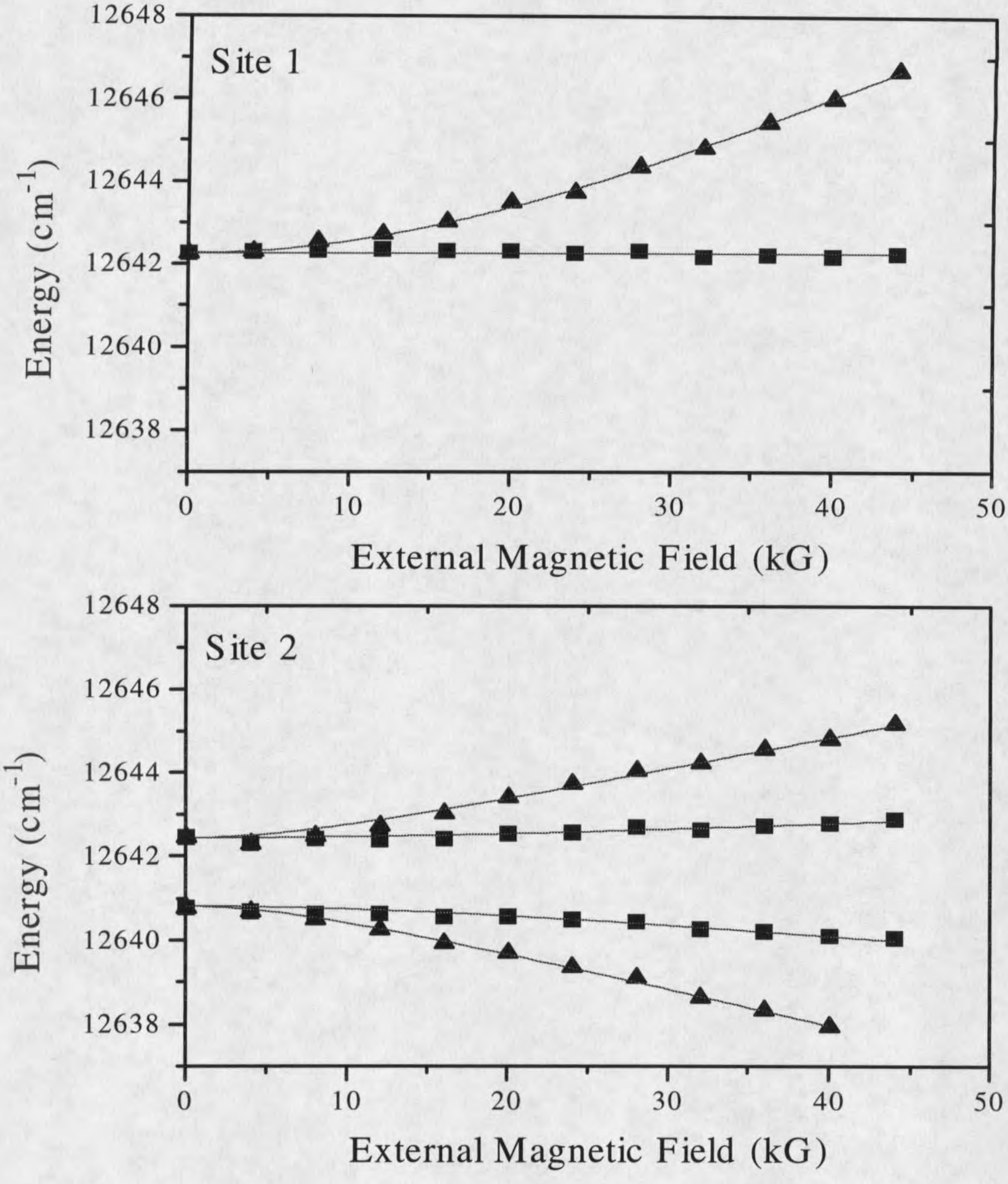

Figure 6.7 Positions of the $^{3}H_{4}$ absorption peaks versus applied magnetic field showing the Zeeman effect of the ground state crystal field levels for both crystallographic sites. The positions for the two peaks in (a) and four peaks in (b) show the different Zeeman effects for the two magnetically inequivalent sites.

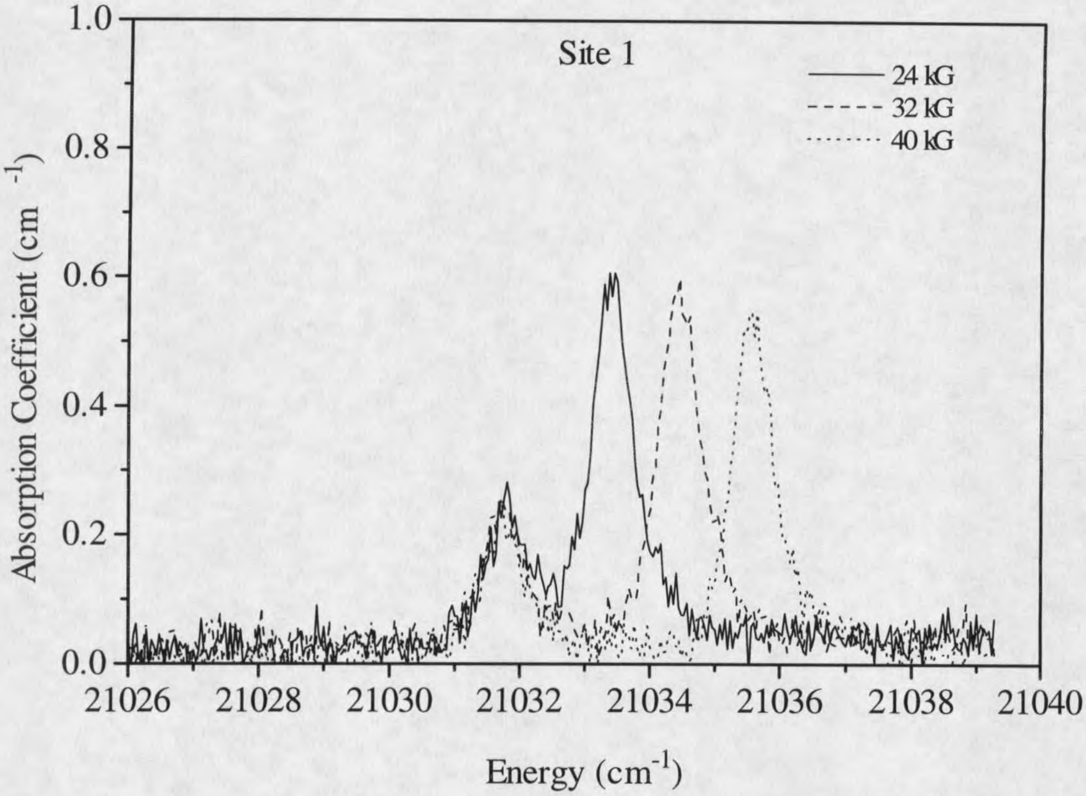

Figure 6.8 Zeeman effect for the lowest $^1G_4$ level of site 1. The lower energy peak is stationary in field and corresponds to one of the magnetically inequivalent sites. Motion of the other peak with applied magnetic field is due to the Zeeman splitting of the ground state for the other magnetic site.

comparable 62 cm^{-1} splitting for the $^3H_4$ multiplet. The 13 cm^{-1}, and 1.6 cm^{-1} splittings for the ground state $^3H_6$ multiplet seen for the two sites in the Y_2SiO_5 host are somewhat smaller but in comparison to these other hosts, are perhaps not surprising. The splittings for the $^3H_4$ multiplet in Y_2SiO_5 are very similar to those reported for Y_2O_3, YAG, and $YAlO_3$.

Photon Echo Measurements

The optical dephasing times for transitions to the lowest $^3H_4$ levels of each site were measured using photon echoes. Measurements were made on the 1 mm sample using the cw Ti:Sapphire laser and the experimental setup described in chapter 3. A 33 cm lens was used to focus the beam to a waist of radius 36 μm. Echo decays were recorded in zero field for the $Z_1 \rightarrow W_1$ transition of site 1 and for the $Z_1 \rightarrow W_1$, and $Z_2 \rightarrow W_1$ transitions of site 2. The effects of instantaneous diffusion were not rigorously studied.

Figure 6.9 shows echo decays for the $Z_1 \rightarrow W_1$ transitions recorded using pulses of 0.5 μs duration with a peak power of 1 mW for site 1, and pulses of 0.2 μs duration with a peak power of 10 mW for site 2. The pulse areas used for the two levels were comparable since the pulse width was reduced by approximately the same factor as the electric field amplitude was increased. These experimental conditions resulted in dephasing times of T_2 = 4.8 μs for site 1, and T_2 = 1.3 μs for site 2 corresponding to homogeneous linewidths of Γ_h = 66 kHz and Γ_h = 241 kHz for sites 1 and 2 respectively. A detailed study of the effects of instantaneous spectral diffusion has not yet been performed for this crystal. Figure 6.10 shows an echo decay for the $Z_2 \rightarrow W_1$ transition of site 2 recorded using pulses of width 0.2 μs, with a peak power of 10 mW. The dephasing time was measured to be T_2 = 1.1 μs corresponding to a homogeneous linewidth of Γ_h = 289 kHz.

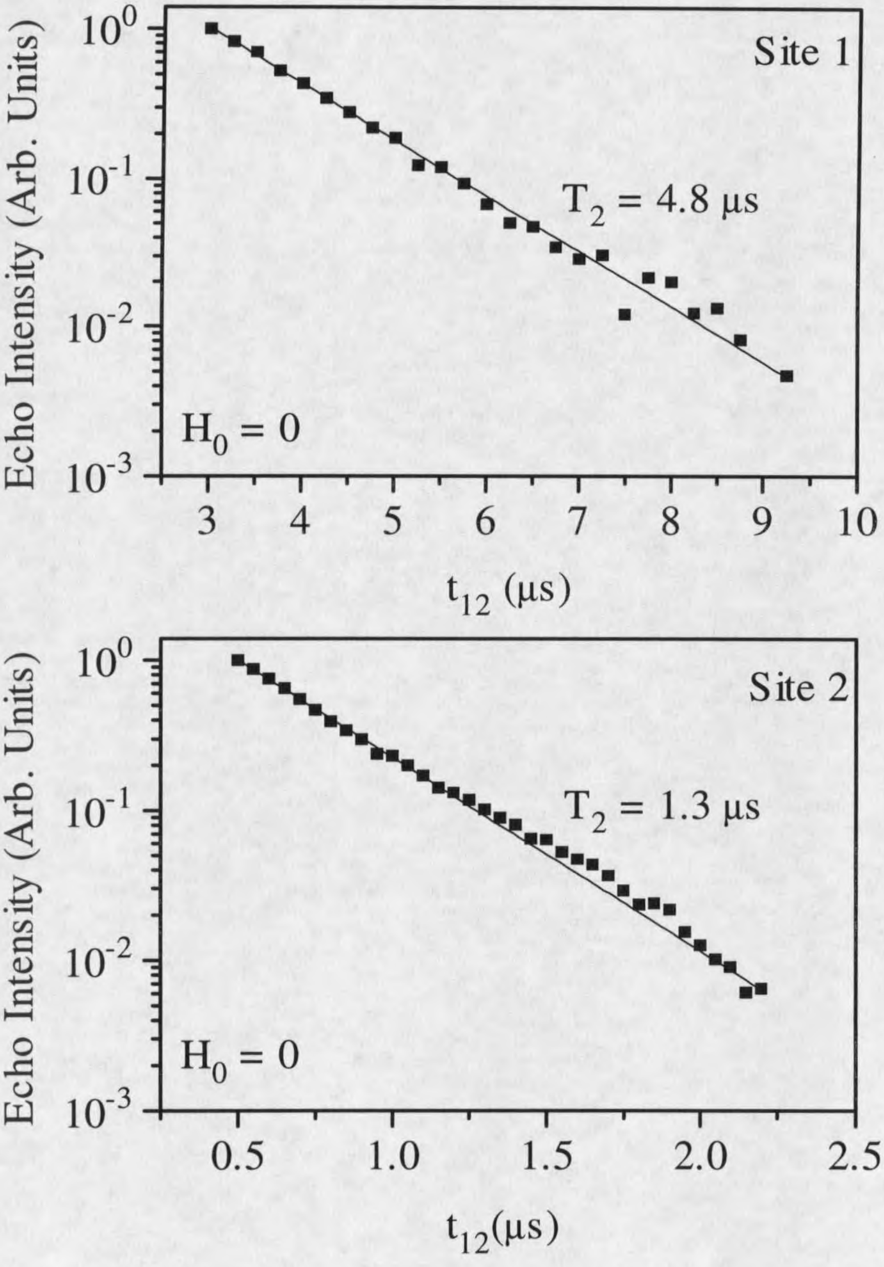

Figure 6.9 Photon echo decays for the $Z_1 \rightarrow W_1$ transitions for both crystallographic sites of Tm^{3+}:Y_2SiO_5. No external magnetic field was applied.

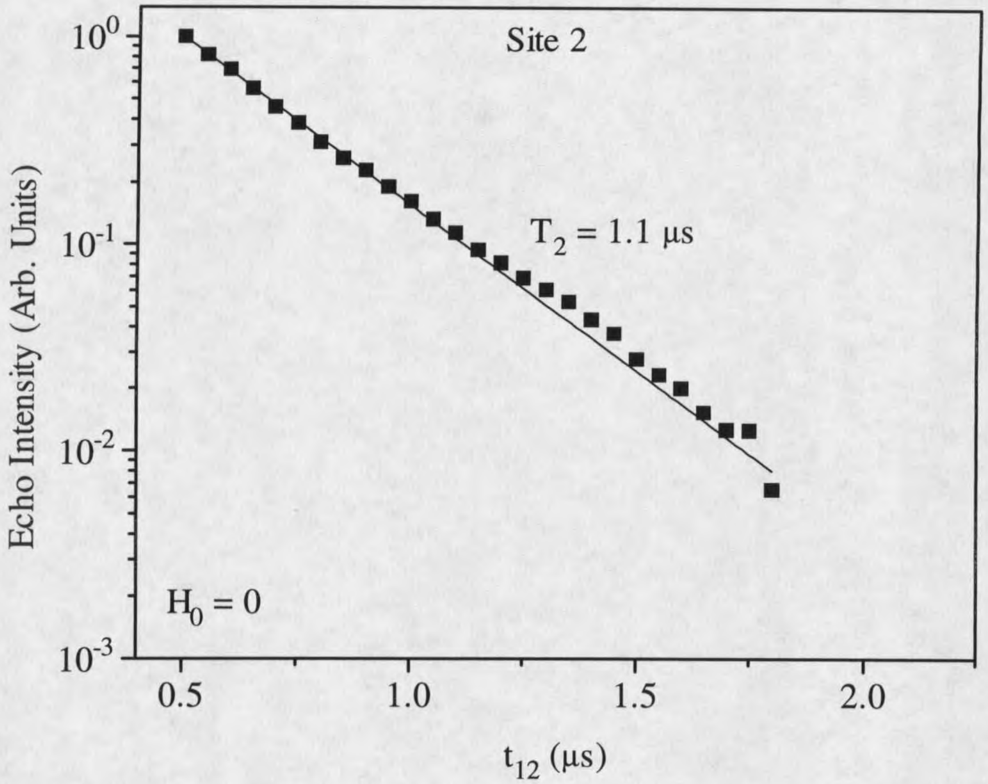

Figure 6.10 Photon echo decay for the $Z_2 \rightarrow W_1$ transition of site 2. 0.2 μs excitation pulses were used with a peak power of 10 mW.

Echo decays were also recorded in an external magnetic field of 40 kG. Echoes were excited using 1μs pulses with a peak power of 0.3 mW for the three transitions at 12643 cm^{-1}, 12645 cm^{-1}, and 12646.8 cm^{-1} shown in figure 6.5 at a field of 44 kG. Nearly identical dephasing times of 34 μs and 33 μs were measured for the two lower energy peaks with the 12646.8 cm^{-1} transition yielding a slightly longer dephasing time of 40 μs. The reduction of the linewidth in an applied magnetic field is in part due to a decrease in the contribution from the ^{89}Y fluctuating nuclear spins as was seen in the cases of Eu^{3+} and Pr^{3+}. In addition, it is also likely that some portion of the narrowing of the homogeneous linewidths observed for these measurements is due to a decrease in the instantaneous diffusion resulting from the use of lower excitation intensities as compared to those used for the zero field measurements shown in figure 6.9.

All of the dephasing times measured for the 0.1% Tm^{3+}:Y_2SiO_5 crystal studied here are considerably shorter than for a 0.15% Tm^{3+}:YAG sample studied by Macfarlane,[45] who reported a dephasing time of 105 μs in a field of 438 G. Dephasing times in Y_2SiO_5 were expected to be longer than for YAG since the magnetic moments of the constituent ions are much smaller than for YAG (aluminum has a nuclear moment of 3.6 μ_N). These shorter dephasing times found for Y_2SiO_5 are attributed to a much greater magnetic sensitivity of Tm^{3+} due to the electronic structure for the ion in this host. For the case of site 1, the ground state crystal field splitting of 13 cm^{-1} will contribute to the enhanced nuclear magnetic moment as described in chapter 4. Site 2 has a an even smaller ground state splitting of only 1.6 cm^{-1} and should therefore have an even larger enhanced nuclear magnetic moment; this is consistant with the shorter dephasing times observed for site 2 compared with site 1. These enhanced magnetic moments in the ground state will result in a much greater sensitivity of the Tm^{3+} ions to fluctuating nuclear and electronic spins of the host lattice. More detailed studies of the effects of instantaneous diffusion are required to quantify the contribution to the linewidth due to the interaction with the host lattice spins. Ultimately though, this material is not considered a good candidate for optical signal processing applications.

Even if the T_1 limit could be achieved, (which is certainly not probable with the observed energy level structure) dephasing times would only be comparable to those already easily obtained for Tm^{3+}:YAG.

CHAPTER 7

SUMMARY

Studies of the spectroscopy and relaxation dynamics of Eu^{3+}, Pr^{3+}, and Tm^{3+} doped Y_2SiO_5 have been presented. The primary goal of these studies was determining the coherence times or homogeneous linewidths and the dephasing mechanisms responsible for the observed linewidths to characterize these materials performance potential in optical memory or signal processing devices.

In the case of Eu^{3+}:Y_2SiO_5, careful elimination of the effects of instantaneous diffusion and shielding the sample from electromagnetic fields allowed measurement of the intrinsic homogeneous linewidth of the $^7F_0 \rightarrow {}^5D_0$ transition at 1.4 K. The total linewidth was separated into two contributions: one due to population decay and the other due to the spin fluctuations of the ^{89}Y nucleus. The homogeneous linewidths measured in these experiments, i.e., 122 Hz for ions in site 1 and 167 Hz for ions in site 2 and the values corrected for instantaneous diffusion 105 Hz for the two sites are, to the best of our knowledge, the narrowest optical resonances yet measured in the solid state. Isolated rare-earth ions at low temperatures behave in some respects like trapped single ions, and by careful selection of host crystal it should be possible to achieve linewidths of less than 100 Hz which would rival the narrowest resonances observed for trapped single ions in the "gas phase." Such extremely narrow resonances can also provide very sensitive probes of local dynamics or external fields in solid state systems.

The spectroscopic properties and dephasing mechanisms of Pr^{3+} ions in Y_2SiO_5 have also been investigated in detail. We have extended existing spectroscopic information by a high resolution determination of the hyperfine levels for the lowest energy component of the $^1D_2$ excited state for both crystallographic sites. Upper crystal field components of the $^1D_2$ multiplet were identified and assigned to the appropriate site, and absorption spectra were presented for higher multiplets which had not been previously reported.

The homogeneous linewidth of the transition from the $^3H_4(1)$ ground state to the $^1D_2(1)$ excited state was measured for the two crystallographic sites using photon echoes. The contributions to the homogeneous linewidths were identified for each site after detailed characterization of the effects of excitation-intensity-dependent dephasing. At a temperature of 1.4 K, each site had two contributions to the linewidth: a small contribution from ^{89}Y nuclear spin fluctuations and a larger contribution from population decay. The host crystal Y_2SiO_5 was again shown to yield a narrower optical resonance for a specific ion, in this case Pr^{3+}, than for any previously reported host. It was also clear from this and other studies, that any measurement of a homogeneous linewidth using photon echoes requires careful identification of the instantaneous diffusion contribution in order to characterize the intrinsic optical resonance width.

The spectroscopy of Tm^{3+}:Y_2SiO_5 was investigated by performing absorption, fluorescence, fluorescence excitation and Zeeman experiments on the $^3H_6$, $^3H_4$, and $^1G_4$ multiplets. These spectroscopic studies showed that the lowest levels of the $^3H_4$ excited multiplet for the two crystallographic sites were separated by only 6 GHz. In addition, the two lowest crystal field levels of the ground state multiplet were separated by 13 cm^{-1} for site 1 and only 1.6 cm^{-1} for site 2. These ground state splittings are quite small but do not differ dramatically from those observed for Tm^{3+} in other hosts. Specifically, the spectroscopy of Tm^{3+} in other low symmetry crystals like Y_2O_3[96], $YAlO_3$[97], and YAG[98] has been reported where the $^3H_6$ ground state manifold had crystal field levels ranging from 3 cm^{-1} to 30 cm^{-1} above the ground state.

The homogeneous linewidth of the lowest $^3H_4$ crystal field levels were measured for both crystallographic sites. Linewidths of 57 kHz for site 1 and 241 kHz for site 2 were found in zero applied field. These are significantly broader homogeneous linewidths than the 3 kHz that has been reported for Tm^{3+}:YAG.[45] The short dephasing times in this crystal are attributed to the magnetic sensitivity of the Tm^{3+} in this host resulting from enhanced nuclear magnetic moments from the small ground state crystal splitting. A detailed study of the effects of instantaneous diffusion must be performed to quantify the contributions to the linewidth from fluctuating spins of the host lattice.

REFERENCES CITED

REFERENCES CITED

1. *Persistent Spectral Hole-Burning: Science and Applications,* Vol 44 Topics in Current Physics, Edited by W. E. Moerner, (Springer, 1988).

2. T. W. Mossberg, Opt. Lett. **7**, 77 (1982).

3. W. R. Babbitt and T. W. Mossberg, Opt. Comm. **65**, 185 (1988).

4. M. Mitsunaga, R. Yano, and N. Uesugi, Opt. Lett. **16**, 1890 (1991).

5. T. W. Mossberg Opt. Lett. **17**, 535 (1992).

6. Y. S. Bai and R. Kachru, Optics Lett., **18**, 1189 (1993).

7. R. Yano, M. Mitsunaga, and N. Uesugi, J. Opt. Soc. Am. B **9**, 992 (1992).

8. X. A. Shen, and R. Kachru, Opt. Lett. **18**, 1967 (1993).

9. *Persistent Spectral Hole Burning Workshop,* IBM Almaden Research Center, San Jose, California, July 28-30, 1993.

10. W. R. Babbitt and T. W. Mossberg, J Opt. Soc. Am B **11**, 1948 (1994).

11. Y. S. Bai, W. R. Babbitt, N. W. Carlson, and T. W. Mossberg, Appl. Phys. Lett. **45**, 714 (1984); W. R. Babbitt and J. A. Bell, Appl. Opt. **33**, 1538 (1994).

12. P. Hu, R. Leigh, and S. R. Hartmann, Phys. Lett. **40A**, 164 (1972).

13. R. M. Macfarlane and J.-C. Vial, Phys. Rev. B **36**, 3511 (1987).

14. C. von Borczyskowski, A. Oppenlander, H. P. Trommsdorff, and J.-C. Vial, Phys. Rev. Lett. **65**, 3277 (1990).

15. R. M. Macfarlane and R. M. Shelby, Opt. Lett. **6**, 96 (1981).

16. A. J. Meixner, C.M. Jefferson, and R. M. Macfarlane, Phys. Rev. B **46**, 5912 (1992).

17. J. C. Bergquist, F. Diedrich, W. M. Itano, and D. J. Wineland, in *Laser Spectroscopy IX,* edited by M. S. Feld, J. E. Thomas, and A. Mooradian (Academic, San Diego, 1989), p. 274.

18. R. M. Macfarlane, R. M. Shelby, and R. L. Shoemaker, Phys. Rev. Lett. **43**, 1726 (1979).

19. D. Grischkowsky and S. R. Hartmann, Phys. Rev. B **2**, 60 (1970).

20. R. M. Macfarlane and R. M. Shelby, in *Spectroscopy of Solids Containing Rare Earth lons,* edited by A. A. Kaplyanskii and R. M. Macfarlane (North-Holland, Amsterdam, 1987), p. 51.

21. R. M. Macfarlane and R. M. Shelby, Opt. Commun. **39**, 169 (1981).

22. J. Huang, J. M. Zhang, A. Lezama, and T. W. Mossberg, Phys. Rev. Lett. **63**, 78 (1989).

23. R. Yano, M. Mitsunaga, and N. Uesugi, Opt. Lett. **16**, 1884 (1991).

24. R. M. Shelby and R. M. Macfarlane, Phys. Rev. Lett. **45**, 1098 (1980).

25. R. Yano, M. Mitsunaga, and N. Uesugi, Phys. Rev. B **45**, 12752 (1992).

26. S. Kröll, E. Y. Xu, and R. Kachru, Phys. Rev. B **44**, 30 (1991).

27. R. M. Shelby, A. C. Tropper, R. T. Harley, and R. M. Macfarlane, Opt. Lett. **8**, 304 (1983).

28. J. Ganem, Y. P. Wang, R. S. Meltzer, and W. M. Yen, Phys. Rev. B **43**, 8599 (1991); A. Szabo and R. Kaarli, Phys. Rev. B **44**, 12307 (1991).

29. R. W. Equall, Y. Sun, R. L. Cone, and R. M. Macfarlane, Phys. Rev. Lett. **72**, 2179 (1994).

30. C. D. Brandle, A. J. Valentino, and G. W. Berkstresser, J. Crystal Growth **79**, 308 (1986)

31 R. Beach, M. D. Shinn, L. Davis, R. W. Solarz, and W. Krupke, IEEE J. Wuant. Elec. **26**, 1405 (1990)

32. C. Li, R. Moncorge, J. C. Souriau, and C. H. Wyon, Opt. Comm. **101**, 356 (1993).

33. R. M. Shelby and R. M. Macfarlane, Phys. Rev. Lett. **47**, 1172 (1981); K. K. Sharma and L. E. Erickson, Phys. Rev. B **23**, 69 (1981).

34. S. C. Rand, A. Wokaun, R. G. DeVoe, and R. G. Brewer, Phys. Rev. Lett. **43**, 1868 (1979)

35. R. M. Macfarlane, C. S. Yannoni, and R. M. Shelby, Opt. Commun. **32**, 101 (1980).

36. D. R. Taylor and J. P. Hessler, Phys. Lett. **50A**, 205 (1974).

37. G. K. Liu, M. F. Joubert, R. L. Cone, and B. Jacquier, J. Luminescence **38**, 34 (1987).

38. J. Huang, J. M. Zhang, A. Lezama, and T. W. Mossberg, Phys. Rev. Lett. **63**, 78 (1989).

39. G. K. Liu, R. L. Cone, M. F. Joubert, B. Jacquier, and J. L. Skinner, J. Lumin. **45**, 387 (1990).

40. G. K. Liu, and R. L. Cone, Phys. Rev. B **41**, 6193 (1990).

41. J. Huang, J. M. Zhang, and T. W. Mossberg, Opt. Comm. **75**, 29 (1990).

42. S. Kröll, E. Y. Xu, M. K. Kim, M. Mitsunaga, and R. Kachru, Phys. Rev. B **41**, 11568 (1990).

43. Y. S. Bai and R. Kachru, Phys. Rev. B **46**, 13753 (1992).

44. S. B. Altner, U. P. Wild, and M. Mitsunaga, Chem. Phys. Lett. **237**, 406 (1995).

45. R. M. Macfarlane, Opt. Lett. **18**, 1958 (1993).

46. A. Szabo, Phys. Rev. B **11**, 4512 (1975).

47. L. E. Erickson, Phys. Rev. B **16**, 4731 (1977).

48. A. Yariv, *Quantum Electronics*, (John Wiley & Sons, New York1975).

49. M. Zhu and J. L. Hall, J. Opt. Soc. Am. B **10**, 802 (1993).

50. A. Z. Genack, R. M. Macfarlane and R. G. Brewer, Phys. Rev. Lett. **37**. 1078 (1976).

51. M. D. Levenson and S. S. Kano, *Introduction to Nonlinear Laser Spectroscopy* (Academic Press, San Diego, 1988).

52. Y. R. Shen, *The Principles of Nonlinear Optics*, (John Wiley & Sons, 1984).

53. M. Weissbluth, *Atoms and Molecules*, (Academic Press, San Diego, 1978).

54. M. Sargent, M. O. Scully, and W. E. Lamb, *Laser Physics*, (Addison-Wesley, 1974).

55. P. D. Maker and R. W. Terhune, Phys. Rev. **137**, A801 (1965).

56. K. E. Jones and A. H. Zewail, Theory of optical dephasing in condensed phases, in *Advances in Laser Chemistry* Edited by A. H. Zewail (Springer-Verlag, Berlin, 1978), pp. 196-222.

57. W. E. Lamb, Jr., and T. M. Saunders, Jr., Phys. Rev. **119**, (1960).

58. C. Cohen-Tannoudji, Atoms in strong resonant fields, in *Frontiers in Laser Spectroscopy,* edited by R. Balian, S. Haroche, and S. Liberman (North-Holland Publ., Amsterdam, 1977) pp. 3-104.

59. L. Allen and J. H. Eberly, *Optical Resonance and Two Level Atoms* (Wiley Interscience, New York, 1975).

60. A. Abragam, *Principles of Nuclear Magnetism* (Oxford Univ. Press, London and New York, 1961).

61. F. Bloch, Phys. Rev. **70**, 460 (1946).

62. R. P. Feynman, f. L. Vernon, and r. W. Hellwarth, J. Appl. Phys. **28**, 49 (1957).

63. N. A. Kurnit, I. D. Abella, and S. R. Hartmann, Phys. Rev. Lett. **13**, 576 (1964); S. R. Hartmann, Scien. Amer. 32 (1968).

64. J. L. Skinner, H. C. Andersen, and M. D. Fayer, Phys. Rev. A **24**, 1994 (1981); J. Chem. Phys. **75**, 3195 (1981).

65. Y. C. Chen, K. P. Chiang and S. R. Hartmann, Phys. Rev. B **21**, 40 (1980).

66. G. Liu, Ph. D. thesis at Montana State University (Unpublished 1988).

67. E. Hanamura, J. Phys. Soc. Jpn. **52**, 2258 (1983).

68. N. Bloembergen, Physica **15**, 386 (1949)

69. W. B. Mims, K. Nassau and J. D. McGee, Phys. Rev. **123**, 2059 (1961).

70. J. R. Klauder and P. W. Anderson, Phys. Rev. **125**, 912 (1962).

71. W. B. Mims in *Electron Paramagnetic Resonance*, edited by S. Geschwind (Plenum, New York, 1972) p. 263

72. P. Hu and S. R. Hartmann, Phys. Rev. B **9**, 1 (1974).

73. R. M. Shelby, C. S. Yannoni, and R. M. Macfarlane, Phys. Rev. Lett. **41**, 1739 (1978).

74. J. Ganem, Y. P. Wang, D. Boye, R. S. Meltzer, W. M. Yen, and R. M. Macfarlane, Phys. Rev. Lett. **66**, 695 (1991).

75. I. D. Abella, N. A. Kunit, and S. R. Hartmann, Phys. Rev. **141**, 391 (1966).

76. M. Mitsunaga, R. Yano, and N. Uesugi, Opt. Lett. **16**, 264 (1991).

77. Y. Sun, Ph. D. thesis at Montana State University (Unpublished 1993).

78. K. Chiang, E. A. Whittaker, and S. R. Hartmann, Phys. Rev. B **23**, 6142 (1981).

79. R. M. Shelby, R. M. Macfarlane, and R. L. Shoemaker, Phys. Rev. B **25**, 6578 (1982).

80. D. P. Burum, R. M. Macfarlane, and R. M. Shelby, Phys. Lett. A **90**, 483 (1982).

81. P. Hu, R. Leigh, and S. R. Hartmann, Phys. Lett. A **40**, 164 (1972).

82. B. A. Maximov, Yu. A. Charitonov, V. V. Ilyikhin, and N. B. Belov, Dokl. Acad. Nauk SSSR Ser. Mat. Phys., **183**, 1072 (1968).

83. X. A. Shen and R. Kachru, J. Opt. Soc. Am. B **11**, 591 (1994).

84. B. Bleaney, Physica **69**, 317 (1973).

85. A. Abragam, and B. Bleaney, Proc. R. Soc. London Ser. A **387**, 221 (1983).

86. T. W. Mossberg (unpublished).

87. N. J. Simon, E. S. Drexler, and R. P. Reed, *Properties of Copper and Copper Alloys at Cryogenic Temperatures*, (NIST, Boulder, 1992).

88. R. M. Macfarlane, R. Wannemacher, D. Boye, Y. P. Wang, and R. S. Meltzer, J. Lumin. **48/49**, 313 (1991).

89. A. Szabo, Opt. Lett. **8**, 486 (1983).

90. Keith Holliday, Mauro Croci, Eric Vauthey, and Urs P. Wild, Phys. Rev. B **47**, 14741 (1993); [Low resolution measurements without site discrimination were reported for 77 and 300 K by N. V. Kuleshov, V. P. Mikhailov, S. A. Radkevich, V. N. Boikov, D. S. Umreiko, and B. I. Minkov, Opt. Spektrosk. **77**, 244 (1994) {Opt. Spectrosc. **77**, 220 (1994)}].

91. J. M. Baker, and B. Bleaney, Proc. R. Soc. London Ser. A **245**, 156 (1958).

92. M. A. Teplov, Zh. Eksp. Teor. Fiz. **53**, 1510 (1968) [Sov. Phys. JETP **26**, 872 (1968)].

93. *Workshop on Practical Materials for PSHB Devices*, University of Washington, Seattle, Washington, February 1-2, 1995.

94. C. Li, A. Lagriffoul, and Ch. Wyon, J. Lumin. **62**, 157 (1994).

95. Fluorescence measurements on the $^1G_4$ multiplet were performed by R. M. Macfarlane at the IBM Almaden Research Center.

96. J. B. Gruber, W. F. Krupke, and J. M. Poindexter, J. Chem. Phys. **41**, 3363 (1964).

97. V. A. Antonov, P. A. Arsenev, K. E. Bienert and A. V. Potemkin, Phys. Stat. Sol. (a) **19**, 289 (1973); L. M. Hobrock, Ph. D. dissertation (University of Southern California, 1972, unpublished); Fluorescence measurements by R. M. Macfarlane at the IBM Almaden Research Center showed that the two lowest components of the $^3H_6$ ground multiplet were separated by 3 cm^{-1} (private communication).

98. J. B. Gruber, M. E. Hills, R. M. Macfarlane, C. A. Morrison, G. A. Turner, G. J. Quarles, G. J. Kintz, and L. Esterowitz, Phys. Rev. B **40**, 9464 (1989).